2D Material Based PTE Detectors with Room Temperature Operations

by

Zhemiao Xie

A thesis

presented to the University of Waterloo

in fulfillment of the

thesis requirement for the degree of

Doctor of Philosophy

in

Systems Design Engineering

Waterloo, Ontario, Canada, 2023

Examining Committee Membership

The following served on the Examining Committee for this thesis. The decision of the Examining Committee is by majority vote.

External Examiner	Dr. Winnie N. Ye Professor, Department of Electronics Carleton University
Supervisor(s)	Dr. John T.W Yeow Professor, System Design Engineering University of Waterloo
Internal Member	Dr. Ning Jiang Associate Professor, System Design Engineering University of Waterloo
Internal-external Member	Dr. Karim Sallaudin Karim Professor, Electrical and Computer Engineering University of Waterloo
Internal-external Member	Dr. Qi-Ming He Professor, Management Science and Engineering University of Waterloo

Author's declaration

This thesis consists of material all of which I authored or co-authored: see Statement of Contributions included in the thesis. This is a true copy of the thesis, including any required final revisions, as accepted by my examiners.

I understand that my thesis may be made electronically available to the public.

Statement of Contributions

The following is a list of peer-reviewed or under-reviewing journal publications where I am the first author. I am responsible for all the chip designs, fabrications, characterizations, measurements, data analysis, and manuscript writing in these works. The co-authors have helped to review the manuscript and provided revision suggestions.

1. Z. Xie, J. Wang, and J. T. W. Yeow, "Doped Polyaniline/Graphene Composites for Photothermoelectric Detectors," ACS Appl. Nano Mater., vol. 5, no. 6, pp. 7967–7973, 2022, doi: 10.1021/acsanm.2c01039.

(This work is presented in Chapter 3. J. Wang edited the manuscript and J. T. W. Yeow supervised and edited the manuscript.)

2. Z. Xie, J. Wang, and J. T. W. Yeow, "Flexible Multi-Element Photothermoelectric Detectors Based on Spray-Coated Graphene/Polyethylenimine Composites for Non-destructive Testing," ACS Appl. Mater. Interfaces, vol. 15, no. 4, pp. 5921–5930, 2023, doi: 10.1021/acsami.2c20487.

(This work is presented in Chapter 4. J. Wang edited the manuscript and J. T. W. Yeow supervised and edited the manuscript.)

3. Z. Xie, J. Wang, G. Lu, and J. T. W. Yeow, "Room-ambient operation of integrated and visualized photothermoelectric system with patterned Mo_2C/PEDOT: PSS flexible devices," *Mater. Des.*, vol. 235, p. 112383, 2023, doi: 10.1016/j.matdes.2023.112383.

(This work is presented in Chapter 5. J. Wang edited the manuscript, G. Lu worked with SEM images and J. T. W. Yeow supervised and edited the manuscript.)

Abstract

Real-time, room-temperature operation and self-powered photothermoelectric (PTE) detection emeries are advanced and versatile solutions for various applications. These detectors offer the advantage of not requiring external power sources, making them portable and suitable for remote or low-power environments. Additionally, their ability to operate at room temperature eliminates the need for costly and complex cooling systems, making them more accessible and cost-effective for various industries and research fields. However, issues of massive fabrication, complicated manipulations, long-term stability, and flexibility are concerned with engaging new exploration on PTE detectors with low-dimensional materials. Two-dimensional (2D) materials are emerging as leading ones due to their broadband detection from Terahertz (THz) to ultraviolet (UV), electrical conductivity with a small band gap, and strong polymer affinity for thermoelectrical conversion. This thesis aims at using 2D nanomaterials of graphene and molybdenum carbide (Mo_2C) MXene for exploring new PTE detectors, guiding 2D materials methodology, leading the investigation of polymer composites, and providing insights into various industrial, imaging, and health monitor applications.

This thesis introduces three types of room operation and self-powered PTE architectures with 2D nanomaterials. First, we developed a new doped polyaniline (PANI) as the composite material with a few layers of sheets of graphene. Semi-transparent, broadband infrared (IR) detection and robust flexibility features are presented. Second, a vertical graphene/polyethylenimine (PEI) composite multi-element H-shaped detector with the spray-coating method is presented. High response time, detectivity, and a broadly responsive range are achieved with PEI concentration adjustment, lowering the thermal conductivity and enhancing compacity, focusing the realistic situations with low incident power. Finally, we propose a low-noise PTE device that operates at

room temperature by Mo_2C and Poly(3,4-ethylene-dioxythiophene)-poly(styrenesulfonate) (PEDOT: PSS) nanomaterials with a flexible PET substrate. Superior energy conversion and long-term stability of the material and sustainability from surroundings are achieved through material optimizations. Based on such PTE detectors, two promising systems—the motion tracking system and the non-destructive testing (NDT) imaging system—demonstrate the time-tracking of human radiation and high-resolution imaging applications.

Acknowledgments

First, I am profoundly grateful to my esteemed Ph.D. supervisor, Prof. John T.W. Yeow, for granting me the incredible opportunity to pursue doctoral studies under his mentorship. His unwavering belief in my potential and their willingness to invest time and resources in my academic growth have been pivotal in shaping my journey as a researcher. I sincerely appreciate his generous financial support, which eased the financial burden and allowed me to focus wholeheartedly on my studies and research. His meticulous guidance and well-structured working plans provided a clear direction, enabling me to progress significantly throughout my research. Our regular idea communication sessions were intellectually stimulating, and his constructive feedback consistently pushed me to think critically and creatively. His mentorship has been a beacon of inspiration. I am deeply indebted for the wealth of knowledge and expertise he shared, which has undoubtedly enriched my research and personal development. I will forever cherish the invaluable lessons learned under their guidance and their profound impact on my academic and professional life.

Looking back from my primary school in my hometown Nanchong to the University of Waterloo, what a long journey of 23 years of studying and research. My father always encourages me that life is a countless marathon. One may see your competitors rush through you, and you find a hard act to follow. Just remind yourself you're not an imitator. The only thing I need to remember is to know, accept, and be myself. I try to keep my pace running through the marathon, overcoming numerous obstacles, knowing my limitations, improving shortcomings, accepting others' criticism, implying after-action reviews, and following my heart. Although I may lose a lot of opportunities, make countless unsatisfactory judgments, and fall over again and again, there's a voice inside my heart to encourage me to stand up and keep it up. Stay calm and keep hope.

I feel so lucky in my journal that my companions, tutors, and parents encourage me to go out of town to see the world. My hometown lies in a small village in Liqiao, Xichong, and my grandparents spent all their lives supporting their children to leave the village and move to the cities. And my parents, of course, provide me with financial support for my summer camps in the US in Grade 9 and my master's study at Duke University. Understudying cultural differences, feeling independent, and respecting individuals have significantly impacted me in confirming my pace to go outside China to see the world. During my study abroad, I have met many friends I respect and admire; their kindness, heartful support, and academic discussions help me make a significant milestone in my degree. Besides, my tutors and professor are willing to solve my puzzles, give academic suggestions, and encourage my accomplishments. I appreciate their heartful recommendations in pursuing research applications. Finally, I would like to be grateful to my parents, who raised and supported me. They are always concerned about my health and progress, listening to my complaint, and providing many suggestions. Without their careless love, I could not be the person of what I am.

Zhemiao Xie

July 2023

Dedication

This Dissertation is dedicated to my loved parents

Jiafeng Xie

and

Min Xie

who have given me invaluable educational opportunities and my life guide

Table of Contents

List of Figures

List of Tables

List of abbreviations

0D	Zero-dimensional
1D	One-dimensional
2D	Two-dimensional
3DMG	Microporous graphene
Al	Aluminum
CNT	Carbon nanotubes
COVID-19	The coronavirus disease 2019
CVD	Chemical vapor deposition
DOS	Density of states
IoT	Internet of Things
IR	Infrared
LIR	Long-infrared
MIR	Mid-infrared
Mo_2C	Molybdenum carbide
NEP	Noise equivalent power
NDT	Non-destructive testing
NIR	Near-infrared
PANI	Polyaniline
PDMS	Polydimethylsiloxane
PE	Pyroelectric
PEDOT: PSS	Poly(3,4-ethylene-dioxythiophene)-poly (styrene sulfonate)
PEI	Polyethylenimine
PET	Poly (ethylene terephthalate)
PTE	Photothermoelectric
PV	Photovoltaic
RGO	Reduced graphene oxide

Ti	Titanium
TMC	Transition metal carbides
THz	Terahertz
UV	Ultraviolet

Chapter 1 Introduction

1.1 Motivation

High-performance photodetectors draw much attention due to their operation in long-wavelength IR to THz regime and potentially broad application in civil and military applications [1-3]. In various applications such as night vision [4], thermal imaging [5], remote sensing [6], medical diagnostics [7], and security systems [8], infrared optoelectronic detection plays a crucial role by converting infrared radiation into electrical signals for analysis and interpretation [9]. Commercial infrared detectors rely on crystalline epitaxial semiconductor materials like cadmium sulfide crystals [10], gallium arsenide [11], and indium antimonide [12], which demonstrate their unique detectivity. However, concerns about metallic toxicity, cryogenic operations, and expensive fabrication technology have spurred novel nano-technology research.

Developing potential infrared sensors necessitates focusing on advanced materials, fabrication techniques, and integration with appropriate signal processing and data analysis algorithms to address these limitations. The photothermoelectric (PTE) mechanism has garnered significant attention among the emerging mechanisms for converting infrared radiation energy. It allows for the efficient self-power conversion of light into electricity by generating a voltage across a temperature gradient [13-16]. In particular, compared to other photodetection, such as bolometric [17], photovoltaic [18,19], and pyroelectric detectors [20], PTE detectors can achieve sensitive photoresponse at room temperature without external bias support. This effective attribute paves the way for numerous applications such as non-destructive tests in industrials [21], biomedical drug tracking [22], security cameras [23], wearable health monitors [24], and space exploration [25]. PTE detectors also obtain low ratio equivalent power besides broadband spectral response

and an external-free power source. Therefore, only thermal noise signals domains the power. PTE detectors overcome the traditional issue of low signal-to-noise effect [26].

The recent emergence of new low-dimensional nanomaterials, including carbon nanotubes (CNT) [27], graphene [28, 29], black phosphorus,[30] transition metal dichalcogenide monolayers [31], and MXenes [32], has enabled room-temperature photodetection by suppressing hot carrier transport directions [33]. As the foremost two-dimensional (2D) material, graphene obtains the superiority of the conduction and valance bands meeting at the Dirac points. Such a zero-band gap structure enables broadband light absorption from THz to visible light. Besides, the virtual of low-dimensional structures lowers the thermal conductivity of graphene [34]. Other optical properties of high transparency, low reflectance, and high carrier mobility enable high efficiency of PTE conversion. Furthermore, compared to other 2D materials, graphene avoids many 2D materials issues of fragile deformation in ambient surroundings within chemical instability, uncontrollable synthesis with a few synthesized productions, and fragile manipulation of transporting layers on a chip. Additionally, graphene has a polymer affinity by involving polymers as a composite matrix to optimize mechanical stability, biocompatibility, and structure flexibility, paving the way for large-area industrial manipulations and wearable electronics. Molybdenum carbide (Mo_2C), a two-dimensional transition metal carbide nanomaterial, has garnered significant attention for its wide range of applications. Mo_2C has shown promise for broadband detectivity and carrier mobility due to its high Fermi density [35]. One potential advantage lies in combining Mo_2C with polymers, leveraging its high affinity for polymer materials. Incorporating polymers facilitates the connection between uniformly dispersed Mo_2C flakes, forming a composite matrix that optimizes structural flexibility, temperature durability, resistance to chemical degradation, biomedical compatibility, thermal diffusion, and electrical conductivity.

However, challenges remain for PTE detectors. These limitations, including complex and costly manipulation processes, unstable synthesis, vulnerability to oxidation-induced degradation, intricate operations, and difficulties in scalable array designations [36], impede the integration of patterned chips into systems for industrial and commercial utilization. Additionally, concerns regarding weak mechanical strength and lack of portability on silicon or glass substrates hinder the development of PTE detectors suitable for conformable attachments. Expensive cost, uncontrollable formation, and complex fabrication process of producing single-layer graphene sheets with high-quality photon detectivity. Reduced graphene oxide shows relatively high efficiency and broadband light absorption, but its fragility of manipulation and unsuitable ambient environment limit further applications. Besides the materials' selections, state-of-the-art PTE detectors still face the challenges of a controllable, cost-effective, scalable fabrication process. In comparing traditional drop-casting and vacuum filtration methods, the uncontrollable drop-casting of solution volumes depends on the surface contact angles between substrates and solutions. An attractive solid Van der Waals force of a substantial amount prevents solutions from combining on relative hydrophobic surfaces and easily peeling off from the surface after drying out [37]. The spin coating method may precisely control the surface. However, the surface's non-uniform due to the flow output fluctuation mitigates the uniformity of electrode depositions and further conversion efficiency [38]. Spray coating is a cost-effective method of accelerating reagent inks through the Venturi effect, where the compressed air stream atomizes the solution [39]. Continuous liquid droplets are driven from a reservoir when pressure differences establish between the orifice and the tip and then broken up into several smaller fluid masses by Rayleigh instability [40, 41]. The feature size of the continuous droplets depends on area deposition scales and the jet breakup, where the solution viscosity, air pressure input and surface tension can easily manipulate [40, 42]. As a

promising technique, spray coating overcomes the limitations of irregular and coarse substrates. Besides, droplets can cause adjustment by controlling the flow rate, and the spraying layer's height can be precisely adjusted [43, 44].

To overcome these challenges, this thesis aims to develop a novel and scalable infrared optoelectronic detector that combines low-dimensional nanomaterials with the PTE mechanism. By exploring and leveraging the properties of 2D nanomaterials, the research seeks to achieve room-temperature photodetection while mitigating hot carrier transport limitations. The focus will be on integrating these advanced materials with suitable signal processing and data analysis algorithms to achieve efficient self-power conversion of infrared radiation into electricity. This approach offers advantages such as broad-spectrum radiation absorption and operation without needing bias support in ambient surroundings. Ultimately, the goal is to develop a controllable, cost-effective, and scalable fabrication process for the proposed infrared optoelectronic detector, enabling its practical implementation in various applications.

1.2 Thesis outline

This thesis will be organized in the following paragraph.

Chapter 2 introduces the background knowledge of light-electrical conversion mechanisms in PTE, photovoltaic (PV), pyroelectric (PE), and bolometers. Discuss each type of detector’s unique characterizations, detection range, domination noise, and response. Then, two types of 2D nanomaterials, graphene, and Mo_2C MXene, will be presented with their characterizations. Next, the investigation of polymer affinity in PTE light absorption, electrical conductivity, thermal conductivity, and flexibility will be addressed. Finally, figures of merit of PTE detection will be introduced.

Chapter 3 proposed doped PANI/graphene composites for PTE detectors. A high-performance, bias-free PTE detector is achieved utilizing vital π–π junctions in the doped-PANI/graphene composite and exhibits its applications in fingertips detection.

Chapter 4 presents flexible multi-element PTE detectors based on spray-coated graphene/PEI composites for multiple hydrophilic and hydrophobic substrates. Optimization of the spray coating method in compact alignment on various surfaces achieves significant photovoltage detectivity and responsivity.

Chapter 5 involves the room-ambient operation of integrated and visualized PTE systems with patterned Mo_2C/PEDOT: PSS flexible devices. Two potential systems—the motion tracking system and the NDT imaging system are proposed for human motion tracking and structural detection.

Chapter 6 summarizes the contributions of works and offers promising prospects for future PTE works.

Chapter 2 Background

2.1 Electromagnetic spectrum

The electromagnetic spectrum encompasses a vast range of wavelengths, each carrying unique properties and applications, as shown in **Figure 2-1**. Starting from the longest wavelengths, we encounter radio waves used for communication and radar, followed by microwaves utilized in cooking and wireless technologies. Beyond visible light, we venture into the terahertz range, where wavelengths measure from 1 millimeter to 100 micrometers. Terahertz radiation finds applications in security scanning [45], spectroscopy [46], and medical imaging due to its unique ability to penetrate various materials while being non-ionizing [47]. Moving further, we encounter infrared radiation, with wavelengths ranging from about 1 millimeter to 750 nanometers. Infrared radiation finds applications in thermal imaging [48], remote sensing [49], and communication [50]. Next comes the visible spectrum, the narrow band of wavelengths perceivable by the human eye, from approximately 750 nanometers (red) to 400 nanometers (violet). This slice of the spectrum allows us to perceive the vibrant colors of the world around us. Understanding the electromagnetic spectrum and harnessing its diverse wavelengths enables us to unlock a myriad of technological advancements and gain deeper insights into the universe.

This chapter focuses on utilizing photon energy to explore the fascinating world of light-matter interactions and photon-based technologies. Understanding how photons, the fundamental particles of light, can be harnessed and manipulated opens a realm of possibilities in various fields. We will delve into different types of detectors, such as PTE, PV, PE, and bolometers, each offering unique strengths and applications. Besides, we'll emphasize novelty PTE detectors using 2D dimensional nanomaterials and figures of merit.

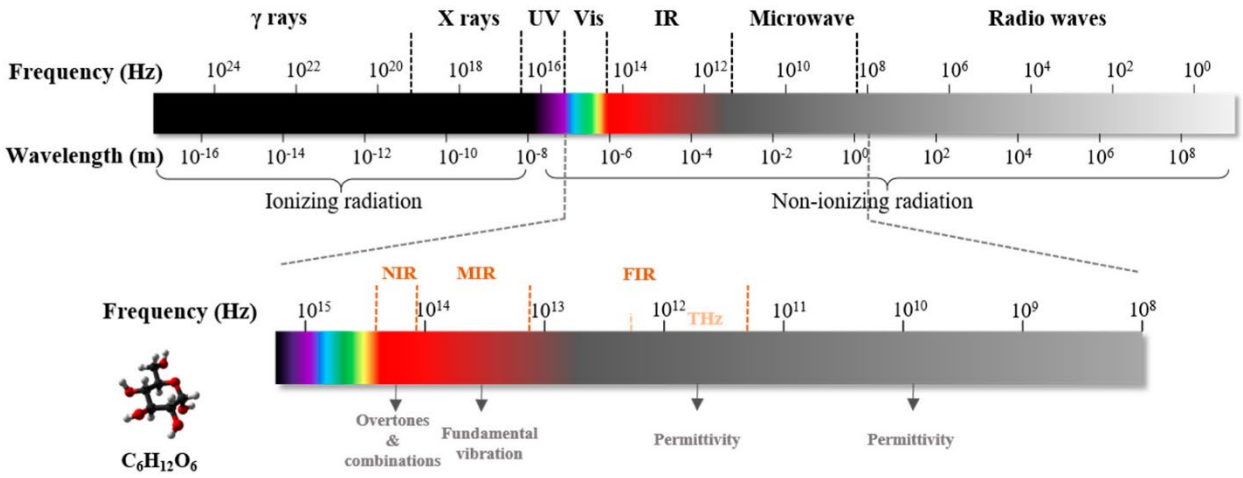

Figure 2-1. General electromagnetic spectrum with its relative wavelength [51].

2.2 Light-matter interactions and photon-based detectors

2.2.1 Photovoltaic detectors

Photovoltaic detectors switch photon energy into voltages by separating electron-hole pairs without any heat engine interface. The initial step of the PV process is the absorption of the photon energy. As the incident photon illuminates the solar cells, photons are passed through transparent electrode layers and absorbed by the donor/acceptor layer (or p-n junction layer in **Figure 2-2**), where photons excite the electron-hole pairs. The excited holes/electrons diffuse through their phase, decay, and dissociate at the donor/acceptor or p-n junction layers. This scenario is called the diffusion and separation stage. Next, moving carriers overcomes the boundary energy and diffuse the relative electrodes with external load, which can guide carriers to the flow path. The flowing continues until the depletion reaches its limitation, and the electric field starts to prevent further hole-electron pair diffusion. Finally, integration from the top and bottom electrodes leads carriers to return to diffuse lower concentration layers and repeatedly follow the previous steps [52,. 53]

Nanomaterials and nano/microstructure accelerate new p-n junction 3D PV detector innovations. Nanostructures with nanowires, nanopillars, nanocones, and quantum dots increase the absorbing surface and quantum confinement ratio, assisting photon absorption and carriers' collections.[54]

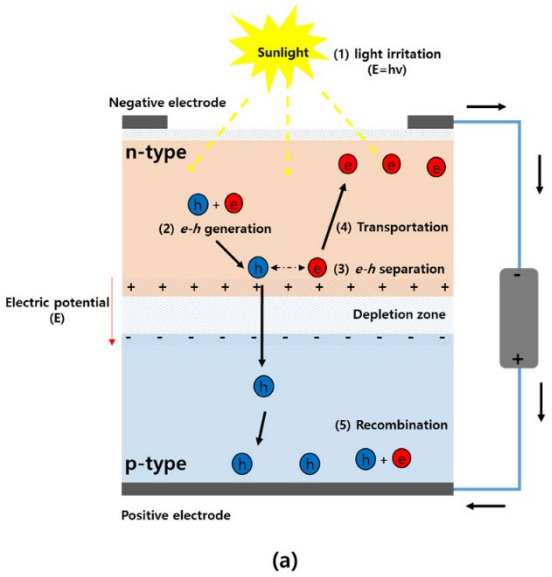

Figure 2-2. Working principle of solar cell with p-n junction structure [53].

Although it is the hot topic of photon-electric conversion research and various applications, including solar power cells, wearable textiles, remote buildings, intelligent vehicles, etc., the limitation of PV detectors is limited to inside defects and outside use range.

First is the limitation of the detector range. The PV effect requires an inter-band interaction in different properties of materials, which, in other words, means that the photon energy should be higher than the Fermi energy level for inter-band transition. And such bandgap limited the PV transition as bandgap is an intrinsic property of semiconductors and eventually has a direct influence on the photovoltaic cell voltage. Thus, only a limited range from near-infrared (NIR) to visible light is available for this transition.

Second, the low surface-to-volume ratio and slow-down reaction limit its efficiency. PV only exists in the localized junction interface, while PTE can be broad at different positions. Besides, the recombination of the electron holes always happens while the carriers move along the contractive layers. Next, the chemical reaction at the top layers prevents the long-term stability of PV detectors.

Finally, the PV is wavelength-dependent even in the near-infrared and visible light regions. When the power of the incident light increases, the raised photon energy cannot be fully converted into electric power, and the responsivity will decrease [55]. As for PTE, the increasing energy will speed up the photothermal conversion, and a more effective heat transition will appear for the next step of thermoelectric conversion.

2.2.2 Bolometer

As for the bolometer, the bolometer is a thermal sensor that transfers electromagnetic radiation in phonon energy. Bolometer depends heavily on temperature-sensitive materials. While incident the photon energy, the absorber is heated up to raise its temperature, following the change of the resistance of the bolometer membrane. The diode-based sensor can measure and convert such resistance change into electric output. Depending on the cooling systems, bolometers are divided into a cooled system with a heat sink **(Figure 2-3**) and an uncooled type at room temperature [56,. 57]

For cooling bolometer, it includes a light absorber, thermometer, insulation part, and readout circuit. The heat capacity and the response time can be regarded as the following equation[58]:

$$\alpha P = C\frac{dT}{dt} + G(T - T_0) \tag{2-1}$$

, where P is the incident power, α is the absorption coefficient, and T_0 is the initial temperature of sinking. During the cooling function, cryogenic are requested with specific gases. Such detector can be operated in broadband temperature range and sensitive for THz to far IR. While the uncooled bolometers are usually micro-chip based and limited to a specific range due to the room temperature fluctuation. Semiconducting materials, such as amorphous silicon and Vanadium oxide (VO_x), and metal/metal oxide, such as Ti, TiO2, ZnO, NiO, bifunctional nanomaterials like CNTs are preferred materials for their temperature-sensitive, resistance instability under various temperatures.

However, bolometers still have functional issues and noise problems in signal detection. As for cooling bolometers, cooling systems with cryogenic operation limited the portable and carry-on applications. Also, the operation of such bolometers requires enough room space. On the other hand, uncooled bolometers are pretty bothered by surroundings and fluctuations in the air. Such conditions will significantly affect resistance changing rates, even if most commercial materials only varied within 3%-5%. Besides, uncooled bolometers are restricted to narrow bands due to inefficient heat exchanges with surroundings. Furthermore, the involving heat change system leads to another noise in signals. The above equation reveals a simple conclusion that the bolometer temperature differences are proportional to the thermal conductivity. The limited issues with the bolometer are that the bolometer requires an external bias. Thus, an external $1/f$ noise is included in the performance, which leads to the overall performance being lower than PTE in some regions. Also, the I-V curve of the bolometer is non-uniform. Importantly, temperature stabilizers and cooling units are required to ensure the overall temperature differences maintain a stable value for resistance. Otherwise, the performance of the bolometer maybe not be stable. Therefore, such a bolometer is much larger than PTE devices.

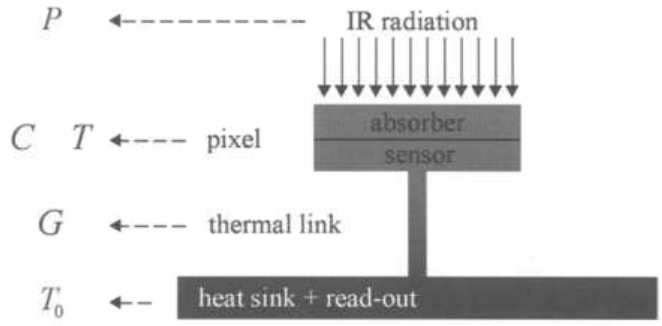

Figure 2-3. Schematic of a classical bolometer device with absorber, sensor, linking part, and heat sink [58].

2.2.3 Pyroelectric detector

A pyroelectric detector (shown in **Figure 2-4**) aims to transfer thermal energy into electrical energy via temperature fluctuation in polar materials. Electrical dipoles in the pyroelectric materials drive spontaneous polarization, leading the surrounding light particles to obtain negative or positive charges. Manipulation of an external circuit on both sides of the materials as electrodes intensifies opposite polarity through electrostatic induction. While positive temperature variation $\frac{dT}{dt} \neq 0$,

Electrical dipoles tend to oscillate at some degrees, weakening polarization and electrical balance, driving electronics in specific directions, and finally, external unbalance leading to electrical signal output [59–61].

To satisfy applications, pyroelectric materials can be divided into single crystals, ceramics, inorganic film, and polymer composites. Triglycine sulfate, perovskite structure in ceramics, $BiFeO_3$ (BFO), $Pb(Zr_{0.3}Ti_{0.7})O_3$, and PVDF/CuO are representative materials for power generation, hydrogen production, temperature sensitive, and sterilization.

However, pyroelectric materials suffer from surrounding temperatures, light fluctuation, and mechanical vibration. Poor long-term and electrical stability are still questionable for micro/nanofabrication. Besides, choppers are required to manipulate the energy induced by power supplies to avoid increasing temperature raising.

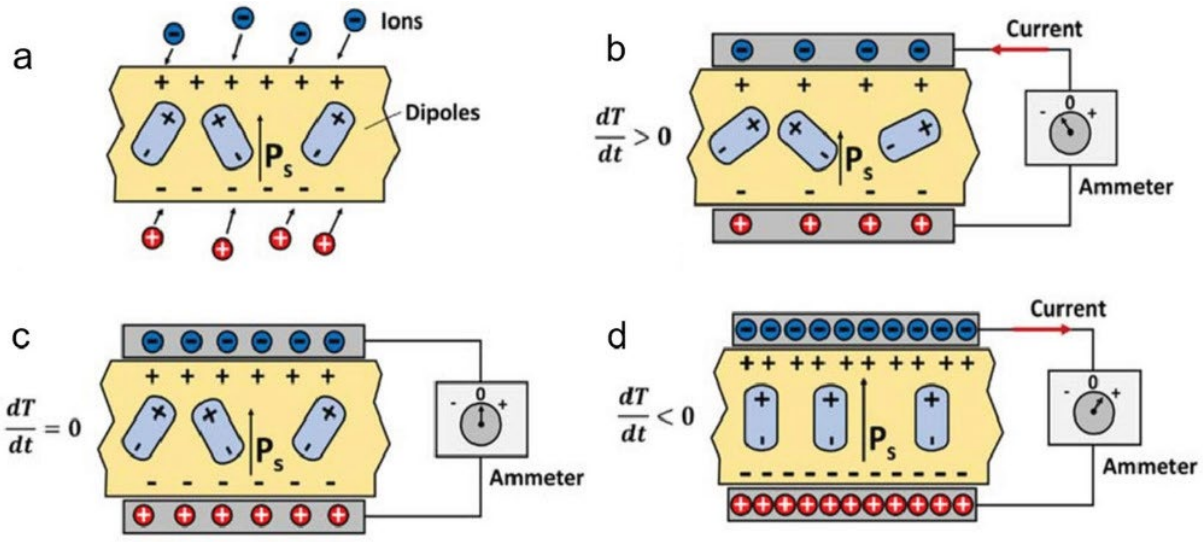

Figure 2-4. Conceptual model of pyroelectric generator. (a) Pyroelectric materials have dipole moments that add up to provide a spontaneous polarization; (b) Pyroelectric material between the two conductive electrodes of a capacitor. Temperature is held constant, and no current is in the steady state; (c) Increase in temperature decreases spontaneous polarization; (d) Decrease in temperature increases spontaneous polarization. Cyclic temperature change in pyroelectric materials generates alternating currents [62,63].

2.2.4 Photothermoelectric detector

The PTE mechanism can be divided into two consecutive methodologies; one is the photothermal effect, low-energy absorption with intraband and interband excitations, and the other one is the thermoelectric pathway with Seebeck coefficient in artificial asymmetries. The PET can absorb the photon energy and then convert it into temperature gradience, pushing the electronics diffusing

from warmer places to colder locations. As can be observed in **Figure 2-5**, the device is illuminated by the photo lights, absorbing the photon energy on one side of the detector. Then the photon excites the location temperature through molecular thermal vibration by lattice and electron carriers. The light-matter interaction continues, increasing temperatures in such vibrated thermal molecules in low-dimensional materials. Due to smaller thermal conductivities of electron carriers than lattices, facile photon-induced electrons are facile to diffuse, accompanied by the global temperature gradients. The Seebeck coefficient establishes the thermoelectric conversion as stable electronics flow with continuous photon energy.

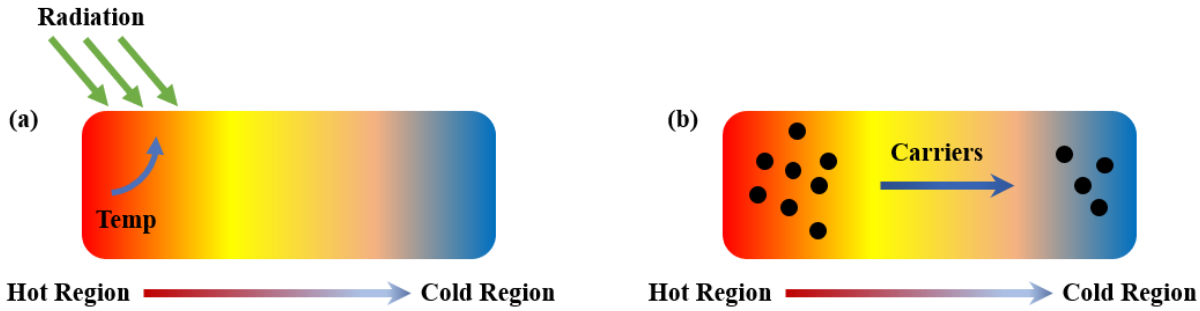

Figure 2-5. PTE conversion **(a)** photothermal conversion **(b)** thermoelectrical conversion.

Experimental expressions cannot entirely determine general photothermal conversion because of its complexity in intraband and interband excitations with electromagnetic waves changing from NIR/visible region to FIR/THz region [64, 65]. Also, low-dimensional materials in zero-dimensional (0D), (one-dimensional) 1D, and 2D are affected by various factors, such as illumination direction in optical anisotropy and defects factors in metallic/semiconductor composition [66, 67]. The overall photothermal conversion in the energy conversion method can be roughly concluded by

$$\Delta T = \frac{Q_{absorb} - Q_{diss}}{\sum C \cdot m} \quad (2\text{-}2)$$

, where ΔT refers to the temperature generated by photothermal conversion. Q_{absorb} is the photon energy that low-dimensional materials absorb. Q_{diss} is the heat dissipation during energy conversion. C is the specific heat capacity, and m is the mass of the material [33].

The Seebeck coefficient plays a significant role in thermoelectric conversion, where the temperature gradient guides the non-uniform charge density of the materials, thus generating the electrical field. These photon-induced electron electrons are diffused in N-type materials along the temperature gradient, while the P-type materials reverse the pathway. For semiconductors, the Seebeck coefficient can be described as

$$S = \frac{8L}{h^2} m_\rho T (\frac{\pi}{3n})^{2/3} \tag{2-3}$$

Where S is the Seebeck coefficient, L is the Lorentz number, m_ρ refers to the effective mass of the carrier, n is the carrier density [68]. The Lorentz number is a dimensionless number that relates the thermal conductivity of a material to its temperature and electrical conductivity. With Wiedemann–Franz law, the constant Lorentz number can be written as

$$L = \frac{\kappa}{\sigma T} = \frac{\pi^2}{3} (\frac{k_B}{e})^2 \tag{2-4}$$

Where κ is thermal conductivity, σ is electrical conductivity, and k_B is Boltzmann's constant [68, 69]. The Wiedemann–Franz law indicates one potential method to adjust the Seebeck coefficient by applying an external magnetic field, where the Lorenz force can impact the overall current by turning the direction of carrier density flow. In this circumstance, spin-dependent thermal effects and Lorentz force will increase carrier mobility in inorganic semiconducting materials [70]. Generally, the overall Seebeck coefficient in nanomaterials can be measured through the equation:

$$\Delta V = -S\Delta T \tag{2-5}$$

A thermal couple can measure the Seebeck coefficient of materials in a solid structure. The basic idea of the measurement is to utilize two different metal materials with known Seebeck coefficients. The unknown value can be obtained under the control of temperature differences:

$$S = -\int_{T2}^{T1}(S_2(T) - S_1(T))dT \tag{2-6}$$

However, such measurement can be influenced by several factors, such as the air surroundings with heat dissipation and the materials' shapes due to random diffusion along the temperature gradient. Besides the Seebeck coefficient, other impacts, including electrical and thermal conductivity, also determine the thermoelectric performance. Therefore, a figure of merit value ZT has been applied:

$$ZT = \frac{S^2\sigma T}{\kappa} = \frac{S^2\sigma T}{\kappa_l + \kappa_e} \tag{2-7}$$

Where σ is the electrical conductivity, a lattice κ_l and an electronic κ_e thermal conductivity [71]. Electrical conductivity can be written as

$$\sigma = ne\mu \tag{2-8}$$

, where μ is the carrier mobility. One expects high electrical conductivity, high Seebeck coefficient, and low thermal conductivity to achieve high thermoelectric conversion. However, most metal materials have a relatively low Seebeck coefficient [72]. As for the semiconductors, few relationships are associated with electric and thermal conductivity. Semiconductors usually have low electric conductivity in common working conditions. Dropping the thermal conductivity is essential for these semiconductors to achieve a high ZT value. The previous discussion involves an electric-phonon carrier, which assists in improving the Seebeck coefficient. And a phonon is

the primary carrier of thermal conductivity through the crystally structure vibration. The ZT value can be approached by suppressing the phonon-induced thermal conversion [73]. Multi-layer metal/polymer/metal thin-film in composites, introducing involving surfaces and composites, can improve phonon scattering [74].

Table 2-1 Comparison of PTE, PV, Bolometer, and PE detector

Features	PTE detector	PV detector	Bolometer	PE detector
Mechanism	Carriers/Lattices vibration and carrier flow with a temperature gradient	Electron-hole pairs combination and separation	Resistance fluctuation with temperature change	Polarity switch with temperature change
Detectivity range	Broadband THz to UV	Narrowband Visible	Broadband THz to IR	Broadband THz to Visible
External power Setup	Unnecessary	If Possible	Necessary	Necessary
Cooling system	Unnecessary	Unnecessary	If Possible	Unnecessary
Dominating noise	Thermal noise	Thermal noise, (1/f noise)	Thermal noise, Dielectric loss	Thermal noise, 1/f noise
Operation Room temperature	Yes	Yes	Likely	Likely
Response Speed	Fast	Fast	Slow	Slow

Table 2-1 compares multiple PTE, PV, bolometer, and PE detector features. As one can notice, PTE has superiority over the other three due to its broadband range from THz to UV, self-powered, room-temperature operations, low noise distribution, and fast response, shining as the new promising detection for various applications.

2.3 2D dimensional materials and polymer matrix

Low-dimensional nanomaterials, encompassing 0D, 1D, and 2D materials, have garnered significant attention and have been extensively applied as PTE sensing layer materials. Compared to typical 1D CNT array design, although CNT has superior high thermal conductivity, several considerations impede such CNT applied to highly efficient PTE detectors. First, the high dependence on incident light angle makes it hard for CNT to absorb the impedance light and bulk CNTs fully. Therefore, the photon incidence power has impacted, and overall PTE conversion will drop. Second, the fabrication of CNT arrays is quite complex and costly. CNT arrays required a CVD machine for hydrogen catalysis and bonding wires, leading to more circuit issues. Finally, CNT are fragile to outside forces. While scratching with tweezers or pins, the structure of such CNTS will be destroyed and cannot return to its normal work condition. For 2D carbon materials, the local fragment has less impact on overall carrier transportation, and most 2D carbon materials will not be impacted by the incident light angle. Due to their reduced dimensions, these materials exhibit unique properties and behaviors, making them excellent candidates for various sensing applications. In this section, we will focus on two exceptional nanomaterials, graphene and Mo_2C MXene, which have shown remarkable potential for enhancing the performance of PTE sensors.

2.3.1 Graphene

Graphene is a single two-dimensional layer of carbon atoms bound in a hexagonal structure [75]. Since it was founded and isolated from the multi-layers of graphite by Scotch tape in 2004, graphene became the most popular research material due to its unique perfect crystal structure and semi-metal properties. Viewing from the lattice structure of the graphene in **Figure 2-6**, each carbon atom is bonded with the other three neighbors with σ bond. Apart from the 2-D platform with σ bonds, in the perpendicular direction (z-axis), hybridized π-π* bonds exist and provide graphene's most special electronic properties. The valance band is formed with bonding pi states,

while the conduction band consists of anti-bonding pi states. These states are connected with 6 orthogonal points, i.e., Dirac points. Except for the zero-band gaps, the vibrational properties show the high thermal conductivity of graphene and the optical properties of photon-phonon scatterings and electron-phonon scattering [76].

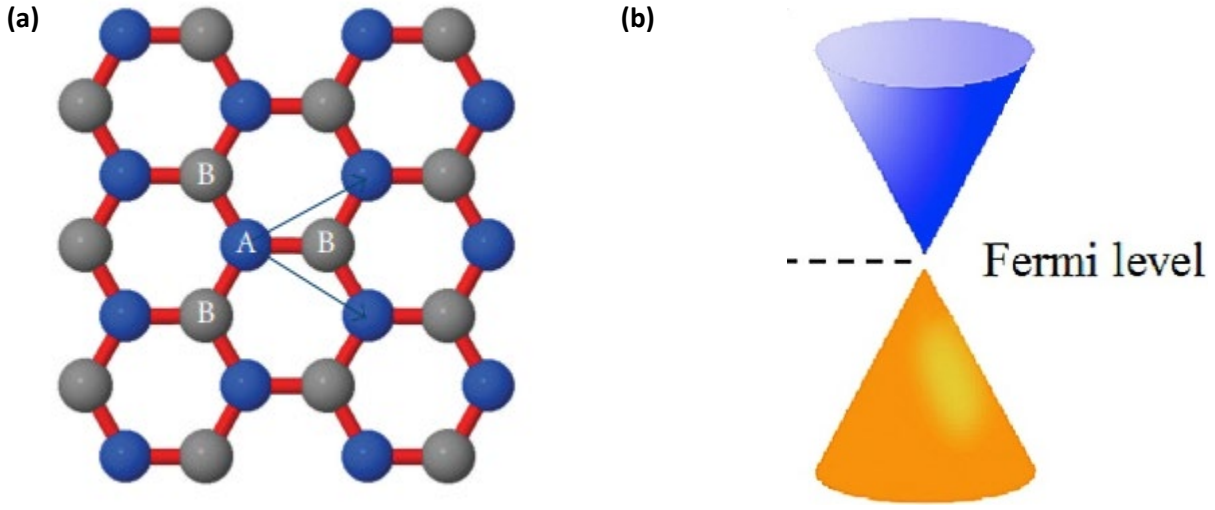

Figure 2-6. (a) An illustration of sublattices of graphene in 2D layer view, each atom has three bounded $\boldsymbol{\sigma}$ bonds with the neighbor atoms and one $\boldsymbol{\pi} - \boldsymbol{\pi}^*$ bonds in the Z axis [77]. **(b)** The bandgap structure of a single layer of graphene [78].

Intrinsic graphene obtains fast electronics Fermi speeding (around 10^6 m/s), stable optical conductivity of $2\pi e^2/4h$, where h refers to the Planck constant, universal absorption of 2.3% with a fine-structure constant α. **Figure 2-7** illustrates the broadband absorption of graphene and its relative optical transitions. Graphene is intended to interband transitions when the frequency reaches NIR to the visible region. However, while in the Mid-IR region, the Pauli-blocking prevents the optical absorption, leaving disorder of the materials to domain the main absorption. When the absorption reaches the THz part, the absorption prefers the intraband due to moving energy less than thermal energy. The overall absorption band demonstrates the potential for ultra-

band optical devices [79]. Besides the optical and high carrier mobility, exotic quantum phenomena owing to strong correlations recently demonstrated its tuning superconductivity in twisted bilayers [80, 81]. With the graphene accumulated to multiple layers, the semiconductor attributes and bandgaps make the potential for trade-in gate-controlled applications such as lasers, OLEDs, smart screens, and photodetectors.

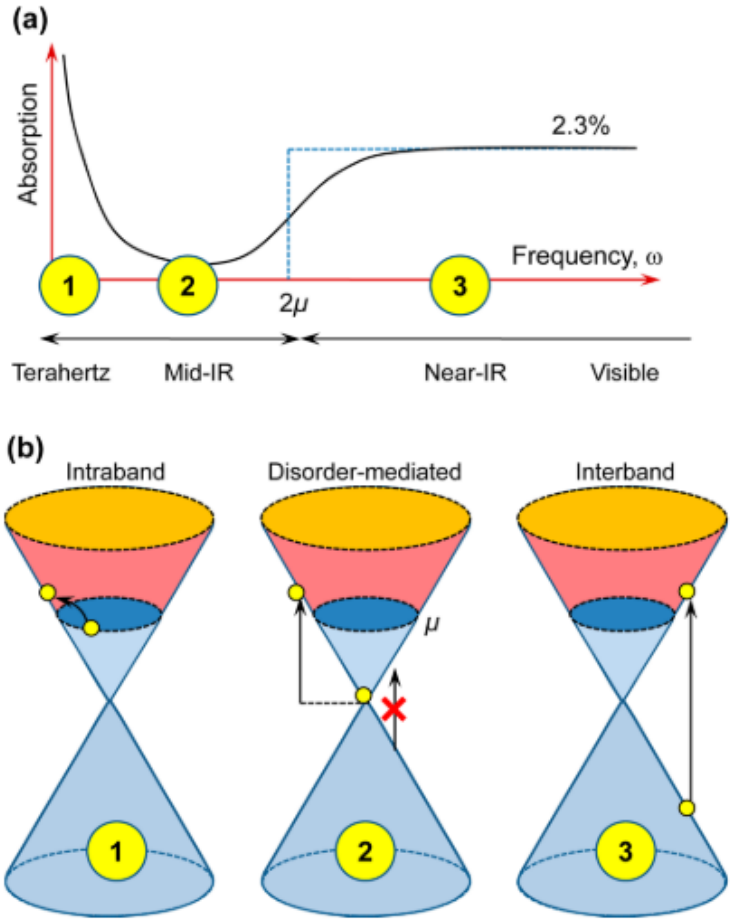

Figure 2-7. (a) Illustration of a typical absorption spectrum of doped graphene. **(b)** Illustration of the various optical transition processes [79].

Graphene was first invented by isolating exfoliated from graphite with tapes in 2004. However, such flakes are invaluable for research and industrial development due to their uncontrollable size, massive defects, irregular shapes, and uneven layers. Besides such defects of mechanical exfoliation, the requests for massive structurally coherent production, pattern/linear sequences, and precise layer manipulation. Since then, many researchers have investigated potential methods. One promising and stable approach is chemical vapor deposition (CVD). The CVD method uses metal/semiconductor method with nutritious carbon atoms attained alkanes and alkene gases such as acetylene (C_2H_2), ethylene (C_2H_4), and methane (CH_4) with protection gases such as hydrogen (H_2) to remove impurities [82, 83].

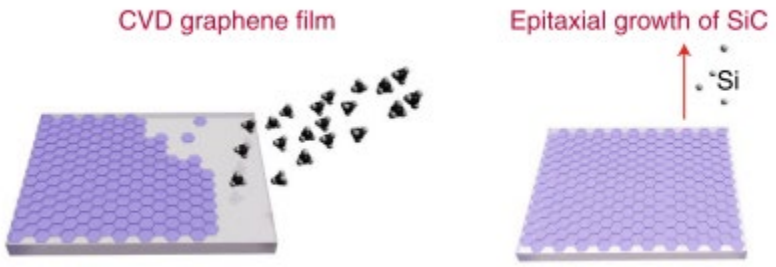

Figure 2-8. Production of graphene with CVD and Epitaxial method[82]

The carbon atoms are concentrated on the catalysis surface at high temperatures by the gradient of alkanes and alkene gases. Then, the carbon atoms segregate the catalysts to form single or multiple layers. Various metal catalysts, such as Pt, Ni, Fe, Co, and Cu, and direct growth using semiconductors like SiC are widely adapted, as shown in **Figure 2-8**. The laboratory scale flask satisfies the research chip requirement in Figure 2-9 and Table 2-2 by combining new transfer methods like wet, bubble, dry, and rolling transfer. However, the transferring/growing methods' current state is still limited to achieving massive production with the desired quality, yield, and

scalability [84]. Crakes, contaminations, expensive operations, and time-consuming challenges require more solutions and optimizations to operate stable transfer of growth layers.

Table 2-2 Methods of transferring graphene

Methods	Principle
Wet transfer	Ionic etchants+liquid cleaning solvent to target substrates
Bubble transfer	Bubble delamination with electrochemical reactions/chemical reaction
Dry transfer	Repeatable thermal peeling off with ionic liquids/releasing tapes
Rolling transfer	Hot laminator, with electrochemical delamination from metal surface

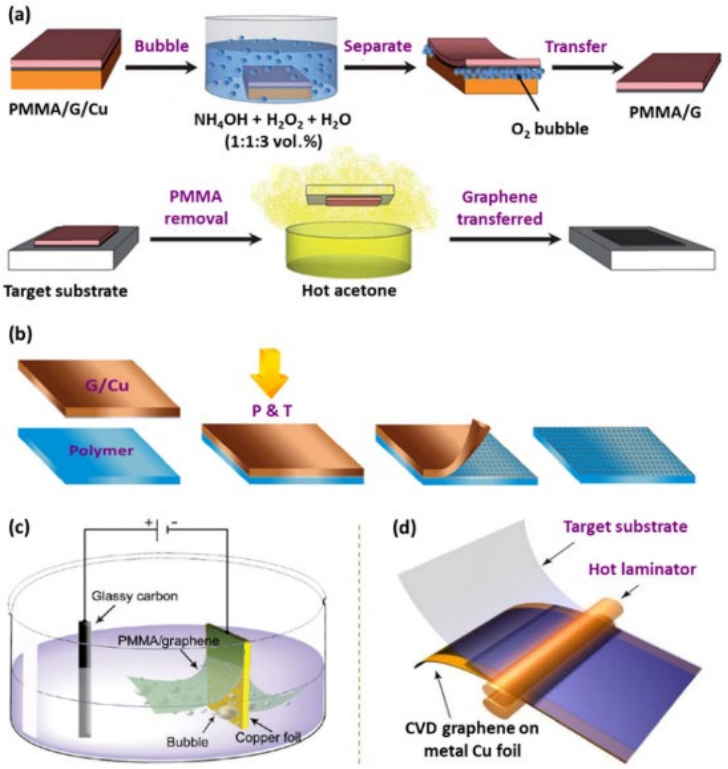

Figure 2-9. Schematic diagrams of typical transfer routes. (a) Non-electrochemical reaction-based bubble-mediated transfer [85]. (b) Dry transfer route [86]. (c) Electrochemical delamination [87]. (d) Scalable roller-assisted delamination transfer method [84, 88].

2.3.2 Mo_2C MXene

Transition metal carbides (TMCs) are a family member of 2D MXenes, siblings of transition metal nitrides and carbonitrides. MXenes start with a formula of $M_{n+1}X_nT_x$, where M represents 3d-5d block transition materials (n=1-4), interleaved by X layers. X stands for carbon or nitrogen material, and T_x refers to a mixture of –O, –F, –(OH), or –Cl surface groups [89, 90]. MXenes are synthesized by removing the A layer in MAX material through hydrofluoric acid or molten salt etching (**Figure 2-10**). The unique cooperation and modification of MXenes in metal and ceramic matrix composites assist applications as catalysts, supercapacitors, electrodes, and energy harvests. MXenes obtain unique electrical conductivity, electrochemical activity, solubility, mechanical strength, and polymer affinity by turning surface functional groups [91].

The electronic properties of MXenes usually depend on the nature of its original transition materials with surface terminations. Metallic to semiconductor properties, small band gaps perfectly match the UV to NIR range due to the high density of states at the Fermi level [92, 93]. Experiments also demonstrate the broadband optical absorption from THz to IR region with MXenes materials [32, 94].

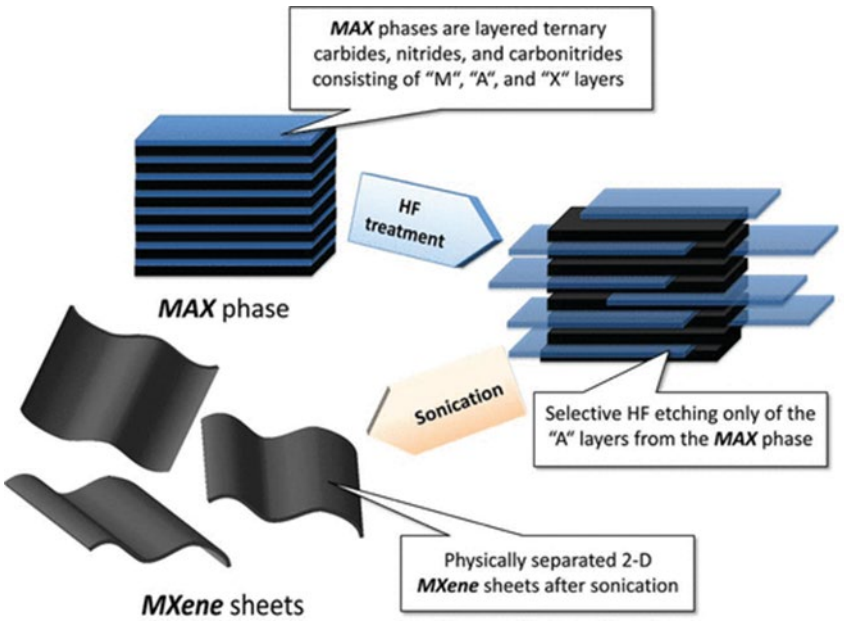

Figure 2-10. Schematic for the exfoliation process of MAX phases and formation of MXenes [95].

Molybdenum carbide (Mo_2C), a two-dimensional transition metal carbide nanomaterial, has garnered significant attention for its wide range of applications. Its unique properties, such as superconductivity [96], low thermal conductivity [97], robust resistivity [98], and corrosion resistance [99], have led to recent achievements in various fields.

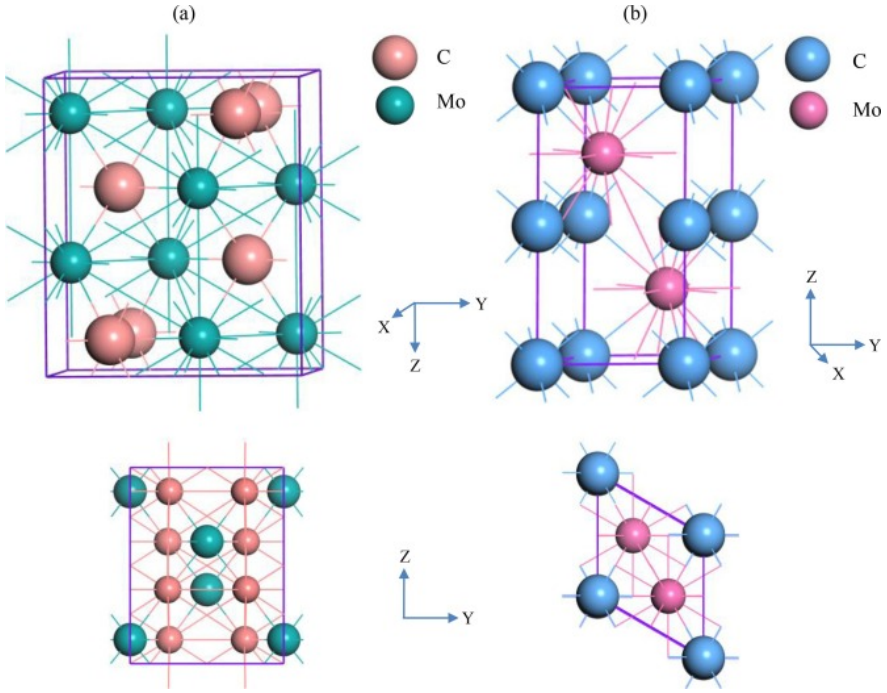

Figure 2-11. The cell structure of Mo_2C [100].

High symmetry of Mo_2C MXene in the armchair and zig-zag directions (**Figure 2-11**); these structural parameters imply that the molybdenum atoms bond strongly with carbon atoms. The DOS simulation indicates its metallic characterization with a large density of states (DOS) around the Fermi level. Such DOS near the Fermi level proves the superconductivity of Mo_2C. Also, relatively low thermal conductivity (48.4 W m^{-1} K^{-1}) compared to graphene makes it possible for

thermoelectrical material. A sizeable elastic modulus (312 GPa) is attributed to a strong interaction between molybdenum and carbon atoms, indicating its superior in robust strain-supportable materials. These include gas-evolution nano electrocatalysts [101], bifunctional electrodes [102], electromagnetic interference shielding [103], and photoelectric detectors [104]. Mo_2C has shown promise for broadband detectivity and carrier mobility due to its high Fermi density [105, 106].

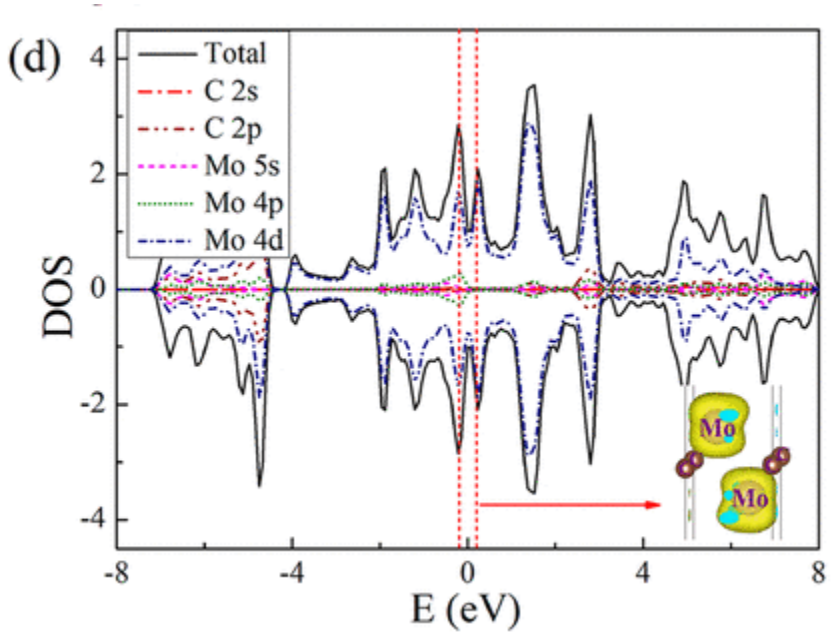

Figure 2-12. The electronic DOS of the MXene in which the projected DOS of each atomic orbital is provided [106].

A hybrid of phototransistors with Mo2C/MoS2 with broadband detection in visible to NIR range is fabricated by Jeon et al [107]. Efficient hot carriers at the interface improve plasmonic resonance, demonstrating its low Schottky barrier height. High responsivity and light-to-dark current ratio also provide new sights for the next generation of photoelectric devices. As shown in **Figure 2-13**, The responsivity is almost independent of wavelength, and even in the IR range, the light-to-dark current ratio maintains a high visible range level. Their performance indicates the plasmonic resonance of visible light to IR period absorption.

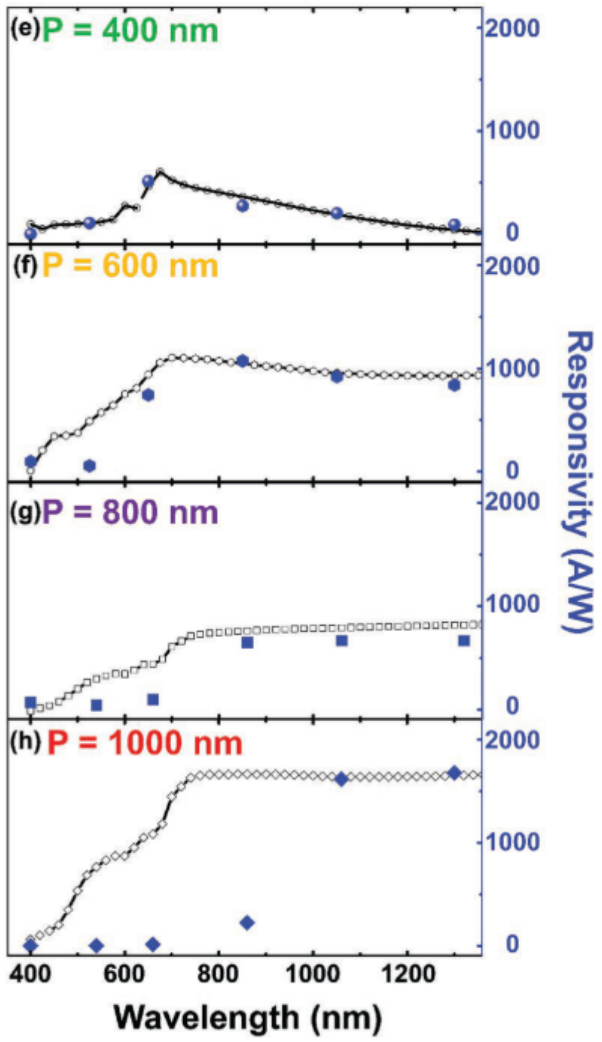

Figure 2-13. Tunable photoresponse using various pattern periods. Simulated normalized extinction cross-section spectra and measured responsivity from the MoS_2/p-Mo_2C hybrid structure with pattern periods of 400, 600, 800, and 1000 nm, respectively [107].

The synthesis of Mo_2C has been grouped into powder form and film form categories. The powder form of Mo_2C is usually synthesized through direct carburization and temperature-programmed reaction of molybdenum oxide at 1000 °C temperature. $MoCl_5$ and MoO_3 deposited on a carbon form structure with H_2/C_2H_4 reaction by CVD method provide a potential hybrid and heterojunction structure design strategy for layer deposition [108].

2.3.3 Polymer matrix

While considering photon absorption, the polymers are utilized to mix with suitable acceptors, themselves acting as donors [109, 110]. This approach will create heterostructures in sandwich structures. Also, for broadband nanomaterials, the priority of polymers is to provide matrix structure for dispersion, increasing contacting surfaces of nanomaterials and assisting in scattering the photons into absorption materials.

For conducting polymers, the sp^2 hybridization of the structure assists in conducting free carriers in the polymer matrix due to the free excitation of π bonds. The reason behind such conducting polymers is the massive percentage of quinoid and benzenoid structures with π- π junctions. Besides, controlling doping and polymerization rates helps to establish narrower bandgaps for charge transport and behave metallic properties. Furthermore, such fruitful quinoids and benzenoids have crystalline domains and relatively low disordered structures. Metallic carriers prefer to flow through crystalline domains, leading to high carrier mobility. At the same time, disordered areas strike free carriers with thermally assisted hopping at low frequency, inducing them to slow down. Variable range hopping and mobility edge models are known theoretical models that describe electronics moving in disordered areas and metallic zones. Unlike semiconductors, which will increasingly enlarge thermal conductivity for thermoelectric conversion, conductive polymers seldom impact overall value due to the amorphous morphology. Therefore, involving conductive polymers will improve the overall proficiency of PTE conversion. Classical conductive polymers are polyacetylene, polyaniline (PANI), polythiophene, polypyrene, and Poly(3,4-ethylenedioxythiophene): Poly(styrene sulfonate) (PEDOT: PSS) [111–114].

The carbon chains provide flexibility in a segment of polymers, the mass proportion of which will provide an internal rotation degree of freedom. Cross-linking structures like amide/ester will

increase the rigidity, forming H-bond branching between chains. Besides, the degree of crystallinity in polymers also determines flexibility. The more crystallinity in polymers, the less flexibility will emerge.

2.4 Figures of merit of PTE detectors

2.4.1 Responsivity

Responsivity (R_v) is defined as the ability of the detector to convert input radiation power to output electrical signal.

$$R_v = \frac{V}{P_{in}} \tag{2-8}$$

Where P_{in} stands for the input energy, the unit of the responsivity is usually V W^{-1}.

2.4.2 Detectivity

Detectivity (D^*) is defined as a device that can differentiate the minimum signal input from the surrounding noise within practical areas. High detectivity can usually detect minimum signals. Detectivity can be written as

$$D^* = \frac{R_v\sqrt{A}}{P_n} \tag{2-9}$$

Where A refers to the illumination area, P_n stands for the noise equivalent power (NEP).

2.4.3 I-V curves

I-V curves contain two lines. One is the dark surroundings, and the other is the illumination curve. Both lines should be straight as the overall resistance of PTE detectors remains stable without any fluctuation. Besides, the dark curve should go through the original point. The slope of each line is the resistance.

2.4.4 Noise and NEP

The PTE device is a free-bias and self-powered detector. Therefore, only John-Nyquist noise (thermal noise) should be considered. NEP (noise equivalent power) is another equivalent formula to judge the noise effect, and it is calculated as the following:

$$P_n = \sqrt{4k_B TR} \tag{2-10}$$

Where k_B is the Boltzmann constant. Low noise values usually mean a downward effect on the precise detection of the PTE devices.

2.4.5 Response time and cycling

The response is generally based on cycle testing with the power source on or off by taking 90% value from the current upgrading differences. The switching period is determined as the response time. And periodically cycling on/off devices, one can obtain the signal cycling time.

2.4.6 Seebeck coefficient

To determine the Seebeck coefficient in the whole device, one homemade system with thermometers made with two different Seebeck coefficient S_A and S_B metal lines is applied to measure the Seebeck coefficient of PTE detectors precisely.

$$V_1 = S_A(T_o - T_H) + S(T_H - T_c) + S_A(T_c - T_o) \tag{2-11}$$

$$V_2 = -S_B(T_o - T_H) + S(T_H - T_c) - S_B(T_c - T_o) \tag{2-12}$$

$$S = \frac{S_A V_2 + S_B V_1}{V_2 - V_1} \tag{2-13}$$

, where T_o is the room temperature, T_H is the heater temperature and T_c is the cooler temperature. According to the above equations, the term air temperature is eliminated during the subtraction from V_1 to V_2.

2.4.7 ZT value

A figure of the merit value of ZT is expressed in section 2.2.4. The dimensionless ZT value can indicate the ability of thermoelectric conversion. Larger ZT usually obtains higher Seebeck coefficients, high carrier mobility, and low thermal conductivity.

Stable and high-efficiency PTE detectors usually obtain high responsivity, large detectivity, stable resistance under dark and illumination surroundings, fast response, high Seebeck coefficient, and high ZT values.

Chapter 3 Doped Polyaniline/Graphene Composites for Photothermoelectric Detectors

3.1 Aims and highlights

In this work, we raised new doped PANI as the composite material with a few layers of a graphene sheet. First, doped PANI improves the PTE conversion in detectors. As a conductive nitrogen polymer with a slight 2.8 eV bandgap, PANI enhances the electrical conductivity of the whole composite [115]. Next, a peak photoresponsivity of 2.5 V W^{-1} and detectivity of 6.8×10^{7} cm $Hz^{1/2}$ W^{-1} are achieved within broadband detection. Furthermore, we investigated the potential of the semi-transparent array and flexible features. Finally, non-contact fingertip experiments demonstrate high sensitivity for detecting human body emission with 10 μV spontaneous radiation photoresponse. Our investigation shows this is the first introduced doped-PANI materials in PTE detectors with demos in multi-array detectors.

3.2 Experimental section

3.2.1 Synthesis of doped-PANI/graphene composite

Figure 3-1 illustrates the formation of the doped-PANI/graphene photodetector. The synthesis of doped PANI by HCl, 37% concentration, purchased from Sigma-Aldrich begins with a typical oxidative polymerization. First, 200 μL Aniline (purchased from Fisher Chemical, Certified ACS) is dropped into 25 mL 1M HCl solution, carefully stirring for 30 mins at room temperature. Then the whole dispersion is transferred under an ice bath at 0 ℃ and continues stirring until the solution turns green. Finally, the mixture is maintained for polymerization at the abovementioned cooling system for ten hours. The resulting dark-green mixing solution was filtered and washed out with

deionized water and ethanol alternatively, followed by drying out at a vacuum heat oven at 60 ℃ overnight in the form of powder.

Apart from avoiding aggregation and recombination of graphene layers, graphene powder (Purchased from Nanochemazone, purity≥97%) with various weight portions (from 5 wt% to 40 wt%, in increments of 5 wt%) is firstly dissolved with adequate DMSO (99.9%, purchased from Sigma-Aldrich). Then, the synthesized doped-PANI power is added to fully dissolve with magnetic stirring for four hours at room temperature and a further ultrasonic bath for one hour. Finally, the homogenous solution was evenly dropped and cast onto a plasma and isopropyl alcohol-treated PET substrate for 48h in slow drying at 35 ℃ ambient conditions (**Figure 3-1(a) to (c)**).

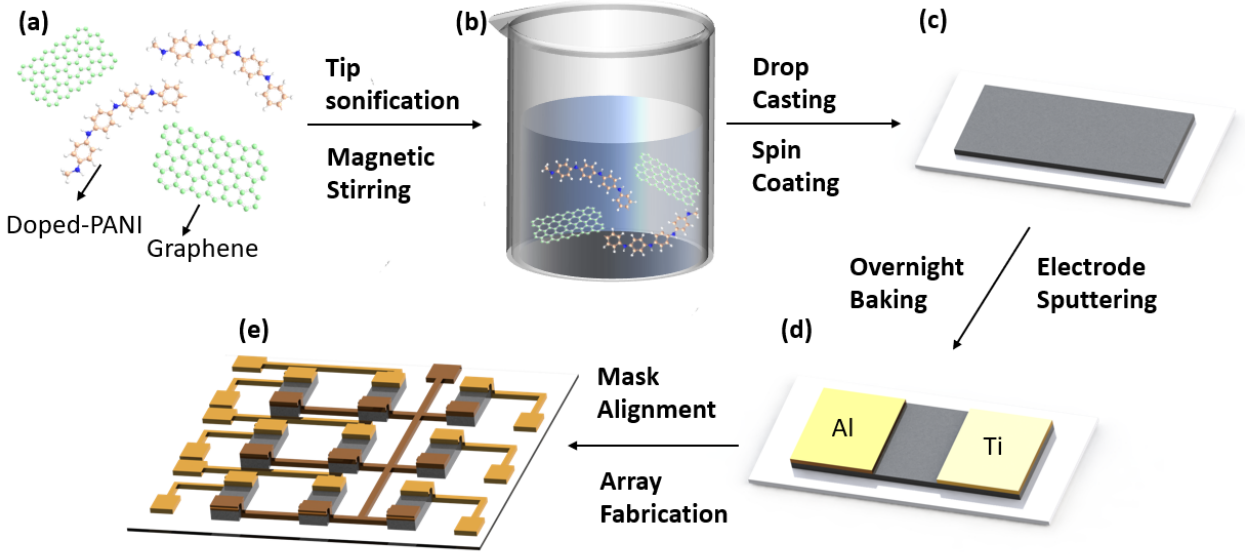

Figure 3-1. Solution synthesis and fabrication process of doped-PANI/graphene composite on substrates. **(a)** Synthesized doped-PANI/graphene composite. **(b)** Tip sonification and magnetic stir to thoroughly mix the composite. **(c)** Drop cast the mixture on a processed PET substrate. **(d)**

Material membrane formation and electrode deposition. **(e)** A 3x3 pixel array structure with 30nm electrodes.

3.2.2 Device fabrication

On the top of the doped-PANI/graphene composite, 120 nm Al and Ti symmetric electrodes are deposited via magnetron sputter deposition (AJA-sputter), structured by a laser-involved shadow mask pattern. The channel length for each photodetector is 1 mm. Conductive wires are connected by silver conductive epoxy (MG Chemicals 8331D Silver Conductive Epoxy Adhesive), waiting for 12 hours in the ambient environment to dry out (**Figure 3-1(d)**). As for the flexible 3x3 pixels detectors array, both electrodes decrease to 30 nm height, controlled by a precise mask technique rather than photolithography (**Figure 3-1(e)**). Finally, the overall 3x3 pixel doped-PANI/graphene detector is depicted in **Figure 3-2**.

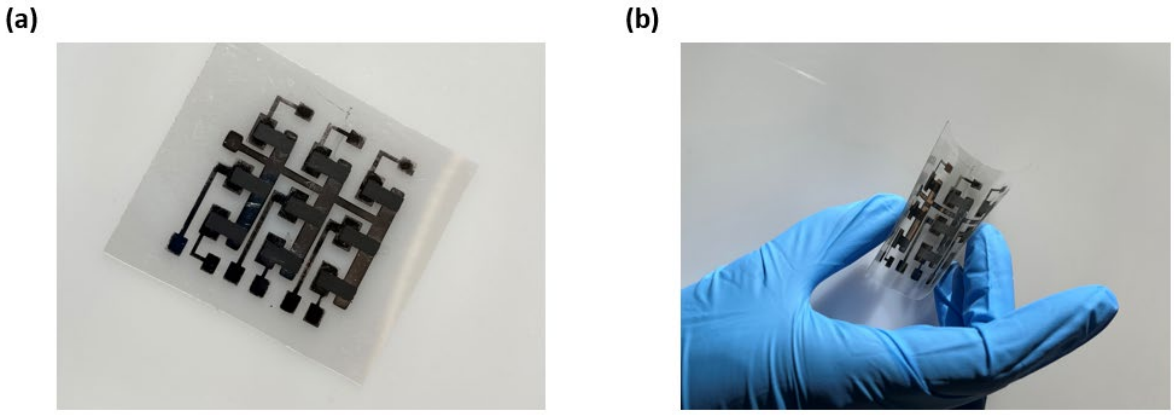

Figure 3-2. A 3x3 pixel doped-PANI/graphene detector.

3.2.3 Characterization

Doped-PANI/graphene composites' morphologies are observed on a JEOL JSM-7200F Scanning Electron Microscope (JEOL-SEM) at 5 kV voltage and 8 nA current. Raman spectrum is obtained

from Bruker Senterra-2 Raman with a 532 nm laser source. The UV-Vis spectrum is observed by PE Lambda 35 &1050 UV-Vis from 350 to 700 nm. In addition, the Seebeck coefficient of the composite is investigated from a homemade thermal-couples platform (**Figure 3-3**), and the thermal image (**Figure 3-4**) is obtained from Hti-Xintai thermal imaging camera HT-19. A low-intensity blackbody facility (Newport Oriel 67030) is applied as the radiation source. This broadband source starts from 573 K to 1173 K, with 200 K as the step temperature. All photodetectors are placed 50 mm away from the source. A specified germanium IR lens has been applied between the testing devices and the blackbody, aiming to block heat and allow the transmittance of IR radiation. Keithley 6487 and Keithley 6500 multimeters engaged the voltage characteristics of I-V curves. Other response time experiments and non-contact tip tests are measured by Keithley 6500.

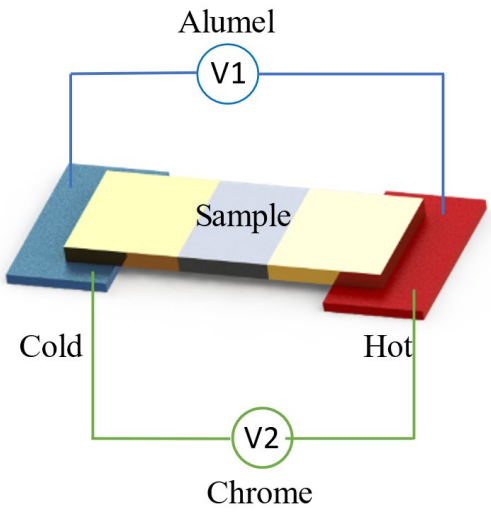

Figure 3-3. A homemade Seebeck coefficient system. Two thermometers are applied in this system.

Figure 3-3 shows the Seebeck coefficient measurement system with two thermometers made with alumel (-18 μV K-1) and chrome (22 μV K-1) to determine the Seebeck coefficient of materials. This system can precisely measure the Seebeck coefficient of low-dimensional graphene materials with polymers without the effect of room temperature:

$$V_1 = 22(T_o - T_H)+S(T_H - T_C)+22(T_C - T_o) \quad (3\text{-}1)$$

$$V_2= -18(T_o - T_H)+S(T_H - T_C)-18(T_C - T_o) \quad (3\text{-}2)$$

$$S = (22V_2+18V_1)/(V_2- V_1) \quad (3\text{-}3)$$

Where T_o is the room temperature, T_H is the heater temp, and T_C is the cooler temperature.

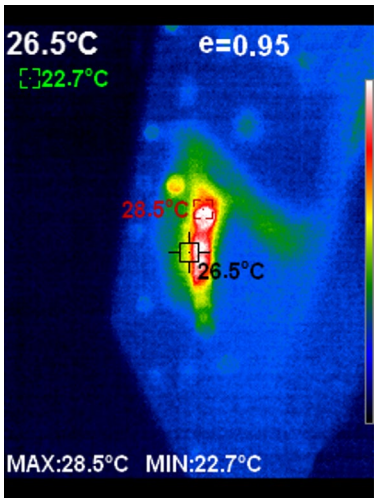

Figure 3-4. Thermal image of a doped-PANI/graphene detector. The bar scale starts from 22.7 ℃ to 28.5 ℃, and the room temperature is 22.7 ℃. The highest temperature in the IR image indicates our materials are not moderately affected under high blackbody radiation temperatures.

3.3 Result and discussion

3.3.1 Material characterization

The Raman curves of doped-PANI/graphene can be viewed in **Figure 3-5**. A typical band of D band (1350 cm^{-1}), G band (1580 cm^{-1}), and 2D band (2685 cm^{-1}) can be viewed in a pure graphene spectrum. These bands can be interpreted as defects in materials, the primary vibration of sp^2-hybridized carbon zones, and modified resonant processes due to the dispersion of split electrons or phonons in stacking layers [116].

The Raman spectrum also confirms general doped PANI materials. The doped PANI curve shows quinoid units of C-H interactions in 2D plane 1164 cm^{-1}, the C-N stretching band in 1344 cm^{-1}, and the C=N stretching of quinoid di-imine units C=C stretch bonds in 1590 cm^{-1}. Compared to Raman curves of pure graphene and doped PANI, the doped-PANI/graphene composite curve at 30 wt% graphene loading differs, including 1570 cm^{-1} and 1352 cm^{-1} bands appearing [117].

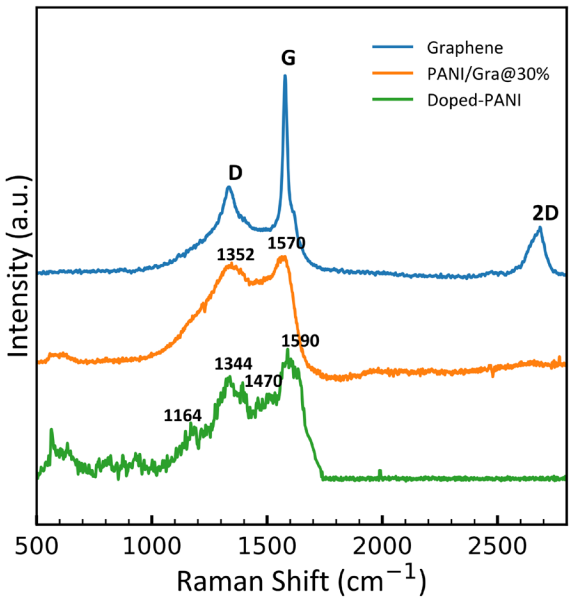

Figure 3-5. Raman Spectrum of pure graphene, doped-PANI/graphene composite at 30 wt% graphene loading, and pure doped-PANI.

UV-Vis spectrums of pure graphene, doped-PANI/graphene composite at 30 wt% graphene loading, and pure doped-PANI are presented in **Figure 3-6**. One critical absorption band (450 nm) shows at the doped-PANI curve and doped-PANI/graphene composite at 30 wt% graphene loading curve, while the graphene curve shows no absorption band appearing in the range of the testing band [118]. The peak band refers to PANI's polaron–π* band transitions. Besides, the peak shift from doped-PANI to doped-PANI/graphene composite at 30 wt% graphene loading suggests polarons from localization to delocalization with a more flattened shape from compacted coils [119]. More ordered regions in doped-PANI/graphene composite appear, strengthening the π–π conjugation and assisting in PTE conversion [120].

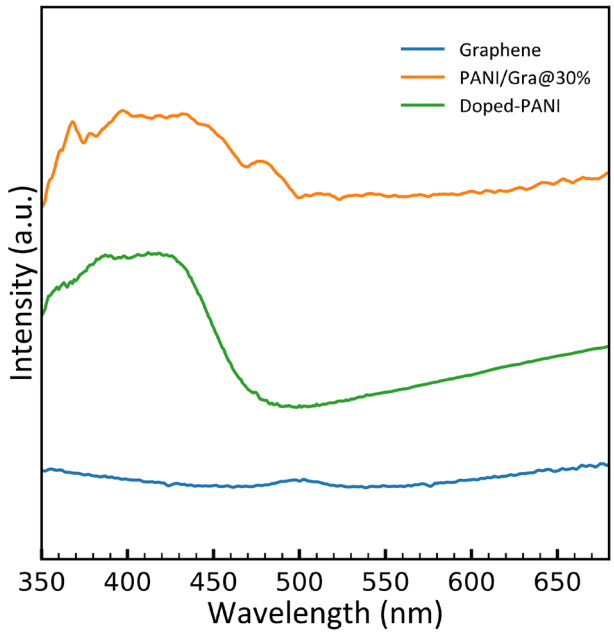

Figure 3-6. The UV-Vis spectrum of pure graphene, doped-PANI/graphene composite at 30 wt% graphene loading, and pure doped-PANI.

The Raman curves, SEM image (**Figure 3-7**), and UV-Vis curves of doped-PANI/graphene demonstrate that involving N-atoms enhances the strong interactions of atoms with a wide range of π- π interactions. Besides, the peaks shift from the original ones also supports strong interactions. Besides, new synthesis material can extend the nanomaterial structure to an expanded sheet structure, leading to a high and broad electron movement and strong sp^2 π- π interactions [121, 122]. The SEM image covers the uniform dispersion of nanomaterials with solutions in a polymer component.

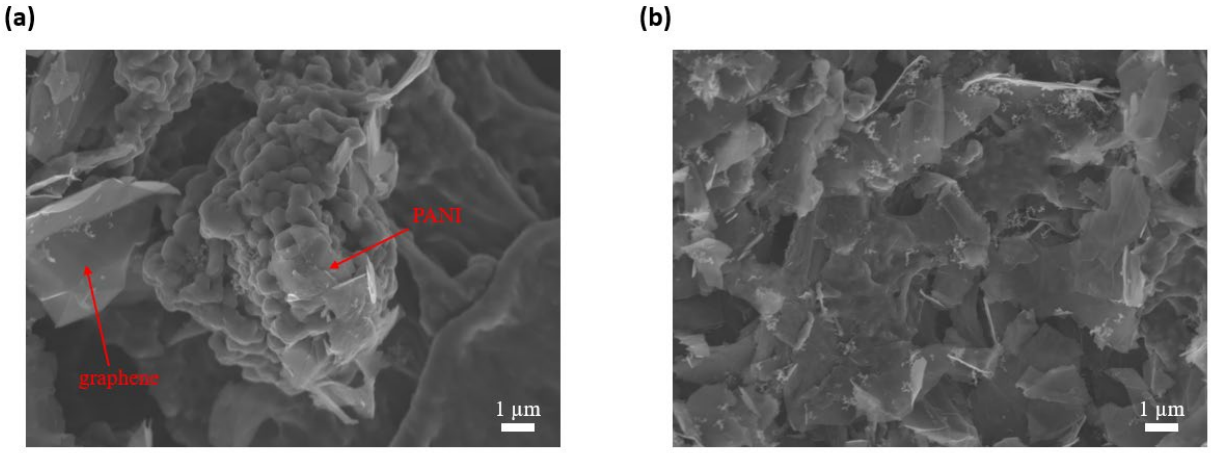

Figure 3-7. SEM image of doped-PANI/graphene composite at 30 wt% graphene loading. The scale bar is 1 µm.

3.3.2 PTE detector's photoresponse measurement

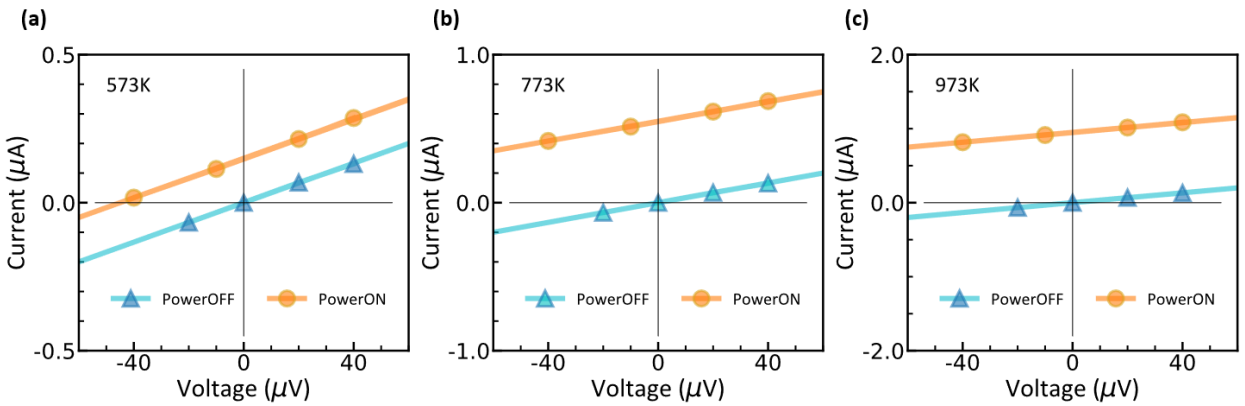

Figure 3-8. I-V curves of doped-PANI/graphene PTE detectors under various blackbody source power with on and off illumination. **(a)**573 K. **(b)**773 K. **(c)**973 K.

A set of current-voltage (I-V) curves is illustrated in **Figure 3-8**. The I-V curves of the doped-PANI/graphene photodetector are illuminated from 573 K to 973 K, and their dark environment is the comparison. And devices photovoltages are measured from -40 μV to 40 μV. All dark I-V plots strictly pass through the original points without bias voltages. Generally, the stability and uniformity of 300Ω are achieved under dark and illuminated circumstances. The PANI materials are not affected under high temperatures due to most heat blocking from the IR lens. (**Figure 3-4** and **Figure 3-9**).

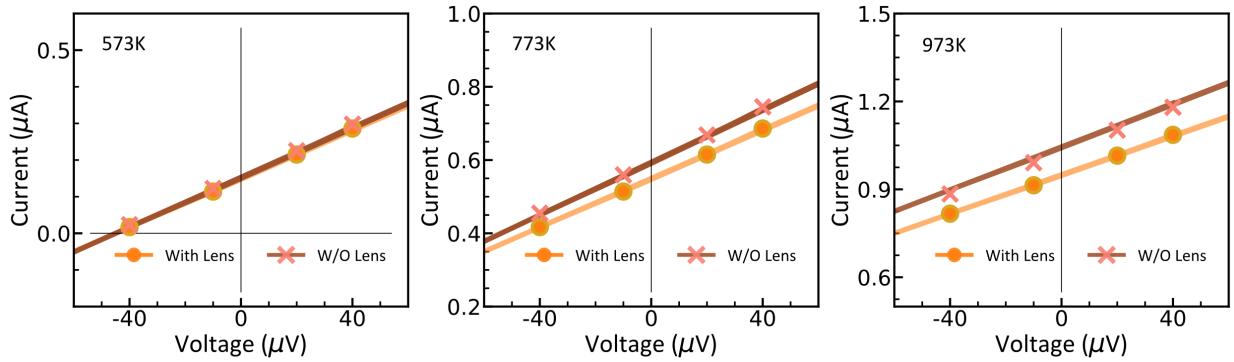

Figure 3-9. Comparison of current changes in/without a germanium IR lens. The current drops within 2.0%, 5.0%, and 8.4% under **(a)** 575K, **(b)**773K, and **(c)**973K, respectively.

Their photocurrent response under 773 K, 973 K, and 1173 K incident light illumination are shown in **Figure 3-10**. Multiple responses are tested with the radiation on/off duty cycles. Each relatively fast and stable transition time is achieved within 8-12 s, accompanied by a 6 s raising time. This durable achievement depends on the fast doped-PANI/graphene thermal equilibrium among specific channel lengths, soft but uniform substrates, and high Seebeck coefficient electrode selections.

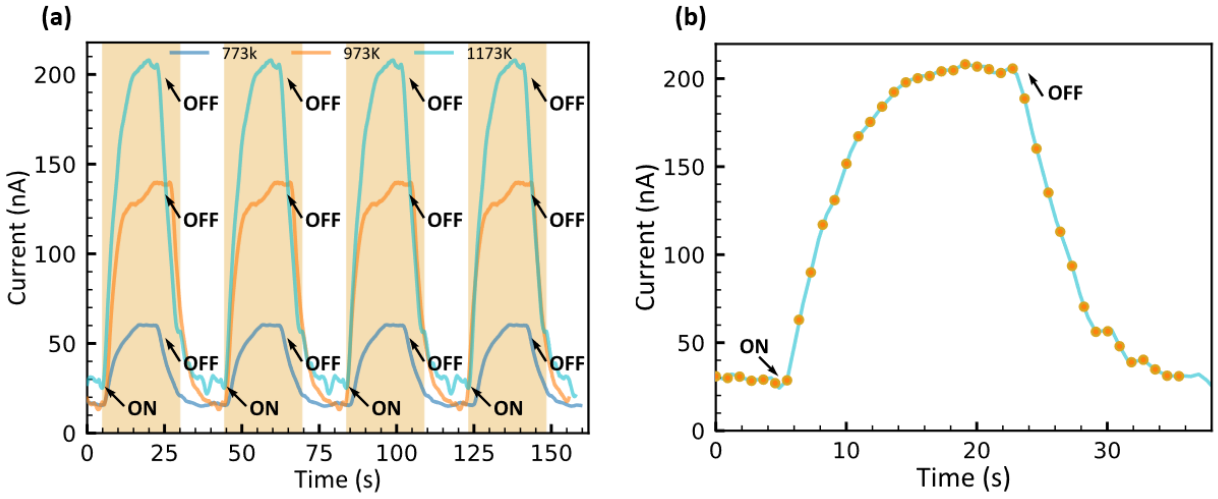

Figure 3-10. Photoresponse time of 30 wt% graphene loading under various blackbody power illumination. **(a)** Cycling of PTE detector response in 773K, 973K, and 1173K. **(b)** Time response of doped-PANI/graphene photodetector in 773K.

3.3.3 Photoresponse regarding impacting factors

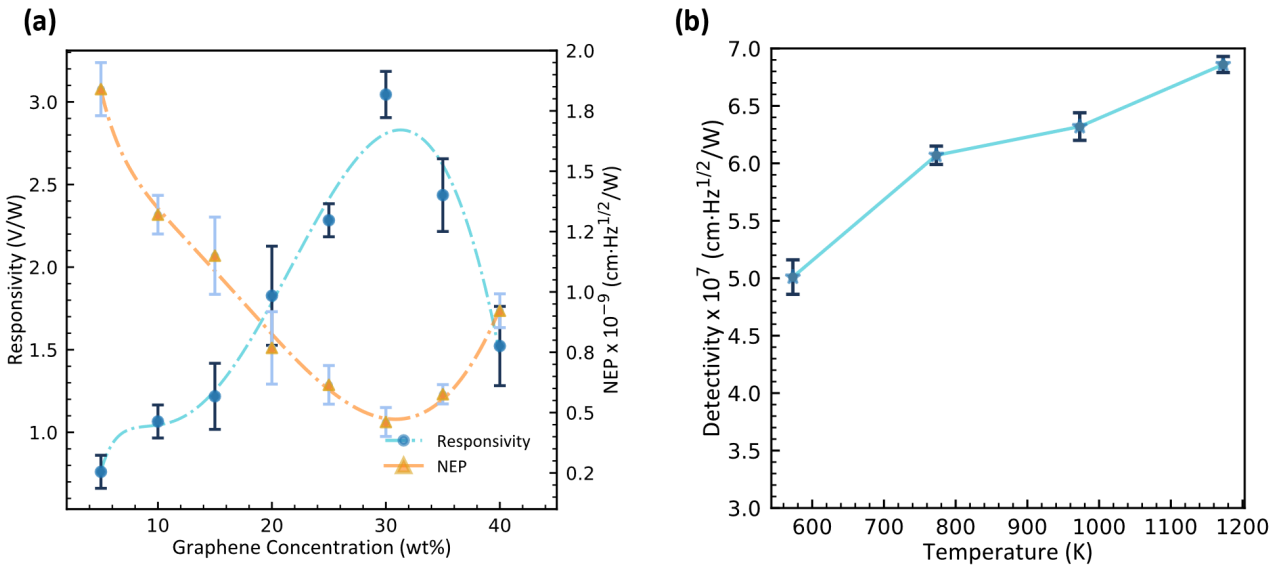

Figure 3-11. (a) Doped-PANI/graphene Photodetector responsivity and noise equivalent power (NEP) via increasing graphene concentrations. The testing content concentrations start 5 wt%, 10 wt%, 15 wt%, 20 wt%, 25 wt%, 30 wt%, 35 wt%, and 40 wt%. **(b)** The detectivity of 30 wt% graphene detectors under various blackbody temperature radiation temperatures, setting at 573K, 773K, 973K, and 1173K.

The first merit of photoresponse is photoresponsivity R_v, which is quantified the detector sensitivity from the photoinduced power P_{in}. The responsivity of doped-PANI/graphene detectors has been investigated by tuning the graphene concentration in mixture solutions. The photoresponsivity in the PTE mechanism can be written as $R_v = \mathrm{V}_p/P_{in}$, where V_p is corresponding to the photoinduced voltage [123]. Due to the stable photo resistances, the prominent noise in such detector belongs to the fluctuation of carriers' thermodynamic motion, in other words, John-Nyquist noise. Therefore, NEP can be evaluated as follows: $V_N = \sqrt{4k_BTR}$, where the k_B is the Boltzmann constant, T is the temperature, and R refers to the device resistance [124]. Increasing the loading of graphene concentration from 5 wt% to 30 wt%, the overall

photoresponse rises from 1.0 V W^{-1} to 2.5 V W^{-1} (**Figure 3-11(a)**). The NEP decreases to its lowest position with a 10^{-10} range under the same measuring condition. This phenomenon is considered when the graphene loading increases, stronger photon energy absorbs, forming a higher temperature gradient in the mixture channel and forcing thermal equilibrium to move to its balance style. Furthermore, the tunable graphene components improve the thermoelectric conversion efficiency using a dimensionless index judgment $ZT = \frac{\sigma S^2 T}{k}$, where σ represents the electrical conductivity, S is defined as the Seebeck coefficient, T stands for the temperature, and k is the thermal conductivity [32]. A higher ZT value may achieve due to the involvement of PANI, improving the electrical conductivity and Seebeck coefficient (21.8 μV K^{-1} in **Figure 3-12**), leading temperature balance quickly to reach the whole channel [124, 125]. Whereas the graphene concentration increases above 30 wt%, the responsivity increasingly drops to 1.5 V W^{-1}. This finding of drops may rely on increasing thermal conductivity at upraised graphene concentration while dwindling the Seebeck coefficient owing to the disorganized distribution of graphene dispersion and the increasing defects structures [116].

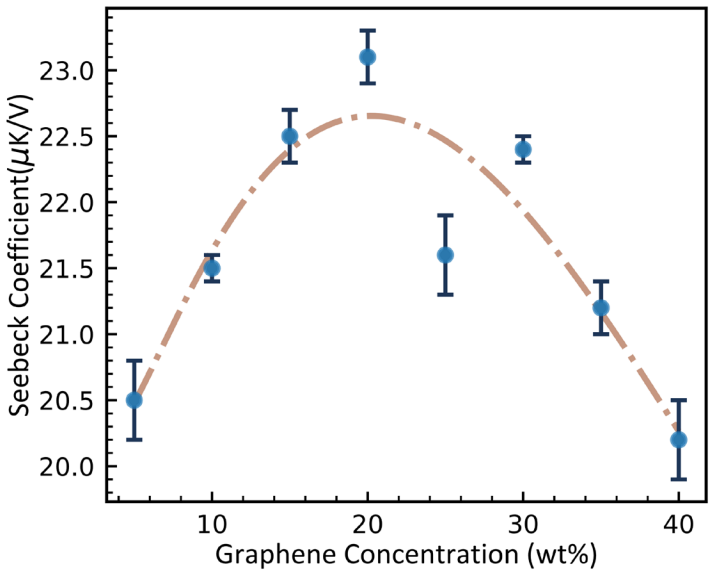

Figure 3-12. Seebeck coefficients under various graphene concentrations. The average Seebeck coefficient of our doped PANI/graphene composite is 21.8 μV K^{-1}.

Apart from the concentration of the graphene content, another principal impact factor is the radiation temperature. The radiation temperature reflects the source power from blackbody radiation. While the temperature rises from 573K to 1173K, the receiving energy of PTE detectors increases from 1.7 mW/(sr·mm^2) to 26.8 mW/(sr·mm^2) (**Figure 3-13**). To judge the photodetector performance, the detectivity $D^* = \frac{R_v\sqrt{A_d}}{V_N}$ is selected to differentiate the photon signals from the measuring noise, where A_d is the effective photoactive area [26]. **Figure 3-11(b)** describes the doped-PANI/Graphene materials' detectivity at temperatures from 575K to 1173K. The detectivity raises from 5.0 cm $Hz^{1/2}$ W^{-1} to a 30% increase. Compared to our previous PEDOT: PSS/graphene, the doped-PANI/graphene improves five times, and several reasons may contribute to this high achievement: First, the doped-PANI/graphene disperses much better with ultrasonic and tip dispersion, and composite materials receive optimized concentration. Second, the metal electrodes are well selected to form a diverse Seebeck gradient for higher thermoelectric conversion efficiency. Third, decreasing and optimized electrode height leads to faster light absorption and less reflection.

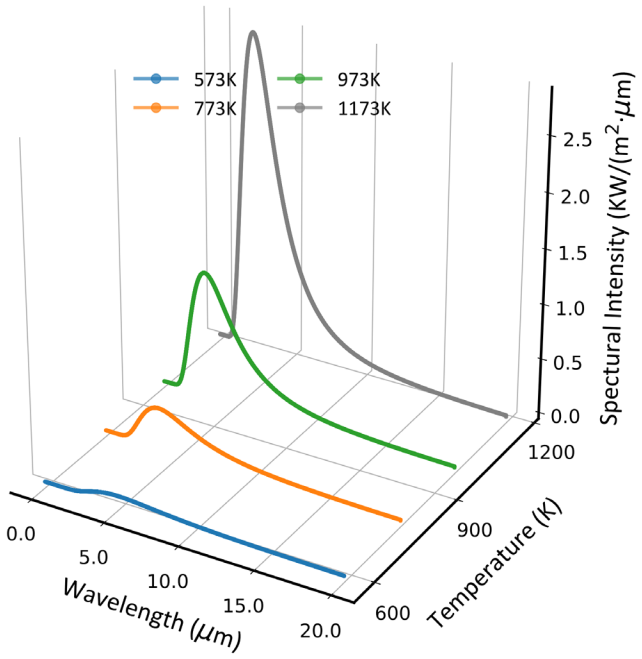

Figure 3-13. Blackbody spectral radiation curves under a temperature of 573 K, 773 K, 973 K, and 1173 K. The wavelength of the peak ranges from 5.1 μm, 3.7 μm, 3.0 μm, and 2.4 μm, respectively.

Table 3-1 compares current representative PTE detectors, and **Table 3-2** makes comparisons of polymer (composite) based photodetectors. Based on the tables' results, we indicate that our doped PANI/graphene detectors obtain a high detectivity, responsibility, wide range, flexibility, and no-bias voltage support.

Table 3-1 Comparison of representative PTE detectors.

Photoactive layer	Mechanism	Responsive Range	Responsivity	Detectivity	Bias Voltage	Flexibility	Ref

Graphene/doped-PANI	PTE	MWIR to LWIR	2.5 V W^{-1}	6.8×10^7 cm $Hz^{1/2}$ W^{-1}	N/A	√	This work
Graphene/p-n junction	Plasmonic + PTE	Visible	0.25 mA W^{-1}	N/A	-2 V/9 V	×	[125]
Black Phosphorus	PTE	THz	297 V W^{-1}	N/A	0-0.2 V	×	[126]
CNT fiber/p^+-p^- junctions	PTE	LWIR to UV	0.32 V W^{-1}	4.3×10^7 cm $Hz^{1/2}$ W^{-1}	N/A	√	[127]
Mxene/MWCNTs	PV+PTE	Visible	1.8 mV	N/A	N/A	×	[128]
$SrTiO_3$	PTE	MWIR to UV	1.2 V W^{-1}	N/A	N/A	×	[129]
$EuBiSe_3$	PTE	THz to UV	1.69 V W^{-1}	N/A	N/A	×	[130]
RGO	PTE	THz to UV	0.7-28.2 mV W^{-1}	0.16-6.67×10^6 cm $Hz^{1/2}$ W^{-1}	N/A	×	[131]
CNT/PVA	PTE	MWIR to LWIR	0.1 V W^{-1}	4.9×10^6 cm $Hz^{1/2}$ W^{-1}	N/A	√	[132]
Graphene/PEDOT: PSS	PTE	MWIR to LWIR	0.27 V W^{-1}	1.4×10^7 cm $Hz^{1/2}$ W^{-1}	N/A	√	[34]

Table 3-2 Comparison of carbon-based photodetectors.

Photoactive layer	**Mechanism**	**Responsive Range**	**Responsivity**	**Detectivity**	**Bias Voltage**	**Flexibility**	**Ref**
Graphene@doped-PANI	PTE	LWIR to MWIR	2.5 V W^{-1}	6.8×10^7 cm $Hz^{1/2}$ W^{-1}	N/A	√	This work
CNT@PVA	PTE	LWIR to MWIR	0.1 V W^{-1}	4.9×10^6 cm $Hz^{1/2}$ W^{-1}	N/A	√	[132]
Graphene@PEDOT: PSS	PTE	LWIR to MWIR	0.27 V W^{-1}	1.4×10^7 cm $Hz^{1/2}$ W^{-1}	N/A	√	[34]
CND@PVA	PV	Visible to UV	267.1 mA W^{-1}	N/A	5 V	X	[133]
PCDTPTSe@PC71BM	PV	NIR	100 mA W^{-1}	6×109 cm $Hz^{1/2}$ W^{-1}	N/A	X	[134]

3.4 Detector flexibility and long-term stability

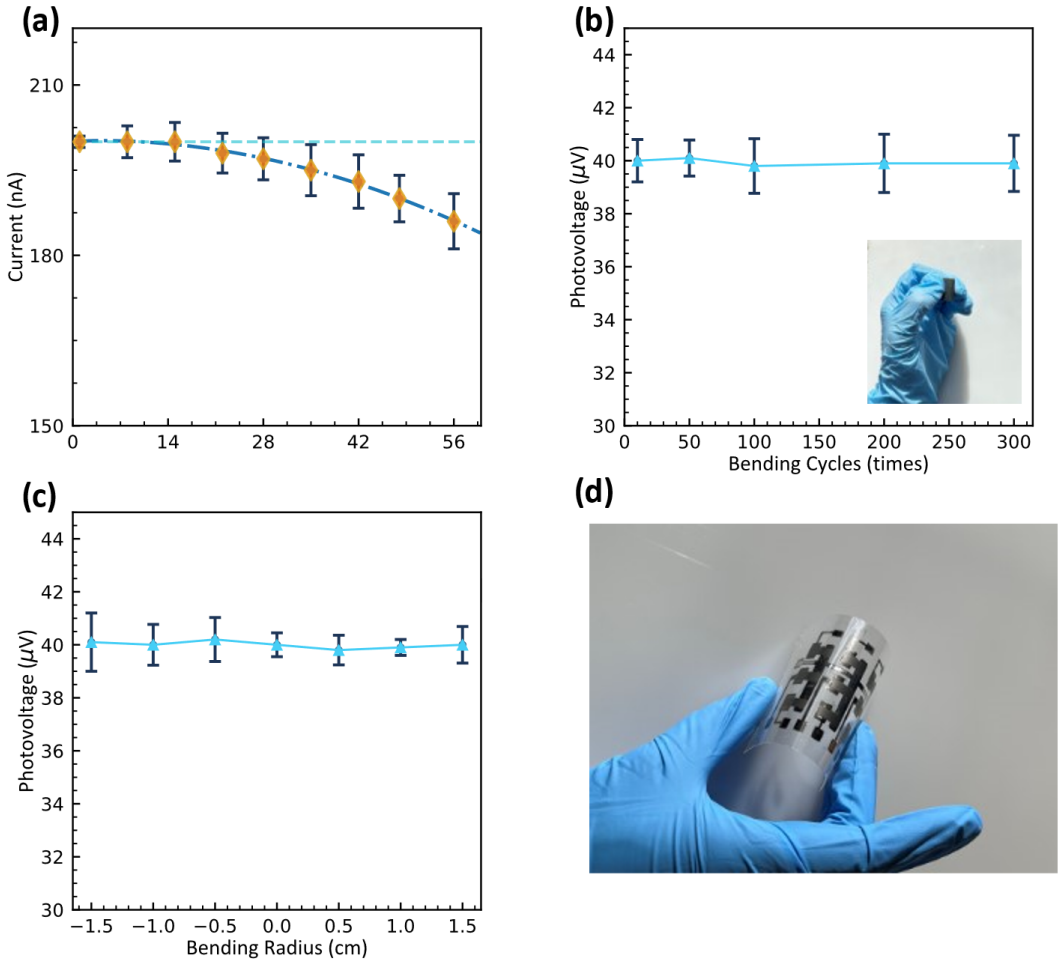

Figure 3-14. (a) Doped-PANI/graphene photodetector stability in an ambient environment after 56 days. **(b)** Stable Photovoltage under multiple bending cycles. **(c)** Photoresponse under various bending radii from -1.5cm to 1.5cm **(d)** Strong flexibility of a 3x3 pixel detector.

As for non-contact PTE detectors, one requirement should be long-time stability and endurable under numerical deformations. Despite the oxygen and air humidity, long-term stability is critical to proving applications in wearable electrons. Our doped-PANI/graphene detector obtains both

excellent stability and flexibility. **Figure 3-14(a)** shows the stable photoresponse of our detector under an ambient environment. The long-term stability demonstrates the photocurrent only shrinks less than 5% degeneration after 56 days without any shape deformation. Such a low-cost, stable response in a doped-PANI/graphene detector allows for realistic utilization. Another crucial investigation is the flexibility of the detector under various bending recycles and external forces. **Figures 3-14(b) and 3-14(c)** illustrate the doped-PANI/graphene photoresponse on PET substrate under multiple foldings. With multiple radii (-1.5 to 1.5 cm) folding and more than 300 bending numbers, the doped-PANI/graphene detector can endure external forces while maintaining its stable performance. Owing to the relatively robust van der Waals interaction between synthesis materials and PET substrate and the flexibility of mixed composite, the potential of such a high-performance detector may be applied to abundant applications **(Figure 3-14(d)**).

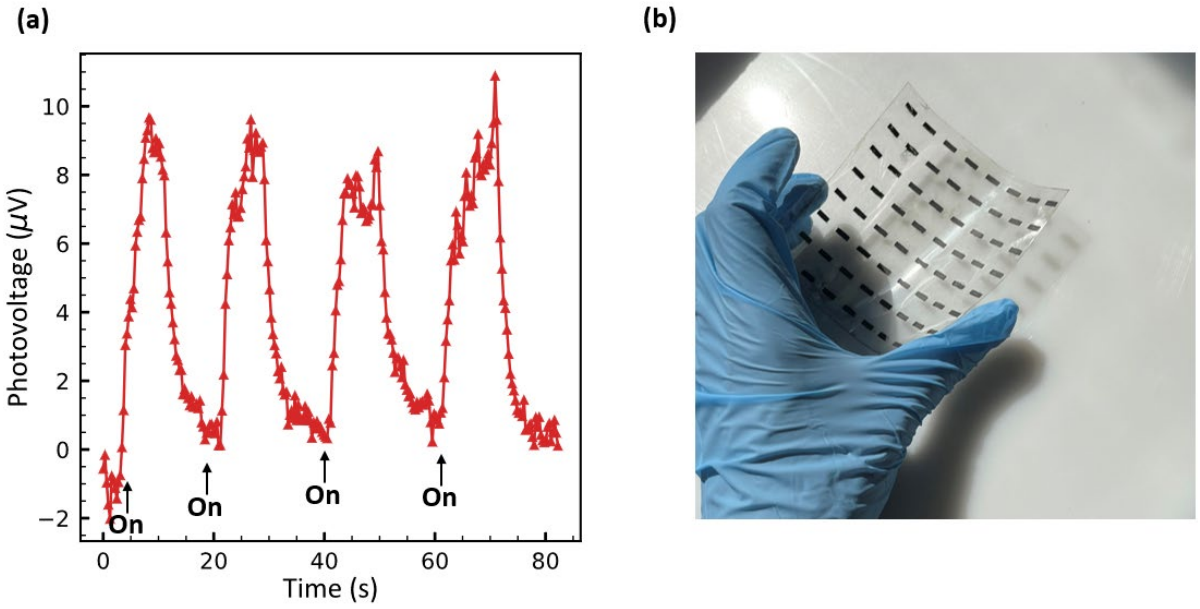

Figure 3-15. (a) Fingertip photovoltage response under multiple stimulations. Each cycle sets fingertips 3-5mm away from the photodetector and moves perpendicularly. **(b)** A flexible 8x8 pixel detector array on PET substrate for various applications.

3.5 Human health responsivity

The coronavirus disease 2019 (COVID-19) pandemic has been expressed as a significant issue of public health defense. The reproductive virus can remain suspended in the air for a long time by droplets and aerosol transmission, leading to a person-to-person infection possibility, especially in poorly ventilated closed spaces [135]. To reduce the likelihood of interacting with human infection, non-contact, self-powered, low-cost, and easy fabrication detectors of human interactions are essential. A specific human-body passive radiation PTE detector aims at such desire using the doped-PANI/graphene as a composite with a flexible PET substrate. Human radiation is compatible with blackbody radiation, mainly from the wavelength from the MWIR to the LWIR region. We further investigate spontaneous human radiation photoresponse using the above sensitive detector. Fingers are set around 3-5 mm away from the detector and then moved up and down along the perpendicular direction towards the detectors multiple times to simulate human interactions. **Figure 3-15(a)** presents a rapid photovoltage response under multiple stimulations in various changes, with the peak voltage lying around 10 μV in each cycle. Furthermore, **Figure 3-15(b)** shows possible applications of an 8x8 pixel detector array with specific channels. An individual pixel represents a photodetector to monitor photoresponse. Such detectors will emerge as complex recognition in human gesture interactions, industrial non-destructive examinations, and other potential application scenarios.

3.6 Conclusion

This chapter proposes a high-performance, bias-free PTE detector using a doped PANI/graphene composite. The photo-response is improved by utilizing vital π-π junctions in the doped PANI/graphene composite and tuning the proportion of graphene, eventually reaching a peak detectivity of 6.8×10^{7} cm $Hz^{1/2}$ W^{-1} and responsivity of 2.5 V W^{-1}. The doped PANI/graphene

photodetector can also maintain stability in a room-temperature environment. After 56 days, the performance degrades less than 5%, and simultaneously, the flexibility on the PET substrate can endure various bending radii and multiple cycles. Furthermore, sensitive finger response reveals its anticipation as wearable health monitors. Our study reckons this doped PANI/graphene composite may pave the way toward broadband PTE detector applications in non-destructive industrial monitors, bio-compatible medical wearable electrons, and explicit aerospace detection.

Chapter 4 Flexible Multi-element Photothermoelectric Detectors Based on Spray-coated Graphene/Polyethylenimine Composite for Non-destructive Testing

4.1 Aims and highlights

In this chapter, we proposed a vertical graphene/polyethylenimine (PEI) composite multi-element detector combined with the spray-coating method on polydimethylsiloxane (PDMS), poly (ethylene terephthalate) (PET), and glass substrate. PEI as the polymer matrix improves the composite's flexibility, lowers the thermal conductivity, and enhances compacity with substrate surface as high amine functional groups [136]. Optimizations of PTE performance on PET substrate are obtained through the 800 mg ml^{-1} PEI adjustment, graphene loadings in 10 wt%, and other technical factors, attaining a peak of 6.05×10^7 cm $Hz^{1/2}$ W^{-1} photo detectivity and 2.7 V W^{-1} responsivity at 973 K blackbody radiation temperature. Compared with recent polymer-based and graphene-based PTE photodetectors (Table S1 and Table S2), our work has the superiority of relatively high responsivity, detectivity, and broad responsive range. In addition, no bias voltage is applied to manipulate the performance. We also investigate the flexibility and long-term stability of our detectors. Finally, the non-destructive testing (NDT) system vividly characterizes the samples' complete image and may contribute to future industrial monitoring.

4.2 Result and discussion

4.2.1 Design flexible multi-element graphene/PEI composite

The flexible graphene/PEI composite multi-elements were schematically illustrated in **Figure 4-1** (a)-(b). First, we combine ultrasonic sonification and magnetic stirring to obtain the uniform

graphene/PEI solution. The branched polyethylenimine (PEI, average Mw 25000, purchase from Aldrich-Chemistry), starting from 100 mg ml-1 to 1500 mg ml-1, with an increment of 100 mg ml-1, was dissolved in Dimethyl sulfoxide (DMSO, ACS reagent, purity ⩾97%, purchased from Sigma-Aldrich), in assistance of magnetic stirring of 1000 rpm for 24 hours under 30 °C until clear, homogeneous solution was obtained. Then, the solution was transferred to another vial, adding graphene power (purity over 97.0 %, 3-5 layers, obtained from Nanochemazone) with various weight portions (2.5 wt% to 15 wt%, in augmentation of 2.5 wt%), operated via ultra-sonication for 20 mins, and followed by another round of magnetic stirring at 1200 rpm for 12 hours under the room temperature, avoiding flakes aggregation and recombination.

With sonification and magnetic stirring, the graphene power can be delaminated and compatibility combined with the PEI polymer matrix. The PDMS substrate is fabricated using silicon elastomer (Sylgard 184, Dow Corning Corporation), base, and curing agent at a ratio of 10:1. The mixture was degassed, poured onto a clean stainless mode, and cured at 65 °C for 1 h. PET substrate and glass substrate were treated with isopropyl alcohol and plasma.

After cleaning the surface of the PDMS, PET, and glass substrate, any organic residual is left out to avoid graphene reaggregations. Then, the substrates are coated with a layer of titanium as the bottom electrodes, which can assist the adhesion of graphene/PEI composite and avoid peeling off from the surface. The bottom layer of the substrates was deposited by 1000 um Ti with the same H-shape shadow mask via an e-beam evaporator (ANGSTROM-Ebeam) with a 3.0 Å s^{-1} deposition rate.

Next, the deposition of the abovementioned homogeneous solution is transferred to a spray-coating system. The spray (TC-20Bseris, Spedertool) was set at 1 bar pressure regulating, and the outlet

diameter of the spray was selected at 0.2 mm. The screw adjusted the spray-coating rate at 1 mL min-1, and the distance between the nozzle tip and the substrate surface was 10 cm. Then, all dispersed substrates were transferred to the oven under drying at 90 °C for 6 hours and cooling to 50°C for 4 hours. The solution was atomized into tiny droplets by toggling the valve to reduce the Van der Waals force between the droplets and the surface. The spray coating is performed twice for uniform spraying in the same zig-zag direction from top to bottom. Specific 4×4 laser-involved shadow masks are patterned for each type of substrate and drive the liquid to standard 16 uniform H-shape cells. Then, all dispersed substrates are baked inside the oven with nitrogen gas protection under drying to evaporate the solvent and cool down to reduce the effect of droplet surface tension.

Finally, dried-out devices were carried out for the third round of aluminum deposition by the same e-beam evaporator at 1.5 Å s^{-1} with the help of the laser-induced mask. Next, the graphene/PEI detectors are bonded through silver conductive epoxy (MG Chemicals 8331D Silver Conductive Epoxy Adhesive) for Ti/Al outlined electrodes, allowing the epoxy to dry out at least 12 hours at room temperature. The shadow mask technique controls all procedures, thus avoiding any complicated photolithography method to pollute the graphene/PEI materials.

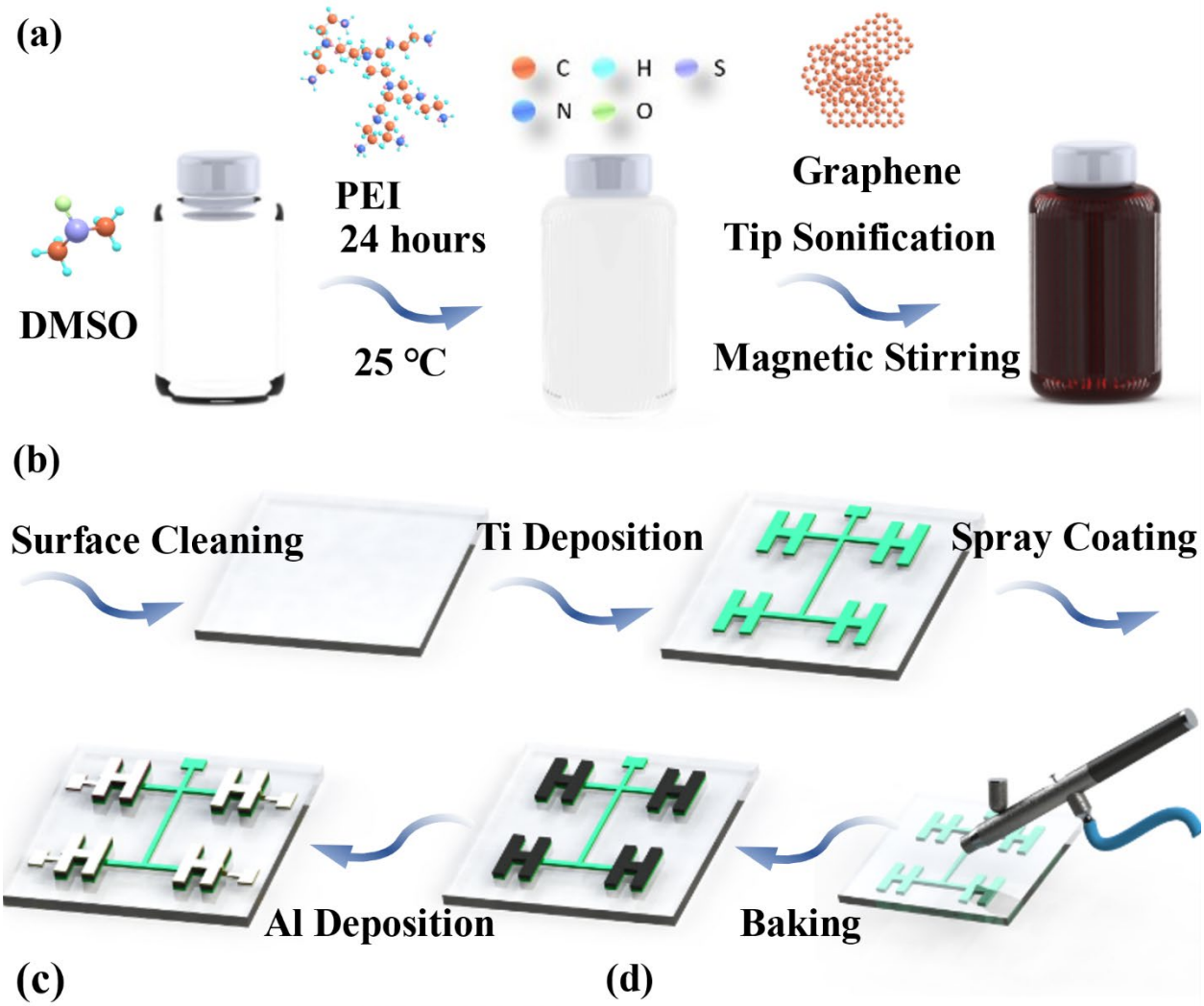
(a)
C
H
S
N
O
DMSO
PEI
24 hours
25 °C
Graphene
Tip Sonification
Magnetic Stirring
(b)
Surface Cleaning
Ti Deposition
Spray Coating
Al Deposition
Baking
(c)
(d)
PEI
DMSO
1μm

Figure 4-1. Spray-coated flexible graphene/PEI composite multi elements. **(a)** Schematic of the fabrication process of the graphene/PEI solution. **(b)** Spray-coating method applied to the graphene/PEI multi-elements. **(c)** A photograph of 16 H-shape cells of graphene/PEI detectors. **(d)** The SEM image of graphene/PEI solution under the 1 μm scale.

4.3 Characterization of flexible multi-element graphene/PEI composite

4.3.1 SEM and optical image

To investigate the morphology characterization of the graphene/PEI material, a 5.0 kV voltage and 8-10 nA beam current were set using the scanning electron microscope (JEOL JSM-7200F). In optical observation, the SEM image (**Figure 4-1 (**d) and **Figure 4-2**(a)) of the graphene/PEI material layer and the gradient of electrode and material (**Figure 4-2**(b)) shows the uniform dispersion and orderly spray coated at the intersection layer. The top metal-sample image was collected by a microscope (OLYMPUS-scope).

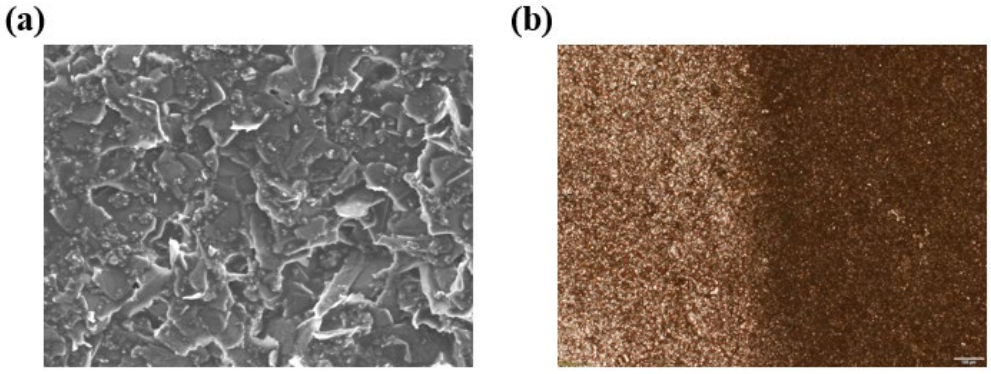

Figure 4-2. (a) The SEM image of the graphene/PEI detector under the bar of 1 μm scale, 5 kV voltage, and 8 nA current. **(b)** The optical image of the graphene/PEI detector at the cross-section of the aluminum and photoactive layer. The scale bar is 500 μm.

4.3.2 Raman image

Next, the Raman Spectrum curve of the sample was obtained by Bruker Senterra-2 Raman with a 785 nm laser source, 1 mW source, and 50 s integration time. The Raman figures (**Figure 4-3**) of a sample prove the 10 wt% graphene homogeneously mixed in 800 mg ml^{-1} PEI matrix solution, leading to an extended structure for electrode movement and strong π- π interactions [137, 138].

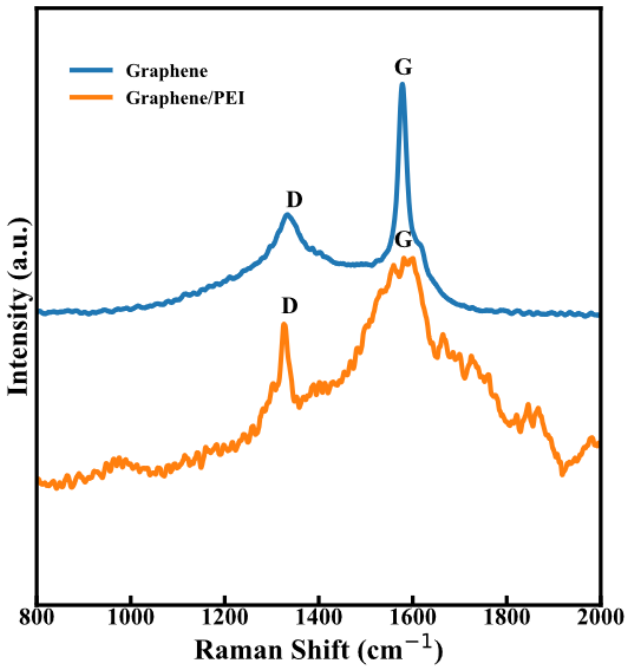

Figure 4-3. The Raman spectrum of pure graphene and the graphene/PEI at 10 wt% graphene loading detector.

A typical D band (1350 cm^{-1}) and G band (1580 cm^{-1}) can be viewed in a pure graphene spectrum. These bands can be interpreted as defects in materials and the primary vibration of the sp^2-

hybridized carbon zone [139]. After the involvement of PEI, the D band increased while the G band decreased. Besides, the peak of the D band and G band slightly shift to a smaller band number. This scenario may consider strong sp^2 interactions [140].

4.3.3 FTIR image

The FTIR image in transmittance mode was obtained by Bruker Tensor 27 FTIR, scanning from 400 to 4000 cm^{-1} wavenumbers. **Figure 4-4** in transmittance mode reveals the compatibility of the graphene/PEI composite.

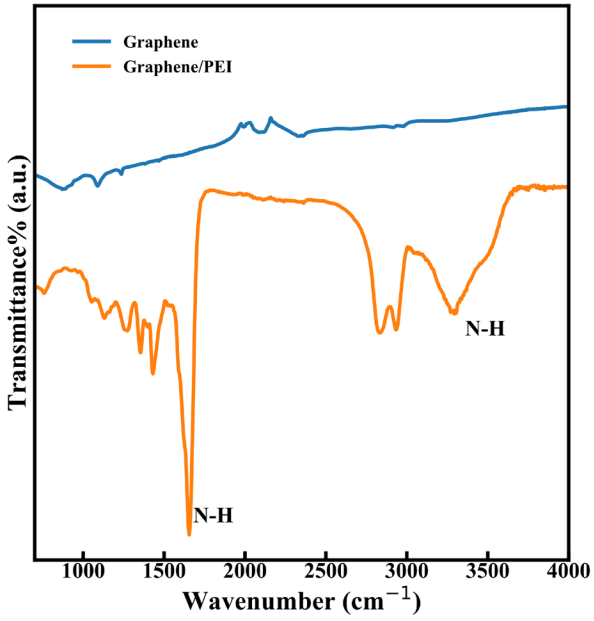

Figure 4-4. The FTIR image of the graphene, graphene/PEI composite curves.

According to the FTIR result, unlike graphene oxide (GO) and reduced graphene oxide (RGO) showing peaks at unique around 3430 cm^{-1} (O-H bond), 1730 cm^{-1} (C=O bond) and 1056 cm^{-1} (C-O bond), graphene does not show such heavy absorption peaks [141–143]. Instead, while combining with PEI, the N-H peaks show at 1654 and 3305 cm^{-1}, demonstrating PEI is successfully compatible with graphene [144].

4.3.4 Seebeck coefficient

A homemade thermal couple (**Figure 4-5**) containing alumel and chrome is made to detect the Seebeck coefficient of the graphene/PEI material with various temperature differences (**Figure 4-6(b)**). Our measurement demonstrates the n-type material with a high average value of -31.5 μV K^{-1}, assisting the overall performance of PTE conversion (**Figure 4-6(a)**).

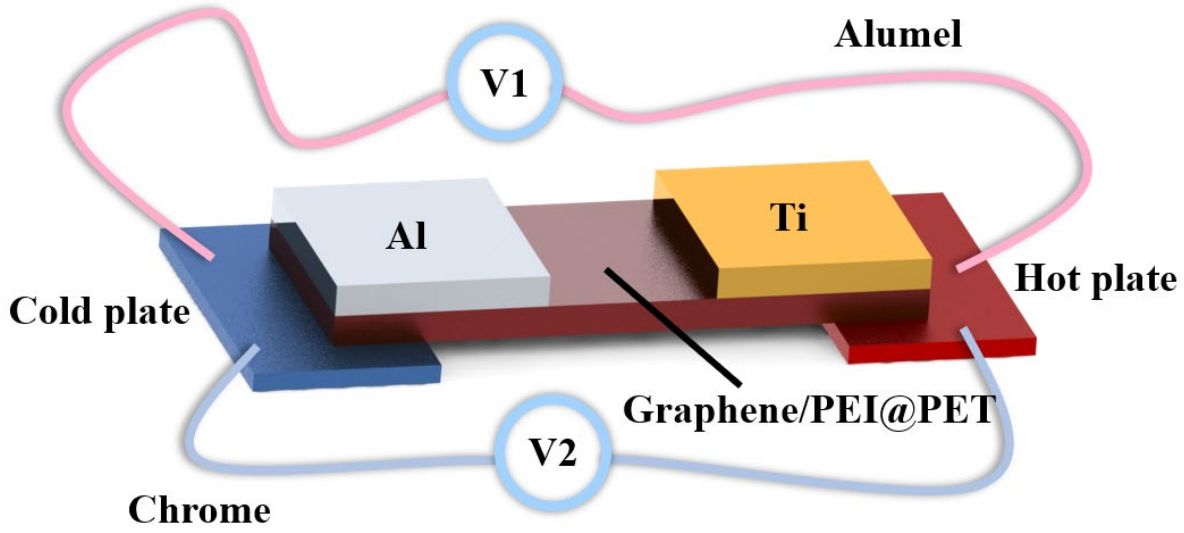

Figure 4-5. A homemade Seebeck coefficient measurement platform.

The Seebeck coefficient of the composite was investigated from a homemade system containing a thermal couple made with alumel (-18 μV K^{-1}) and chrome (22 μV K^{-1}) and temperature adjustment. The device was placed onto one side of a hot plate and the other onto a cold plate. The temperature difference can be calculated by manipulating the temperature differences on the hot side while the cooling plate was stable at 0°C, and voltage changes can be read out. Besides, the relationship between the Seebeck coefficient and graphene loadings was tested using the same system [21].

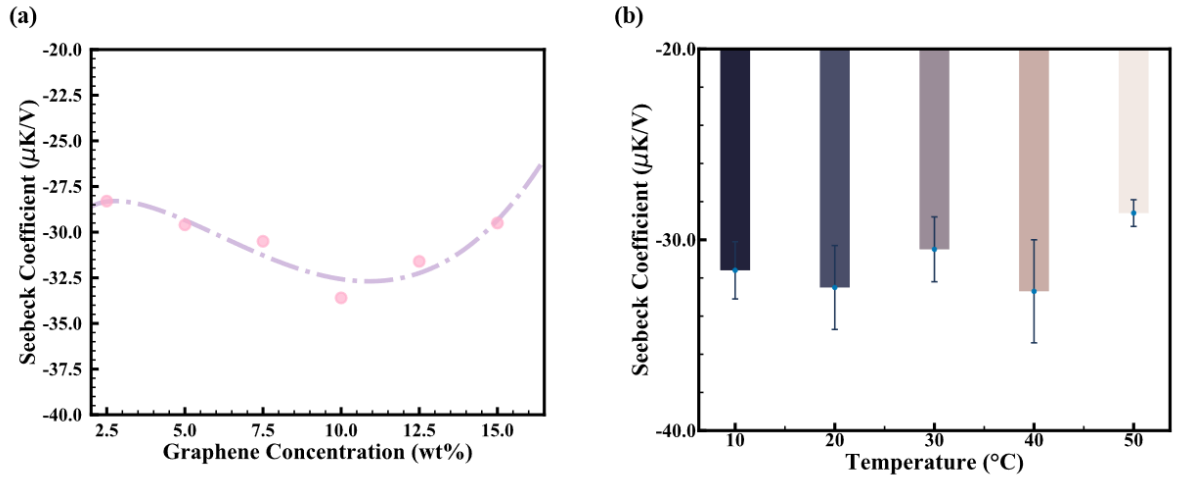

Figure 4-6. Seebeck coefficient of the graphene/PEI material. **(a)** The Seebeck coefficient of the material under the various graphene concentration starts from 2.5 wt% to 15.0 wt%. The PEI concentration is stable at 800 mg ml $^{-1}$. **(b)** The Seebeck coefficient under various temperature differences. The average of the Seebeck coefficient is -31.5 μV K^{-1}.

4.3.5 Thermal image

The standard IR thermal image to reflect the thermal conduction was photographed by a thermal imaging camera (Hti-Xintai thermal imaging camera HT-19) (**Figure 4-7**). The peak temperature is 45.3 °C, and the room temperature is 23.7 °C. The highest temperature in the IR image indicates our materials are not moderately affected under high blackbody radiation temperatures.

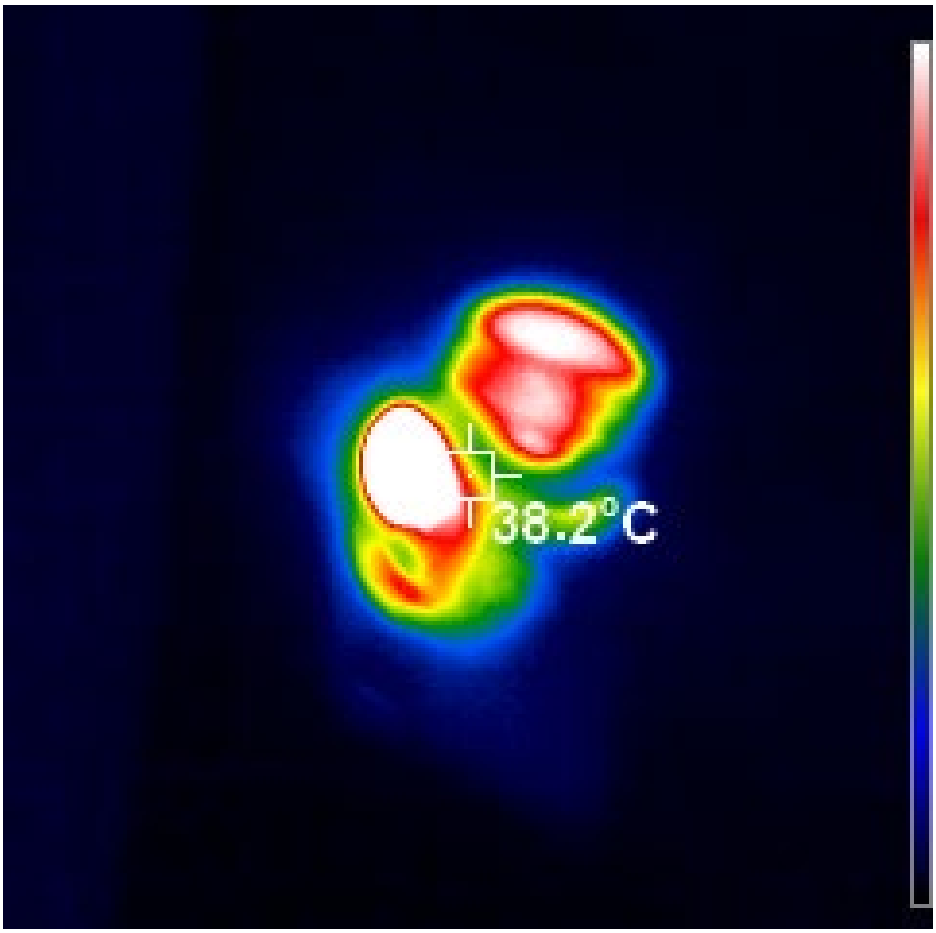

Figure 4-7. The temperature of the material under the 973 K blackbody radiation.

4.3.6 Height measurement

The height of the samples with different methods was obtained through a surface profilometer (BRUKER-profilometer) with standard scan procedures.

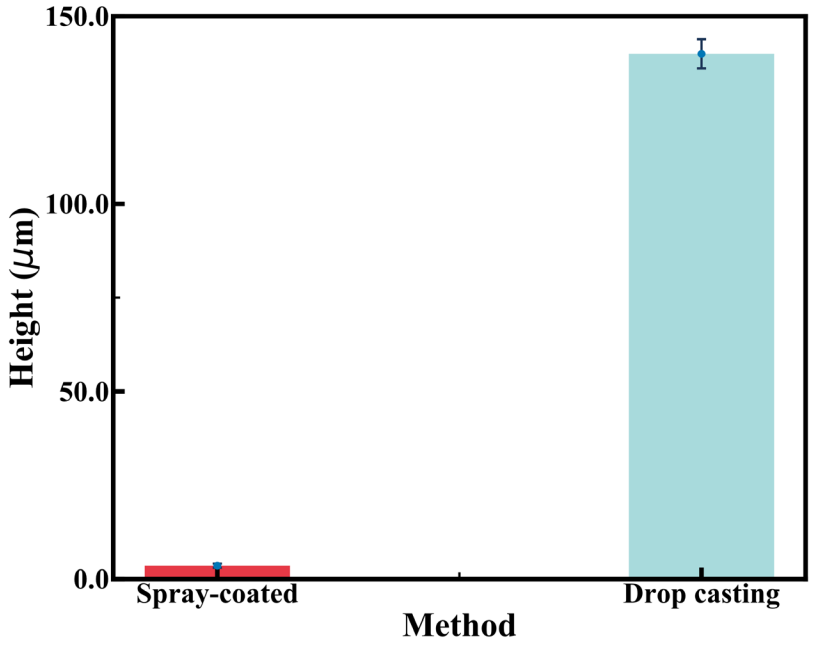

Figure 4-8. Comparison of the spray-coated and drop-casted membrane of graphene/PEI material under the same photo resistance.

4.4 PTE response measurement

PTE response can be explained as a signal generated by the carrier diffusion along the temperature gradient induced by the radiation illumination. More specifically, the PTE mechanism can be viewed as two steps: the photothermal stage and the thermoelectric stage. **Figure 4-9(a)** depicts that when the incident radiation waves are illuminated on the top of the thin film of 20-25 nm aluminum, most waves infiltrate inside the top electrode [123]. While the middle layer of graphene/PEI continuously traps the radiation energy, most of the illumination energy is eventually absorbed inside the aluminum (Al) and graphene/PEI region. The titanium (Ti) electrode and the substrates act as the heat sink, and the top thermalized aluminum electrode represents the hot source. Therefore, the nanostructure will induce the temperature gradient through the vertical direction as described by

$$V = \int_{bottom}^{top} S(h)\nabla T dh = \int_{GP-S}^{Al} S\,(h)\nabla T(h)dh + \int_{Ti}^{GP-S} S\,(h)\nabla T(h)dh \qquad (4\text{-}1)$$

, where S refers to the Seebeck coefficient, and T stands for the temperature[145]. Overall, the efficient conversion from photon energy into thermal and electric energy without bias suggests the self-powered energy harvest and other wearable IoTs.

Figure 4-9(c) illustrates the current-voltage (I-V) curves of graphene/PEI detectors on PDMS, PET, and glass substrates under radiation of 973K illumination within the -80 μV to 80 μV range. To measure the current-voltage characteristics of the graphene/PEI detector, a Keithley 6500 multimeter (current measurement, TEKTRONIX, INC) and Keithley 6487 (voltages providing, TEKTRONIX, INC) are applied. The data was recorded by applying -1 mV to 1 mV voltage without any voltage/current amplifier combination. The radiation off measurement was set under the cover of a black box to reduce any outside environment light illustration. A blackbody source (Newport Oriel 67030), adjusted from 573 K to 1173 K, incrementing 200 K as a step temperature, was applied to stimulate the low-intensity radiation environment. Besides, a germanium cut-off IR lens, which cut off the wavelength below 1.5 um, was inserted to reduce the heating factors and block other wavelength radiations, only allowing infrared radiation for PTE absorption. Besides, the graphene and PEI composite on the PDMS substrate exhibits a higher photocurrent response. The reason behind the scenario may rely on the thermal conductivity variations in different substrates. Our samples' PDMS, PET, and glass substrate values are 0.27,0.30, and 1.04 W m^{-1} $K^{-1,}$ respectively. Higher thermal conductivity means faster heat dissipation generated by the transfer of the absorbed photon energy. Therefore, the thermoelectric and the overall PTE efficiency are lower than a substrate with lower thermal conductivity. Even increasing the voltage range from -1 mV to 1 mV (**Figure 4-10**), the linearity of the I-V curve at zero external bias validates the ohmic contact of various layers, achieving 500-700 Ω resistance.

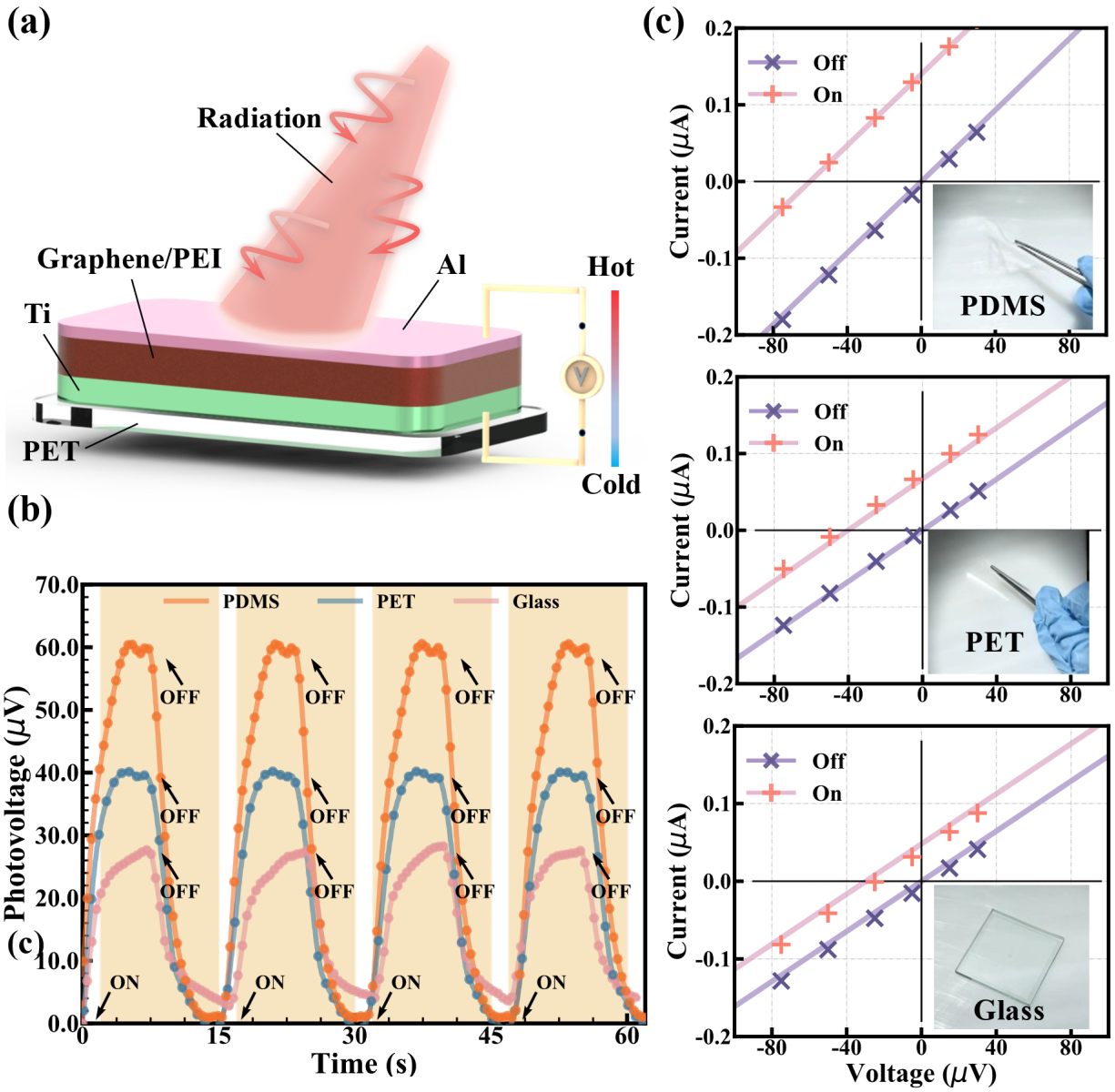

Figure 4-9. PTE response measurement. **(a)** PTE mechanism and structure of graphene/PEI composite **(b)** Cycling photoresponse time of 10 wt% graphene loading under 973K radiation with PDMS, PET, and glass substrates. **(c)** I-V curves of graphene/PEI detectors with on/off illumination with glass, PET, and PDMS substrates in the -80 μV to 80 μV range.

Furthermore, repeatable and stable transition cycles can be attained through **Figure 4-9(b)**, where the rapid PTE response in 5-7s demonstrates the photon stimulation and thermal conduction among specific electrode selections, precisely controlling electrode height and the homogenous synthesis materials. Additionally, slight variations in response time for each PDMS, PET, and glass substrate may indicate the different heat dissipation through the bottom substrate with the substrates [146].

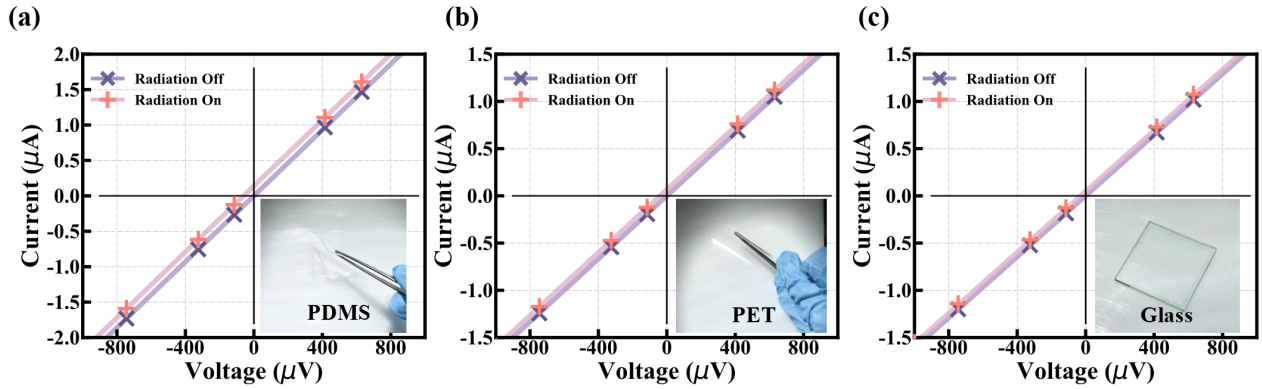

Figure 4-10. The current-voltage (I-V) curves of graphene/PEI detectors on various substrates under the illumination of radiation of 973K within the -1 mV to 1 mV range. A linear relationship can also be viewed to confirm. **(a)** The PDMS substrate. **(b)** The PET substrate. **(c)** The glass substrate.

To verify the capacity of graphene/PEI detectors to absorb the lowest photon energy from the noise disturbance, the detectivity D^* is written as $D^* = \frac{V_{in}\sqrt{A}}{P_{ab}NEP}$ [147], where V_{in} implies the photovoltage, P_{ab} is the incident photon energy, A stands for the effective photoactive area, and NEP refers to the noise equivalent power (NEP). No heat dissipation is considered at any evaluated values. Owing to the no-bias voltage applied in the detectors, the dominant noise, called Johnson-

Nyquist noise, can be calculated as $NEP = \sqrt{4k_BTR}$ [148], where k_B refers to the Boltzmann constant, and R is the stable device resistance. Besides, the first friction of the detectivity D^* can be concluded as responsivity $R_V = \frac{V_{in}}{P_{ab}}$ [149]. While the source temperature increases from 573 K to 1173 K, the power intensity switches from 2.7 to 35 mW $(sr \cdot mm^2)^{-1}$. The photocurrent raises from 31.7 nA to 91.6 nA as the PET substrate (**Figure 4-11(a)**). This enhanced photoresponse may rely on high infrared photon energy absorption. The correlation of detectivity exhibits in **Figure 4-11(b)**. The detectivity is consistently located above 10^7 cm $Hz^{1/2}$ $W^{-1,}$ and the peak value is 6.05 x 10^7 cm $Hz^{1/2}$ W^{-1}. This enhancement indicates an improved photoresponse appearing in the lower input power. We reckon this situation with two possible reasons. First, the responsivity R_V decreases as the shifting of the radiation pattern (see **Figure 4-12**), the selective absorption broadband, and the IR filter's cut-off effect. With the blackbody temperature rising, the peak of the blackbody spectrum moves from 5.06 μm to 2.47 μm, leaving less area of the IR regime by the cut-off IR filter. Besides, the photon energy absorption of the graphene/PEI is not consistently equivalent at each wavelength [79]. Thus, the total photo responsivity integration is insufficient at higher power intensity. Second, as a zero-bias detector, the NEP power increases as the source temperature improves from 573 K to 1173 K with constant resistance. This drop flection of the responsivity and the raising pattern of NEP matches well with **Figure 4-11(b)** and **(d)**. Overall, the total of the detectivity drops depends on the reduced photoresponsivity and the increasing NEP power. This feature may benefit practical applications as the real-world infrared radiation is much weaker than the laser output. Besides, the peak of human radiation usually locates at 9.3 μm [150], which is much closer to the lower blackbody radiation power input, facilitating applications such as wearable electronics for energy harvesters and human health monitors possible in the future.

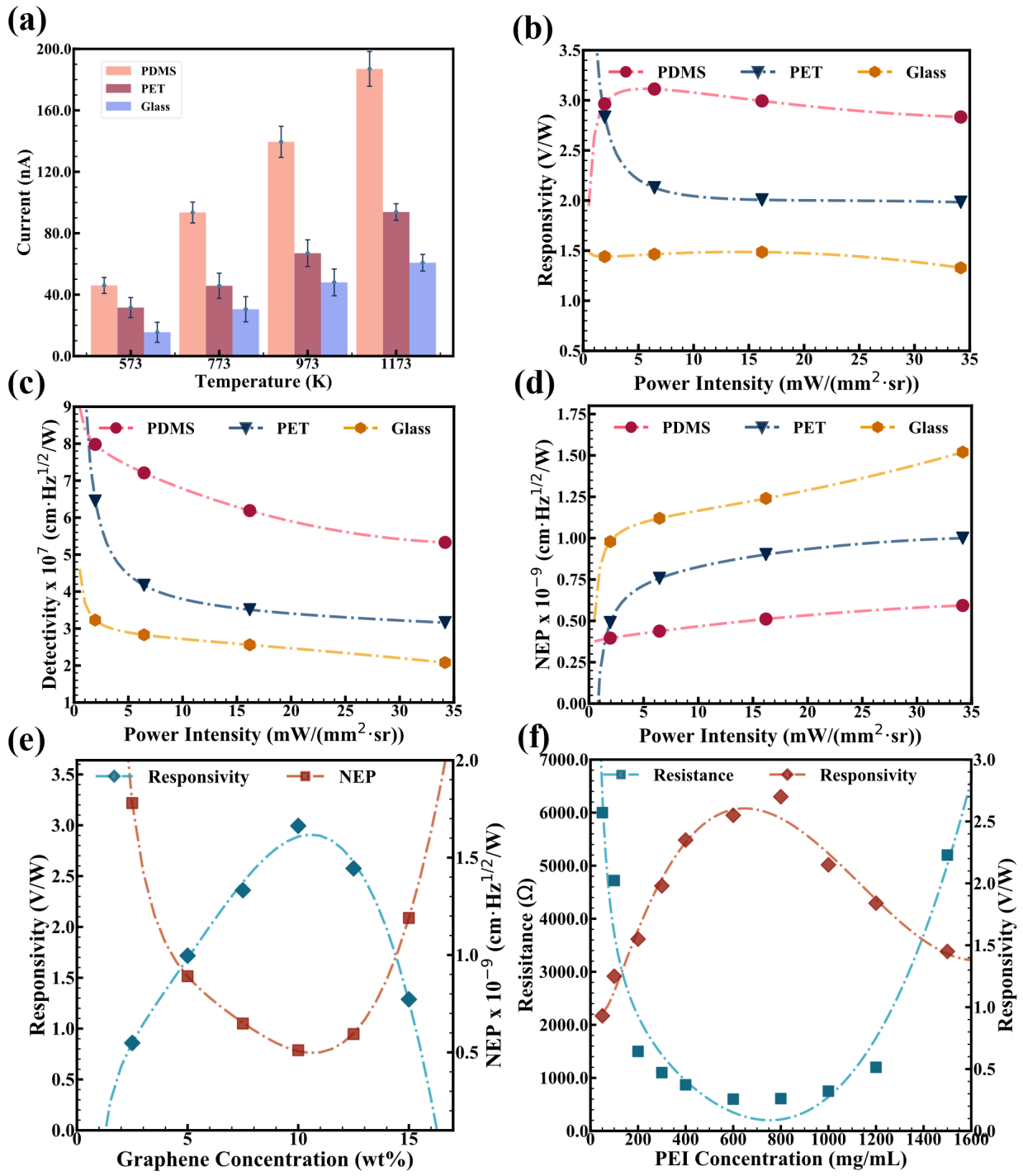
(a)
PDMS
PET
Glass
Current (nA)
Temperature (K)
(b)
PDMS
PET
Glass
Responsivity (V/W)
Power Intensity (mW/(mm^2·sr))
(c)
PDMS
PET
Glass
Detectivity x 10^7 (cm·Hz$^{1/2}$/W)
Power Intensity (mW/(mm^2·sr))
(d)
PDMS
PET
Glass
NEP x 10^{-9} (cm·Hz$^{1/2}$/W)
Power Intensity (mW/(mm^2·sr))
(e)
Responsivity
NEP
Responsivity (V/W)
NEP x 10^{-9} (cm·Hz$^{1/2}$/W)
Graphene Concentration (wt%)
(f)
Resistance
Responsivity
Resistance (Ω)
Responsivity (V/W)
PEI Concentration (mg/mL)

Figure 4-11. Optimization of graphene/PEI PTE performance: **(a)** Photocurrent under various blackbody temperatures, from 573K to 1173K. **(b)-(d)** Responsivity, detectivity, and NEP of graphene/PEI detectors on PDMS, PET, and Glass substrates under multiple power intensities. **(e)** The PEI concentration factor reflects the detector's resistance and responsivity. **(f)** Increasingly tunable graphene loadings (2.5 wt% to 15 wt%) affect the responsivity and NEP of the detector.

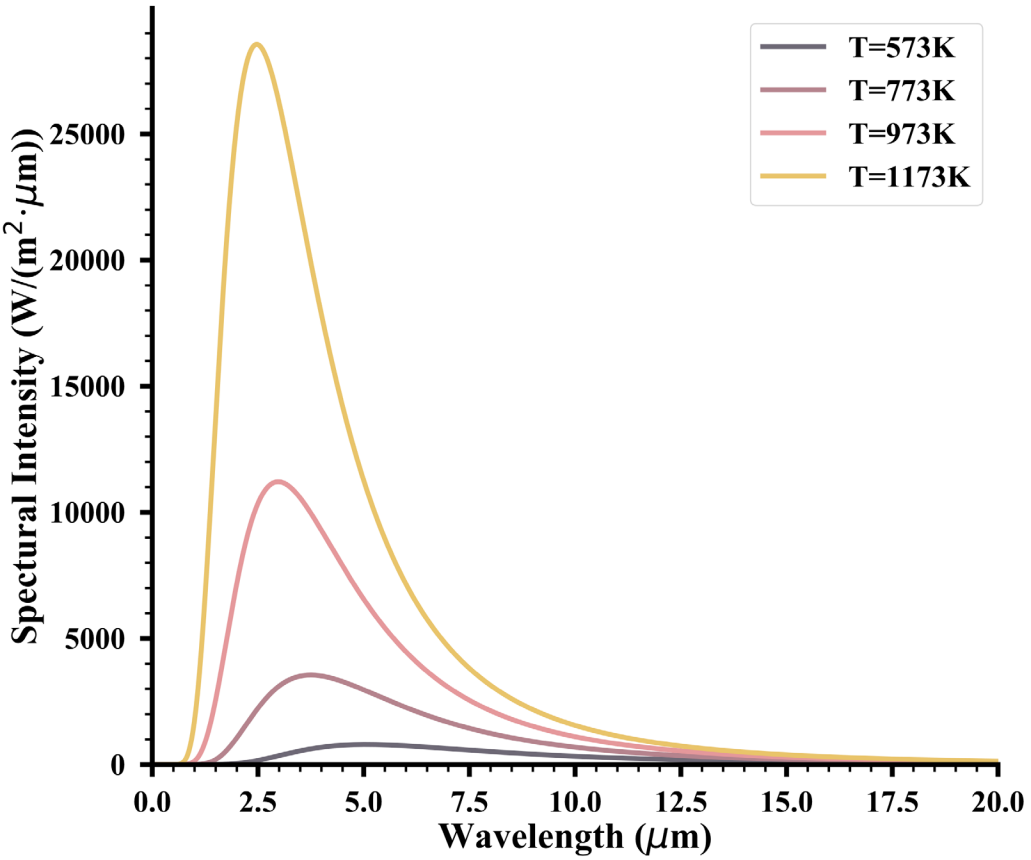

Figure 4-12. Blackbody spectral radiation curves under a temperature of 573 K, 773 K, 973 K, and 1173 K. The wavelength of peaks ranges from 5.1 μm, 3.7 μm, 3.0 μm, and 2.4 μm, respectively.

4.5 PTE performance optimization

We further investigate the concentration of PEI and graphene in the spray-coating method. Figure 4-11(e) shows that the PEI concentration starts from 100 mg ml^{-1} to 1500 mg ml^{-1}, maintaining the graphene concentration at the same 10 wt %. The resistance of the synthesized material increasingly drops from 6.2×10^3 Ω to less than 1.1×10^3 Ω, and the responsivity increasingly improves. This optimization may be attributed to increasing viscosity, uniform dispersion, and thermoelectric conversion. First, as the PEI concentration increases, the mixture's viscosity will increase inside the tiny droplets by the spray coating [151]. Thus, the droplets may form more stickily on the surface of the substrates. Second, the graphene may disperse nicely inside the polymer matrix and bridge the connections with another droplet. Thirdly, the thermal conductivity of the graphene/PEI is optimized. Graphene, as a superior light-sensitive material, is not sufficient to convert thermoelectric energy due to its high thermal conductivity [152]. However, the involving PEI concentration may assist the thermoelectric conversion by significantly mitigating the thermal conductivity [153], where a figure of merit can evaluate the efficiency of thermoelectric conversion, $ZT = \frac{\sigma s^2 T}{k}$ [154]. σ represents the electrical conductivity, S is the Seebeck coefficient, and k equals the thermal conductivity. Hence, the value of ZT can be enhanced achieve, and the overall performance of PTE conversion may improve, as shown in the responsivity raising 1.3 V W^{-1} to 2.7 V W^{-1}. While the PEI concentration increases to 1200 mg ml^{-1}, the resistance rapidly boosts to 5.7×10^3 Ω. This phenomenon is considered for the extremely PEI colloidal conjugation as the graphene powder is stickily stacked together by attractive solid Van der Waals forces [155, 156]. Thus, the significant droplet coalescence obstacle the path of carriers to transport in the PEI matrix, reduce the contact surfaces of the substrates, and rapidly decrease the performance of the detectors while the responsivity turning 2-fold rise as the comparison with lower PEI concentrations.

Another primary consideration is the content of the graphene power as the photoactive material. The overall responsivity and NEP noise are shown in **Figure 4-11(f)**. Enhanced PTE responsivity is observed with the increase of graphene concentration from 2.5 wt% to 10 wt%, accompanied by decreased NEP power. The involvement of the graphene powder stimulates the photon energy absorption and thus increases the photoresponse. Another point stands for increased electrical conductivity and sufficient phonon scattering [157]. As continuously turning the graphene concentration to 15 wt %, the descending of responsivity from 2.7 V W^{-1} to 1.3 V W^{-1} can be noticed under the same illumination environment. This scenario may distribute to the aggregation of graphene flakes. The disuniformity of materials will increase defect structures and obstacles to converting photon energy [158]. Besides, the increased thermal conductivity may be considered one factor leading to decreased photo responsivity, and the Seebeck coefficient is potentially affected under higher carrier concentrations [140, 159].

Other technical factors, including the spraying directions, repeating cycles (**Figure 4-13**), the atomizing pressure (**Figure 4-14**), the drying temperature (**Figure 4-15**), the cooling rate, and the spray feeding rate (**Figure 4-16**), probably may affect the overall PTE performance of graphene/PEI detectors [160, 161]. Overall, the spray coating can precisely control the height of the graphene/PEI layer as 4.78 ± 0.5 μm, overcoming the 142 ± 6.7 μm compared to the drop-casting method under the same resistance **(Figure 4-8**). In general, the vertical architectures of graphene/PEI detectors conduct advantages compared to the planer-induced detectors. First, the vertical structure is relatively insensitive to the source spots instead of overcoming complications in precisely controlling the focal position on the intersections in electrodes, sensitive materials, and optical radiation alignment. Second, the vertical position may absorb the insert photon energy

more efficiently due to broadband light-sensitive areas and top thin electrodes for assisting illumination penetrating the absorbing layers, facilitating the low-cost, large-compact detectors.

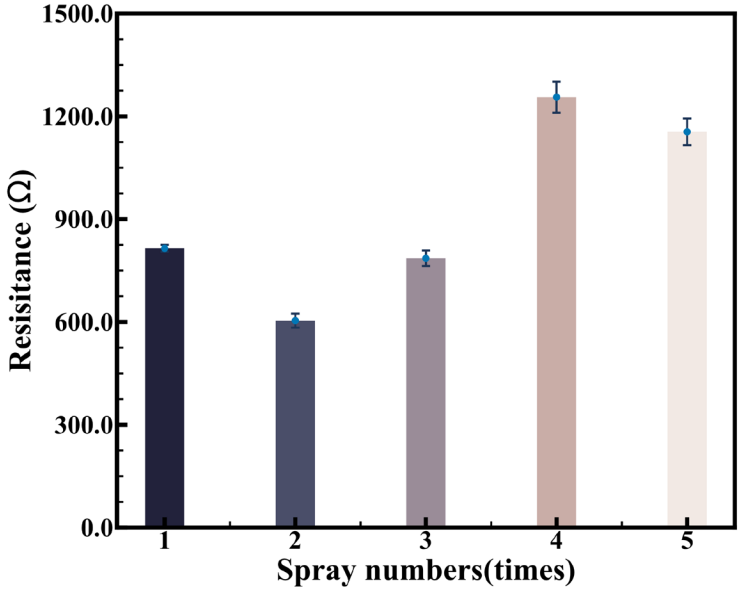

Figure 4-13. The effect of the number of spraying times on graphene/PEI material. The direction of one time is defined as the zig-zag direction from top to bottom.

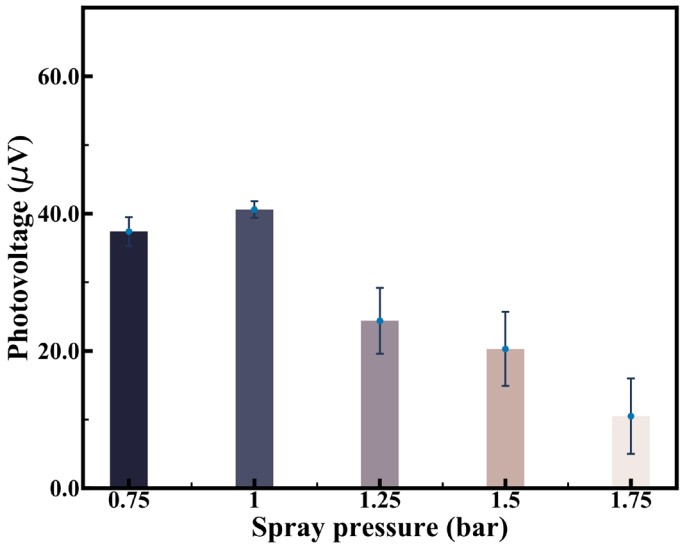

Figure 4-14. The effect of the spraying pressure on graphene/PEI material.

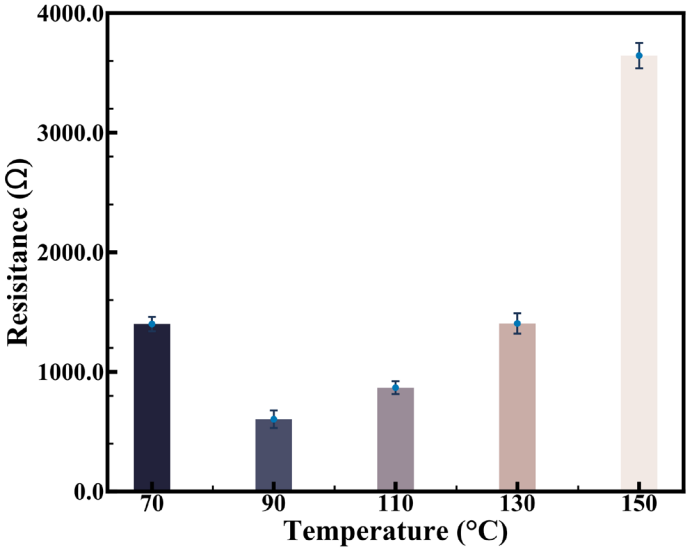

Figure 4-15. The effect of the drying temperature on graphene/PEI material.

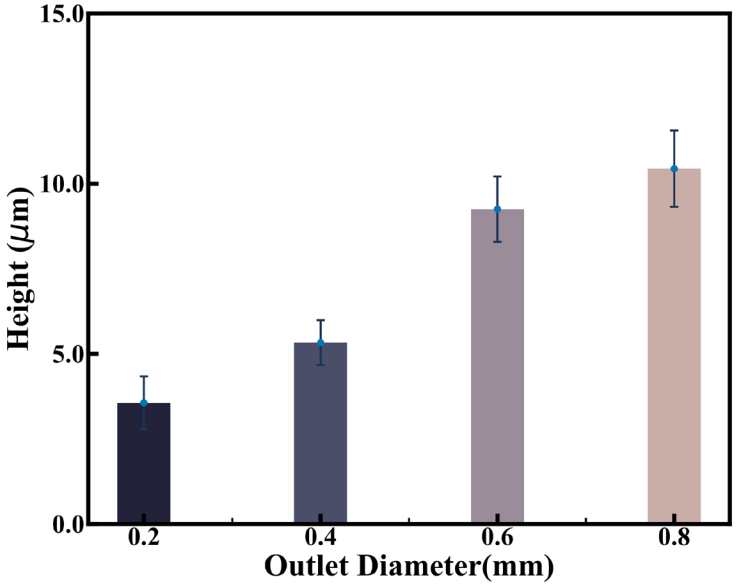

Figure 4-16. The effect of the outlet diameter (or the spray feeding rate) on graphene/PEI material.

As compared with recent polymer-based photodetectors and graphene PTE detectors (**Table 4-1** and **Table 4-2**), our graphene/PEI composite PTE performance results reach the top level with a detectivity of 6.05 × 10^7 cm $Hz^{1/2}$ W^{-1} and 2.7 V W^{-1} response in imitating real-world, low-intensity blackbody radiation. This attribution is owing to the combination of graphene/PEI

composite material and spray coating method. The zero-bias graphene provides broadband absorption of most infrared wavelengths, and its room-temperature stability overcomes the potential of rapid oxidation and deformation. PEI may manipulate mechanical flexibility, thermal conductivity, structural composite matrix, and affinity with variable substrates [136]. The cost-effective spray coating method assists in atomizing composite into smaller fluid masses, changing the surface tension, and achieving multi-element designs on hydrophobic and hydrophilic surfaces. This graphene/PEI detector will be applied as remote NDT detection for industrial monitoring, wearable human body health detectors, as human radiation wavelength ranges from medium wave infrared to long-infrared wave [162, 163], non-contact human interaction sensors to avoid coronavirus infection, and outer spacing cameras.

Table 4-1 Comparison of polymer (composite) based photodetectors.

Photoactive layer	**Mechanism**	**Responsive Range**	**Responsivity**	**Detectivity**	**Bias Voltage**	**Flexibility**	**Ref**
Graphene@PEI	PTE	LWIR to MWIR	2.7 V W^{-1}	6.05×10^{7} cm $Hz^{1/2}$ W^{-1}	N/A	√	This work
Graphene@Doped-PANI	PTE	LWIR to MWIR	2.5 V W^{-1}	6.8×10^{7} cm $Hz^{1/2}$ W^{-1}	N/A	√	[16]
CNT@PEDOT:PSS	PTE	LWIR to MWIR	0.15 V W^{-1}	1.9×10^{7} Jones	N/A	×	[164]
CNT@PVA	PTE	LWIR to MWIR	0.1 V W^{-1}	4.9×10^{6} cm $Hz^{1/2}$ W^{-1}	N/A	√	[132]
Graphene@PEDOT:PSS	PTE	LWIR to MWIR	0.27 V W^{-1}	1.4×10^{7} cm $Hz^{1/2}$ W^{-1}	N/A	√	[34]
Helical Carbon Nanotubes @PEDOT:PSS	PTE	NIR	166.01 mW cm^{-2}	N/A	N/A	√	[165]
Manipulate nanowires@Te-Ag_2Te-Ag NW film	PTE	NIR to MWIR	4.1 V/W	944 $MHz^{1/2}$ W^{-1}	N/A	×	[134]

Table 4-2 Comparison of graphene-based photodetectors.

Photoactive layer	Mechanism	Responsive Range	Responsivity	Detectivity	Bias Voltage	Flexibility	Ref
Graphene@PEI	PTE	LWIR to MWIR	2.7 V W^{-1}	6.05×10^{7} cm $Hz^{1/2}$ W^{-1}	N/A	√	This work
Microporous Graphene (3DMG) @Liquid gating	PTE	THz	0.012 V W^{-1}	2.3×10^{6} cm $Hz^{1/2}$ W^{-1}	-2 to 2 V	×	[166]
Graphene@ PEDOT:PSS	PTE	LWIR to MWIR	0.27 V W^{-1}	1.4×10^{7} cm $Hz^{1/2}$ W^{-1}	N/A	√	[34]
Graphene@Ecoflex	PTE	UV to Visible	42 μA W^{-1}	N/A	N/A	√	[167]
Reduced Graphene Oxide (RGO)	PTE	UV to THz	0.003 V W^{-1}	6.7×10^{6} cm $Hz^{1/2}$ W^{-1}	N/A	√	[131]
Graphene@P/N junction	PTE/Plasmonic	Visible	0.25 mA W^{-1}	N/A	-2 V to 9 V	×	[125]
Graphene@Doped-PANI	PTE	LWIR to MWIR	2.5 V W^{-1}	6.8×10^{7} cm $Hz^{1/2}$ W^{-1}	N/A	√	[16]

4.6 Stability and flexibility investigation

One critical concern is the stability and flexibility of our graphene/PEI PTE detectors. The combination of durable photoresponse and flexible ability is revealed from the graphene/PEI on PET substrate (**Figure 4-17(a)**). **Figure 4-17(b)** illustrates the graphene/PEI photovoltage response under various bending recycles. The graphene/PEI materials can endure massive bending, even 400 times from a 90° bending angle. Besides, the graphene/PEI detectors can endure multiple bending radii (starting from -2 cm to 2 cm, increasing by 0.5 cm per run) after the detectors return to the flat state, indicating the swiftness of our materials and strong interactions between the

graphene/PEI composite and the substrate, maintaining the rapid and stable PTE response in **Figure 4-17(c)**. Furthermore, the stability of the graphene/PEI detector is carefully examined under the ambient surroundings with the same testing conditions. **Figure 4-17(d)** shows that the substrate's voltage is relatively stable for 30 days. Even for an extended period, there's only less than a 10% drop in the performance owing to the excellent protection and effective resistance of the oxidation of the material. Our graphene/PEI PTE detectors can sustain long-term stability within the ambient surroundings, resist bending motion, and withstand critical concave and convex folding, making it a potentially promising wearable application.

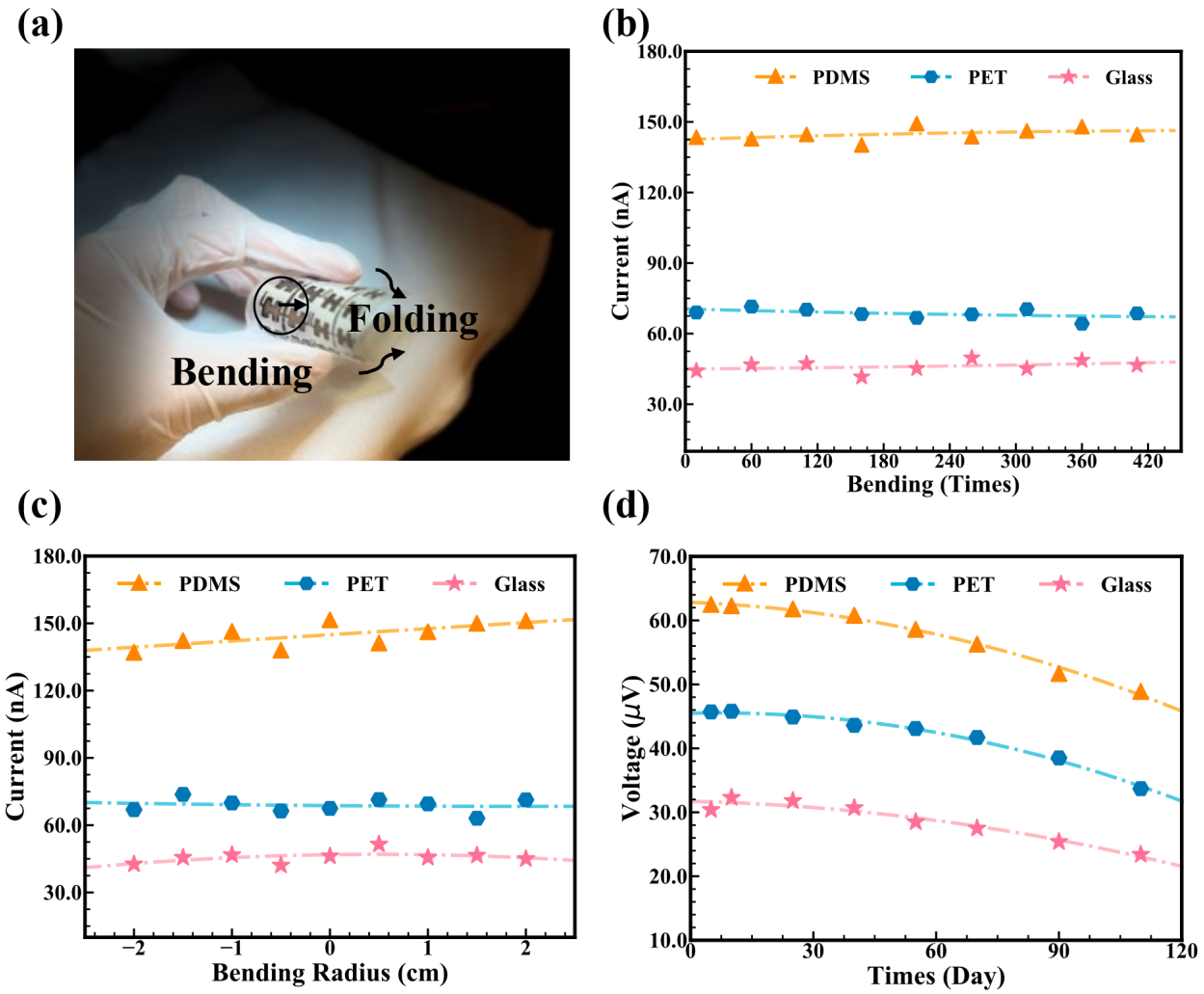

Figure 4-17. Stability and Flexibility measurement of graphene/PEI detector. **(a)** A testing flexible 4×4 array on the PET substrate sustains huge bending curves. **(b)** Stable photocurrent under multiple bending cycles. **(c)** Photoresponse under various bending radii from -2 cm to 2 cm. **(d)** Long-term stability of the graphene/PEI detector in an ambient environment.

4.7 NDT measurement

A single graphene/PEI PTE image sensor is placed onto the holder with micrometer caliper adjustment by sleeves (**Figure 4-18(a)**). And target objects, an aluminum crossing, and a copper key are attached to the back of the opaque plastic board (**Figure 4-18(d)** and **(e)**), with black tapes coated on the front surface of the board to block any visible ambient radiation (**Figure 4-19**). Each target is fixed on a PMMA carrying board hole, controlled by MPC-200 steppers and MP-285 micromanipulators on XY-axis 2D plan stage. The tapes, testing objects, and the opaque board had different infrared absorption; thus, the system could obtain their specific PTE signals. Besides, the PTE voltage and data logger is recorded by Keithley 6500.

Similarly, a specified germanium IR lens filters the IR radiation and blocks heat fluctuation. As for the NDT measurement, the stepper is carried out by MPC-200 steppers and MP-285, motivated by a laptop with self-written codes at a stable step of 200 μm on the X-axis or Y-axis, acquiring a total of 25 mm × 25 mm mapping scale. All NDT images (**Figure 4-18(d)** and **(e)**) are plotted without optimized procedures and matched well with the original structures. The photovoltage response of surroundings and objects can be viewed from the margins with 2-3 fold variations. In addition, boundaries of key and crossing illustrations could be observed, and verified the outstanding capability of our graphene/PEI detectors in high penetration and high-spatial resolution.

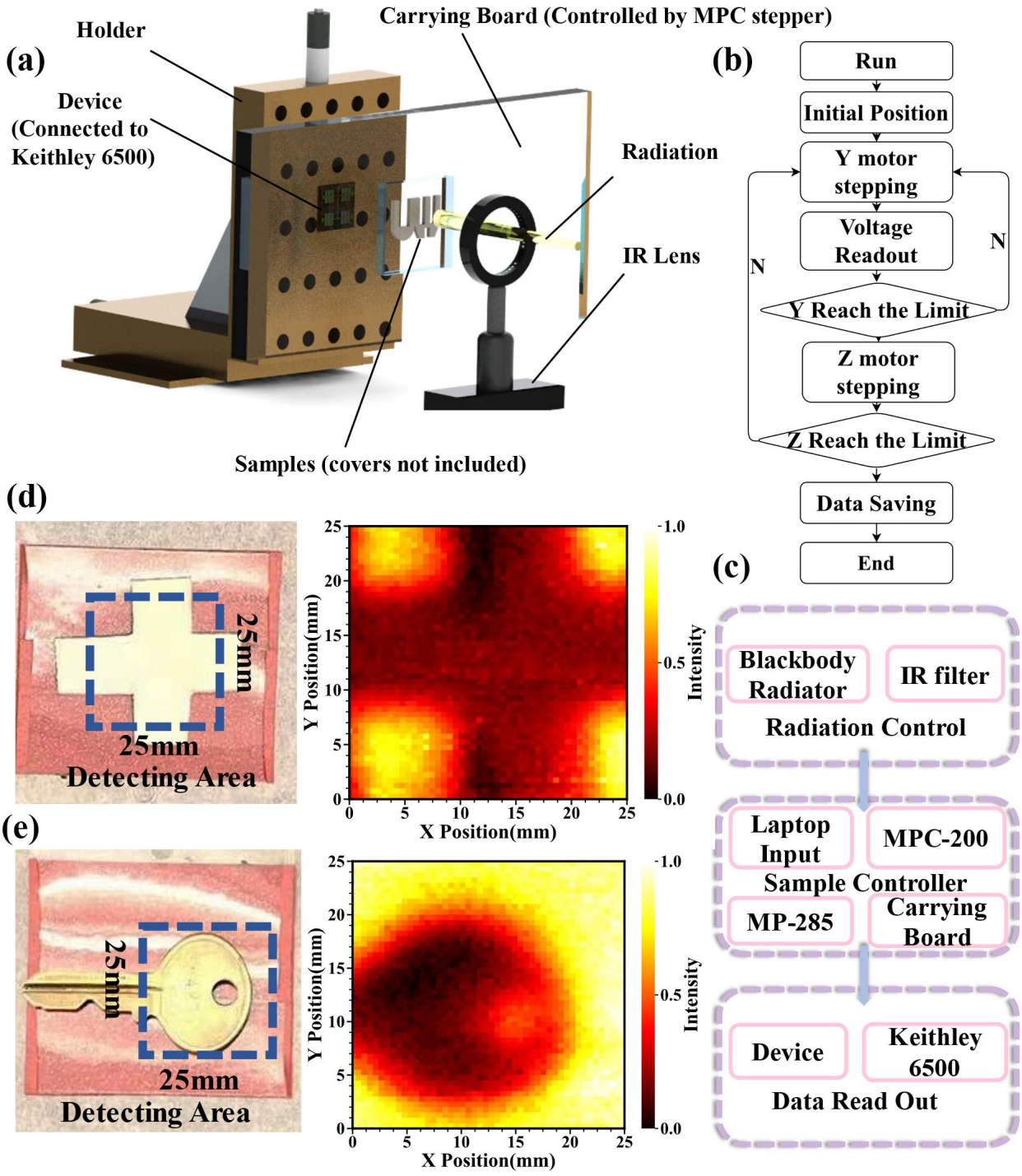

Figure 4-18. Schematic of NDT measurement platform. **(a)** The NDT platform overview includes a holder, a carrying board, a blackbody radiation source, and controlling steppers. **(b)** General

system formation chart. **(c)** Coding principles of mapping the samples and data analysis. **(d)-(e)** The PTE images of the cross and key samples using the NDT system.

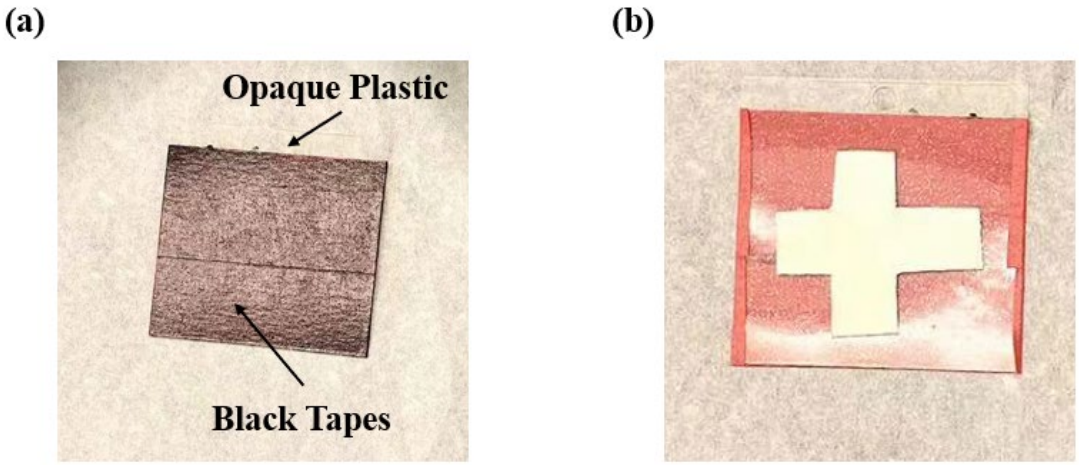

Figure 4-19. The front and back cover of the NDT testing sample. **(a)** The front is an opaque plastic covered with black tape. **(b)** The back is the attached sample.

4.8 Conclusion

This chapter successfully proposed self-power, low-cost, and flexible vertical PTE array detectors based on graphene and PEI composite within a unique spray-coating method. A high photovoltage detectivity of 6.05×10^7 cm $Hz^{1/2}$ W^{-1} and 2.7 V W^{-1} response is achieved at a 2.98 μm peak wavelength on PET substrate, focusing on realistic situations with low incident power. Besides, detailed optimization of PTE performance and spray-coating techniques are discussed, providing a peak performance at an 800 mg ml^{-1} PEI and 10 wt% graphene loading. Furthermore, stability and flexibility investigation proves 90-day long-term sustainability under an ambient environment. Finally, the NDT measurement adopting a single detector demonstrates the prominent applications in health electronics, remote industry monitoring, and wearable biological applications.

Chapter 5 Room-ambient Operation of Integrated and Visualized Photothermoelectric System with Patterned Mo_2C/PEDOT: PSS Flexible Devices

5.1 Aims and highlights

This chapter proposes a novel approach for fabricating a multi-array flexible Mo_2C/PEDOT: PSS PTE device on a Polyethylene terephthalate (PET) substrate, offering several key advantages. Our device achieves bias-free operation, self-power supply, and infrared broadband detection while demonstrating exceptional photon energy conversion. The success of our approach relies on meticulous fabrication techniques, pattern design development, and concentration manipulations. A spray-coating method that atomizes the solution into smaller droplets was employed to create a uniform mixture to reduce the surface tension on the contact surface [168, 169]. We also successfully manipulated a 3×3 pixel patterned array of devices by incorporating laser-induced masking and relative techniques. We optimize the Mo_2C concentration at 10 wt% to achieve impressive results. At this optimized concentration, our Mo_2C/PEDOT: PSS detector exhibits a responsivity of 4.2 V W^{-1} and a detectivity of 1.2×10^8 cm $Hz^{1/2}$ W^{-1} under 973 K blackbody radiation. This outstanding performance and the device's chemical stability and mechanical flexibility pave the way for integrated PTE systems. In addition, two demonstration PTE systems have been set up: a motion-tracking system and an NDT imaging system. These systems exhibit reliable sensitivity and high spatial resolution, enabling tasks such as fingertip tracking, curvature measuring, and deep fragment detection. The versatility of these promising systems extends beyond industry research, encompassing safety inspections, outdoor exploration, public health, human health monitoring, and wearable electronics.

5.2 Experimental

5.2.1 Synthesis of Mo_2C/PEDOT: PSS solution

As shown in **Figure 5-1 (a)**, various Mo_2C powder (2.5 wt% to 20 wt%, with an increment of 2.5 wt%) was dissolved into 4 mL DMSO solution, followed by 30 mins tip sonification and 12 hours magnetic stirring for complete delamination. Second, the suspension was transferred to vials and centrifuged at 2000 rpm for 15 min, separating the sediment and supernatant. Then, by disposing of the upper supernatant and adding DI water into the sediment, we repeated the previous step several times until the top of the supernatant was transparent. The remaining sediment was post-baked at 30 °C for 10 hours to remove moisture. Next, the dried powder was mixed with 3mL PEDOT: PSS overnight for 24 hours of magnetic stirring. Finally, the Mo_2C/PEDOT: PSS solution was obtained and stored at room temperature.

5.2.2 Mo_2C/PEDOT: PSS device fabrication

Silicon, glass, and PET substrate were cleaned with Isopropyl alcohol and acetone and treated with plasma. The previous Mo2C/PEDOT: PSS solution was added into the spray nozzle (purchased from TC-20B series, Spedertool), setting at 0.5 bar pressure. The flow rate was controlled under 0.75 mL min-1, and the 0.2 mm-diameter spray outlet was placed 15 cm over the surface. A specified laser-involved mask was placed over each substrate, and the spray was controlled and moved in a zig-zag direction. After repeated spraying for two rounds, well-dispersed substrates were baked under the oven, drying at 35 °C for 24 hours with nitrogen gas protection, evaporating moisture and reducing surface tension. All baked devices are deposited with 1000 nm Titanium (Ti) and 300 nm Aluminum (Al) electrodes using an e-beam evaporator (ANGSTROM-Ebeam). Cost-effective shadow masks were carried out to control the size of the circuit, avoiding any short

circuit and potential photoresist pollutions of the Mo2C/PEDOT: PSS materials. Finally, the 3×3 array detectors outlined electrodes were bonded with silver conductive epoxy, accompanying Parafilm circuit protection bounding under for 12 hours at room temperature to dry out (**Figure 5-1 (b)**).

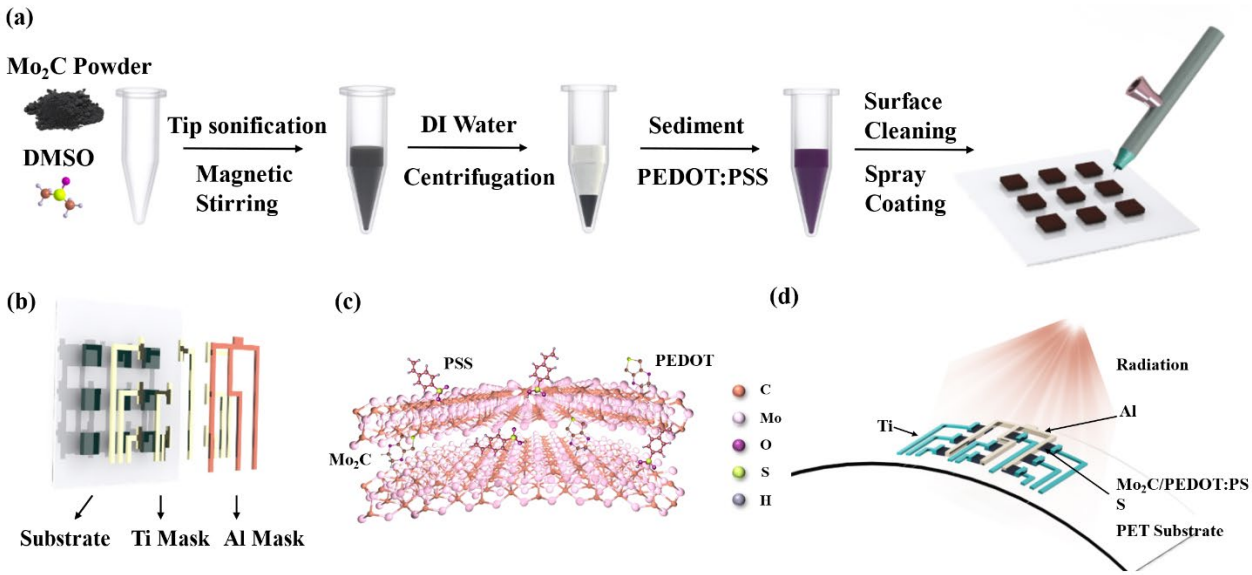

Figure 5-1. The fabrication process of the Mo_2C/PEDOT: PSS detector. **(a)** Schematic of the process of Mo_2C/PEDOT: PSS solution and spray coating method applied to form patterned detectors **(b)** Electronics deposition with laser-induced mask alignment. **(c)** Concept of Mo_2C/PEDOT: PSS materials **(d)** PTE Mechanism of Mo_2C/PEDOT: PSS detector.

5.2.3 Mo_2C/PEDOT: PSS Seebeck coefficient measurement system

Continuing with the previous Mo_2C/PEDOT: PSS solution synthesis, 5%, and 10% PVA are separately added into the material with 50 °C oven heating, stirring the mixture, and pouring on plates for 24 hours cooling down to form membranes. Then the Mo_2C/PEDOT: PSS/PVA membrane is transferred on the specific homemade Seebeck coefficient system. The system contains two temperature plates; one is stable at 0 °C, and the other can be adjusted from 20 to

50 °C. The membrane is placed between two temperature plates, and a couple of the thermocouples are bounded on the side of the membrane separately. One can calculate the Seebeck coefficient S by switching the temperature difference between two plates.

$$S = -\Delta U/\Delta T \tag{5-1}$$

ΔU stands for the voltage difference of both sides, and ΔT refers to the manual temperature difference settings.

5.2.4 Current-voltage curve measurements

The characterization of the I-V curve was measured by a Keithley 6500 multimeter (current recording, TEKTRONIX, Inc)) and Keithley 6487 (voltage providing, TEKTRONIX, Inc.). The detector was put inside a self-made opaque system to mitigate the influence of surrounding illustration. An infrared germanium filter cuts off the wavelength below 1.5 μm and controls the radiation input to optimize the infrared range in the detector. A temperature-controllable blackbody radiation (Newport Oriel 67030) is applied to imitate the low-intensity IR radiation.

5.2.5 SEM image

The overall morphology of the Mo_2C/PEDOT: PSS and Mo_2C flakes details in the material was examined by a scanning electron microscope (JEOL JSM-7200F), setting 5 kV voltage and 10-12 nA beam current (**Figure 5-2**).

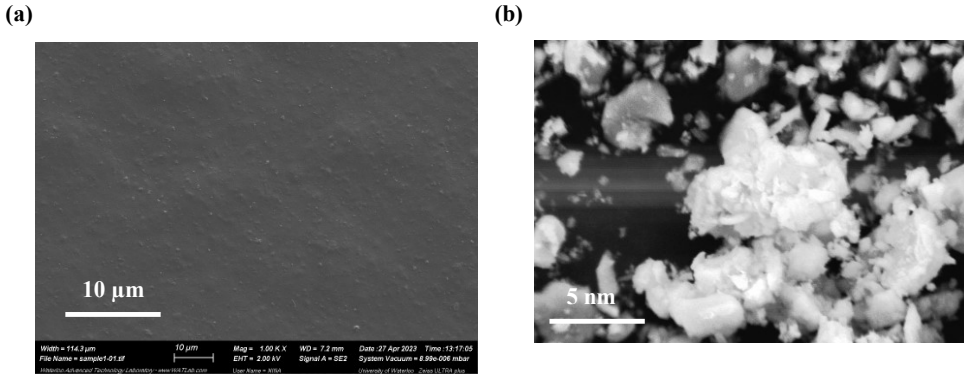

Figure 5-2. SEM images of the **(a)** Mo2C/PEDOT: PSS. **(b)** Mo2C flakes. Materials were examined by a scanning electron microscope (JEOL JSM-7200F), setting 5 kV voltage and 10-12 nA beam current.

5.2.6 Raman curves

Figure 5-3 in the Raman depicts the Raman curves of the Mo_2C/PEDOT: PSS by Bruker Senterra-2 Raman with a 785 nm laser. The output power was set at 10 mW with 20 s integration time. The Mo-C band peaks of the Mo_2C appear at around 814 and 965 cm^{-1} to confirm the formation of a Mo_2C phase. The D, G band peaks appear at 1363 and 1580 cm^{-1}, indicating defects and the primary vibration of the sp^2-hybridized zone [170, 171]. With the addition of the PEDOT: PSS, the peak of the D and G bands slightly shift to the smaller area, demonstrating sp^2 solid interactions [15, 103].

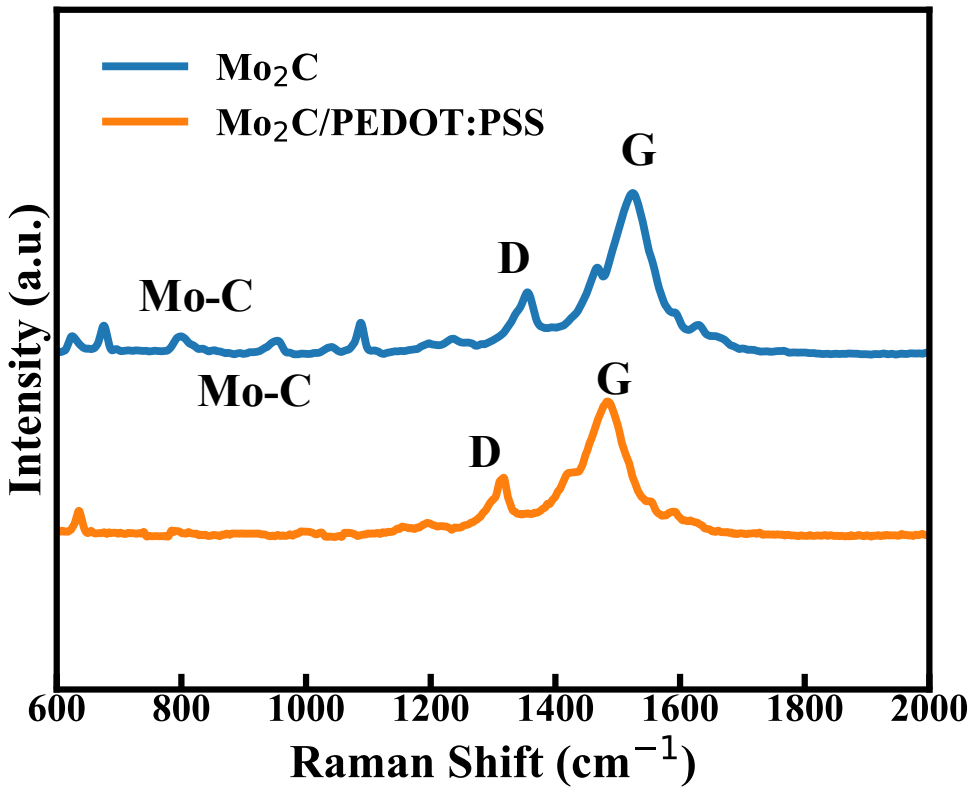

Figure 5-3. Raman curves of the Mo_2C and Mo_2C/PEDOT: PSS.

5.2.7 FTIR curves

Transmittance mode of the Mo_2C/PEDOT: PSS FTIR curves from 400 to 4000 cm^{-1} wavenumbers were conducted by Bruker Tensor 27 FTIR scanning (**Figure 5-4**).

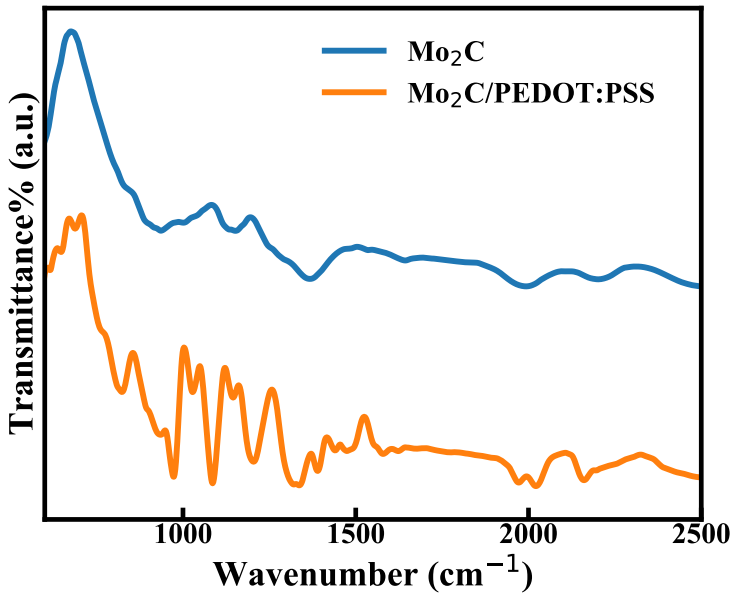

Figure 5-4. FTIR image of the Mo_2C and Mo_2C/PEDOT: PSS. Mo_2C does not represent heavy absorption peaks.[172] While adding PEDOT: PSS, several peaks appear due to the bonds in the PEDOT and PSS [173, 174].

5.2.8 Height measurements

The Mo2C/PEDOT: PSS height in PET, silicon, and glass substrates were compared through a surface profilometer (BRUKER-profilometer) (**Figure 5-5**).

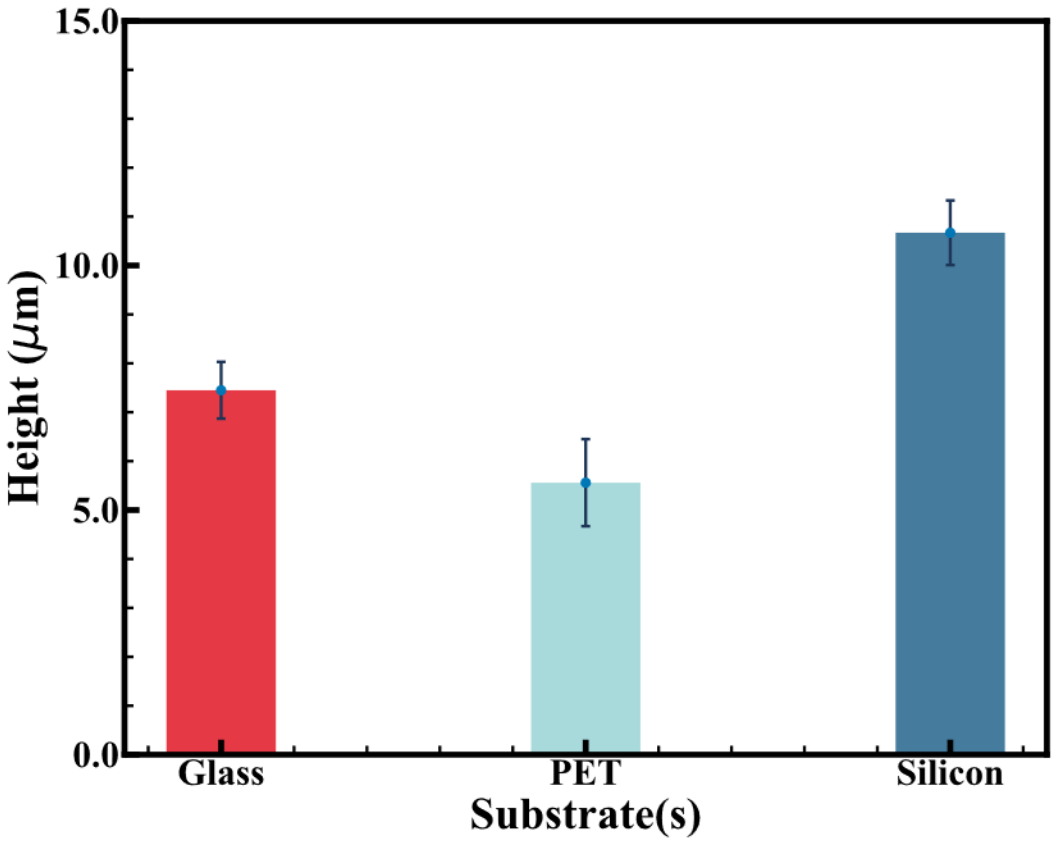

Figure 5-5. The Mo_2C/PEDOT: PSS height in glass, PET, and silicon substrates through a surface profilometer. The height of the sample in each substrate is 7.45±0.58, 5.56±0.89 and 10.67±0.66 μm, respectively.

5.3 Results and discussion

5.3.1 PTE mechanism

The PTE mechanism can be explained into two pathways, the photothermal conversion and the thermoelectric conversion. Figure 1d illustrates the PTE conversion in Mo_2C/PEDOT: PSS detector: while the lights of photons illuminate the material, the solid light-matter interaction leads to a tremendously increasing in the global temperature of electrons and lattices, and then delocalized hot carriers (i.e., electrons) are facile to change while lattice vibration remains

unaffected, thus generating the asymmetric temperature gradient from a hot region to the cold region. Due to the high heat sink of two metal electrodes with strong infrared reflection, electrons mainly flow through the Mo_2C/PEDOT: PSS channel and create the voltage along the horizontal pathway [175–177], whose scenario can be explained with the equation:

$$V = \sum_{Ti}^{Al} \int S_i \nabla T_i dl = \int_{Ti}^{MPP\text{-}Ti} S(l) \nabla T(l) dl + \int_{MPP\text{-}Ti}^{Al\text{-}MPP} S(l) \nabla T(l) dl + \int_{Al\text{-}MPP}^{Al} S(l) \nabla T(l) dl \quad (5\text{-}2)$$

, where T_i represents the local temperature [178]. The above equation demonstrates the potential for optimizing the desirable maximum voltage by controlling the horizontal distance between two electrodes. Besides, efficient energy conversion from photon energy into thermal and electronic power indicates the demand for outstanding light absorption and high Seebeck coefficient material.

5.3.2 I-V curves and time response of Mo_2C/PEDOT: PSS detector

Figure 5-6 (a) illustrates the I-V curves of the Mo_2C/PEDOT: PSS detector. The results of the I-V curves from different substrates, including silicon, PET, and glass, show the linear relationship from -80 to 80 μV in the illustration of light and dark environments. Increasing the tunable voltage input from -1 mV to 1 mV without any amplifier assistance achieves stable linearity of each type of substrate, with a range of 10^3 resistance. The straight lines prove the stability of the PTE energy conversion and the superiority of the blocking temperature effects on resistance compared to rapid temperature effects on bolometers. Another possible reason is the compact contact between the substrate and the Mo_2C/PEDOT: PSS. Besides, the PET substrate performs best among the three substrates, and the silicon substrate has the lowest photocurrent response. This performance indicates PTE conversion of the silicon substrate is restricted by thermal conductivity, which is usually higher than PET and glass. Thus, the converted thermal energy is facile to dissipate through the electrons moving to generate photovoltages. Moreover, less surface tension on the silicon will

slightly increase the height of the Mo_2C/PEDOT: PSS layer (**Figure 5-5**), and the electrons may scatter more randomly along the electrodes. Therefore, the driving voltage will decrease compared to the other two substrates.

The above discussion can also be proved from the time domain result in **Figure 5-6 (b)**. **Figure 5-6 (b)** depicts the cycling photovoltage response with 973 K radiation temperature. Rapid time response, repeatable cycles, and steady output of silicon, PET, and glass photovoltages react within 5s, implying superior and efficient PTE conversion and uniform material synthesis. Also, the generations of voltages on the PET substrate reach the elevated top while the silicon touches the bottom, in agreement with the previous discussion of I-V curves. Based on the I-V curves and time cycling tests, Mo_2C/PEDOT: PSS on the PET substrate reveals its prevailing PTE energy conversion and stable ability, which may be utilized in various applications and portable IoTs.

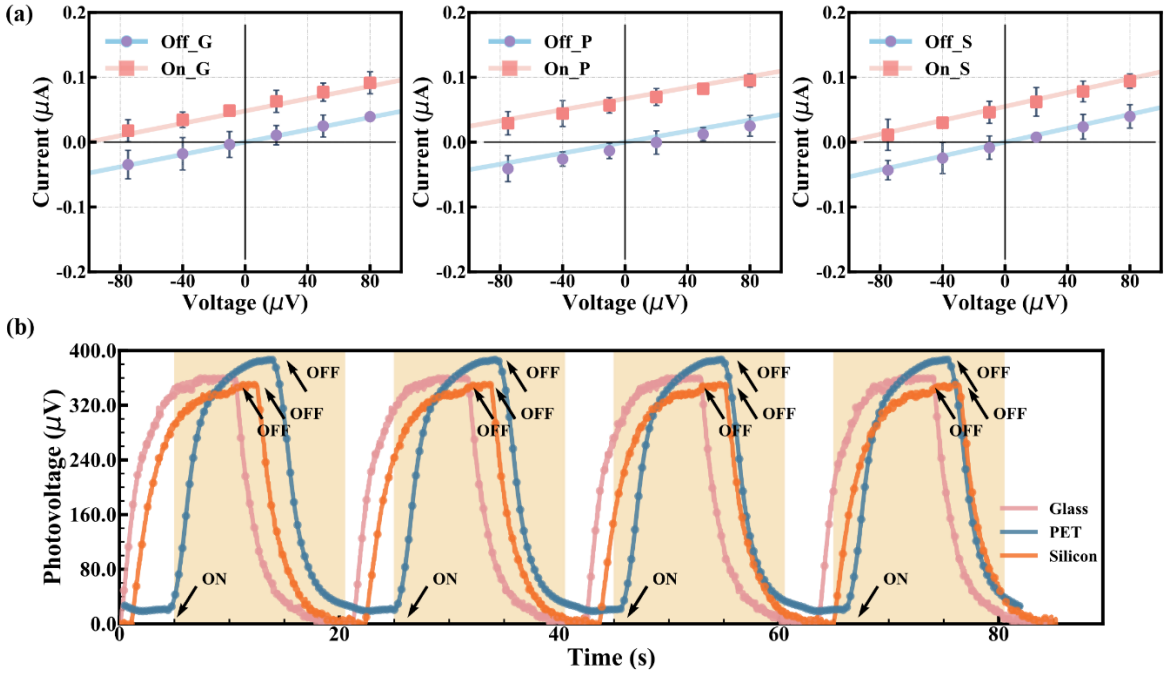

Figure 5-6. (a) I-V curves from different substrates, including glass(G), PET(P), and silicon (S), show the linear relationship from the -80 to 80 μV range in the illustration of light (ON) and dark (OFF) environments. **(b)** Photoresponse of the above three kinds of substrates with multiple cycles at 973 K radiation.

5.3.3 Mo_2C/PEDOT: PSS detector's PTE performance and its optimization

To further discuss the optimization of the material and its PTE performance, we adjust Mo_2C concentrations. **Figure 5-7 (a)** illustrates the Seebeck coefficient measurement of the sample with various Mo_2C concentrations. The results reveal the most significant value of the N-type Mo_2C/PEDOT: PSS/PVA membrane reaches -37.2 μV K^{-1} at 10 wt% Mo_2C loading. Higher Seebeck coefficient values usually indicate the superior ability for energy conversion from heat to electric power. Besides the Seebeck coefficient factor, other potential features can also determine the ability of the thermoelectric conversion. Thus, a figure of merit dimensionless parameter *ZT* value is involved in regulating the general efficiency of thermoelectric conversion, and it can be written as

$$ZT = S^2\sigma T/\kappa$$

In the equation, σ represents electrical conductivity, and κ stands for thermal conductivity [179]. The *ZT* value of Mo_2C/PEDOT: PSS may improve due to the high Seebeck coefficient of the component, enhanced electric conductivity of mixing solution with conjugation of the delocalized π-bond networks, and descending thermal conductivity by surface energy filtering, hence boosting the overall of the illumination energy conversion [34, 165].

Then, several merits are proposed and measured to determine the performance of the PTE mechanism. To quantify the sensitivity of the detector, the responsivity R_v can be expressed as

$$R_v = V_a / P_{in}$$

V_a represents voltage, and P_{in} implies the incident power [180]. Considering the ability to distinguish surrounding noise from the lowest absorbed photon energy, detectivity D^* is introduced as

$$D^* = R_v A^{1/2} / P_n$$

A refers to the material effective area, and P_n stands for the power of the noise, i.e., noise equivalent power (NEP). In PTE circumstance, without any bias support, the dominant power is considered the environment thermal noise, namely Johnson-Nyquist noise, and is written as

$$P_n = (4 k_B TR)^{1/2}$$

k_B is the Boltzmann constant, and R represents the detector's overall resistance [181]. As shown in **Figure 5-7 (b)**, the content fraction of graphene is switched from 2.5 wt% to 20 wt%, the optimized responsivity reaches the peak of the 4.2 V W^{-1}, and while the lowest NEP power is 1.06 × 10^{-9} cm $Hz^{1/2}$ W^{-1} at the 10 wt% concentration, coincidence with the maximum Seebeck coefficient. It's worth noting that the increment of Mo_2C concentration assists the photon energy absorption, thus increasing PTE responsivity. At the same time, the NEP power and the general resistance of the Mo_2C/PEDOT: PSS drops down due to the internal flake bridging inside of the PEDOT: PSS solution. However, when continuously increasing the Mo_2C concentration, the responsivity declines to 0.9 V W^{-1} with the increasing NEP power. The reason behind this scenario may be the aggregation of Mo_2C powder. Disuniform of the Mo_2C flask will form defects; thus, obstacles prevent free electrons from moving to generate voltage distributions. Also, involving overqualified concentrations will raise the thermal conductivity of the Mo_2C/PEDOT: PSS

materials, preventing heat dissipation from local blocks. Hence, the *ZT* value and conversion of photon energy may be influenced.

Besides the Mo_2C concentration, other factors, including radiation power input and preset temperatures, may also affect the overall PTE performance. **Figure 5-7 (c)** and **(d)** illustrate the effect of temperature from 573 K to 1173 K and illumination power from 8.23 to 35 mW $(sr \cdot mm^2)^{-1}$. The detectivity of Mo_2C/PEDOT: PSS detector raises to 1.2×10^8 cm $Hz^{1/2}$ W^{-1} at 2400 mW $(sr \cdot mm^2)^{-1}$ and then increasingly drops 5-fold to 0.6×10^8 cm $Hz^{1/2}$ W^{-1}. The responsivity is compatible with the response of detectivity. This enhancement indicates that absorption with infrared wavelength and the interaction between hot carriers and photons is suppressed with the photon energy increasing simultaneously. Hence, more electrons are guided by the temperature gradient and induce photovoltages. While reaching the peak of the 973 K, NEP and thermal conductivity play critical roles in the total PTE conversion, generating massive thermal noise and preventing thermoelectric conversion by heat dissipation.

Suitable substrates may also assist the conversion of photon energy from the PTE mechanism. Compared to solid substrates, such as silicon and glass, the flexible PET substrate behaves the prominent photoresponsivity and current with various power intensities and temperatures from the blackbody radiations, as shown in **Figure 5-7 (e)** and **(f)**. Several potential factors contribute to the performance, including previous discussions of lower heat dissipation with thermal conductivity, less surface tension with the spraying coating method, and material height guiding electrons moving directly along the horizontal direction. The overall Mo_2C/PEDOT: PSS with PET substrate demonstrate its superior PTE conversion in low-intensity blackbody radiation, broadband wavelength absorption from the infrared region, compatibility with spraying coating method to mitigate surface tension between materials and substrates, low-cost fabrications with

array design, long-term temperature stability to overcome fragility, delamination, and oxidation, paving a way of industrial manufacturing and applicable in various applications.

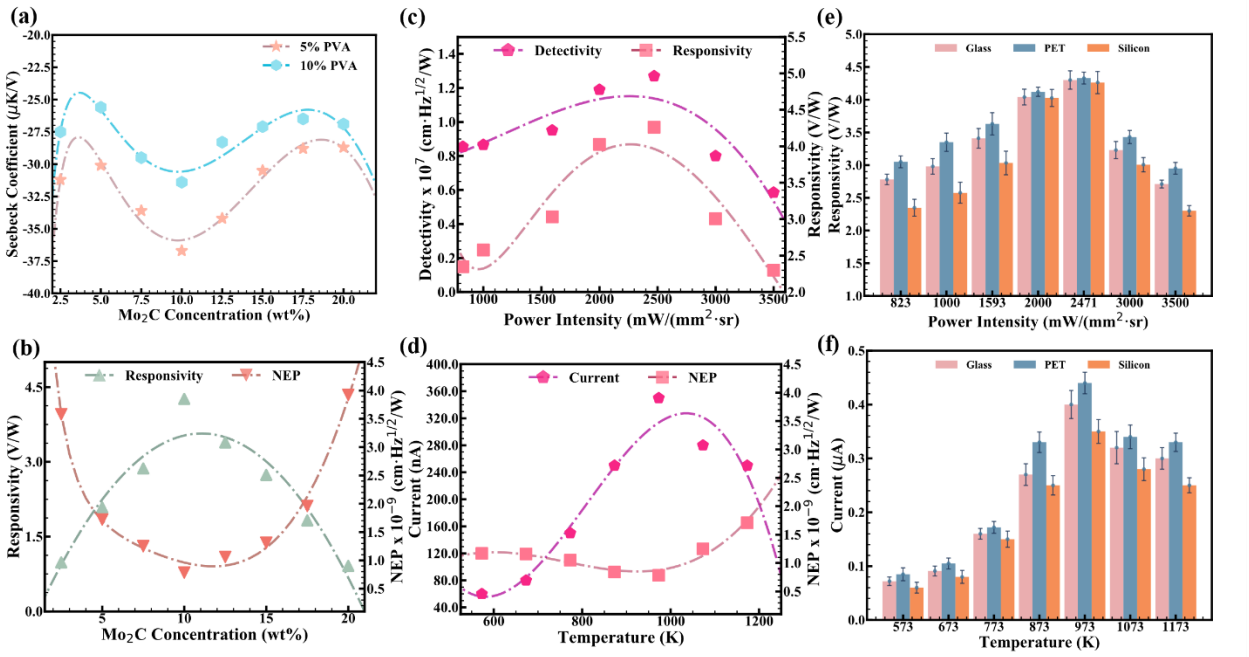

Figure 5-7. Optimizations of Mo_2C/PEDOT: PSS detector performance. **(a)** N-type Seebeck coefficient measurement with -37.2 μV K^{-1}. **(b)** Responsivity and NEP power with the Mo_2C concentration range from 2.5 wt% to 20 wt%. **(c)** Detectivity and responsivity with various blackbody radiation power intensities from 8.23 mW $(sr \cdot mm^2)^{-1}$ to 3500 mW $(sr \cdot mm^2)^{-1}$. **(d)** Current and NEP power of Mo_2C/PEDOT: PSS detector with temperature gradients from 573 K to 1173 K. **(e)** Responsivity comparison of glass, PET, and silicon substrates with various blackbody radiation power. **(f)** Photocurrent comparison of glass, PET, and silicon substrates with various temperatures.

5.3.4 Stability and flexibility of the Mo_2C/PEDOT: PSS detector

For flexible electronics, stability and flexibility are critical considerations in evaluating the performance of devices. Selecting silicon and glass substrates are considered as references. The stability of Mo_2C/PEDOT: PSS on PET, silicon, and glass substrates devices are proposed as the following methods: three kinds of devices are carefully placed in the ambient surroundings with 20-30 days of photovoltage response check, keeping all other factors. **Figure 5-8 (a)** shows these detectors' response is stable in the first 60 days. Although a slight decrease emerges for an extended period of 3 months, only a 10% voltage drop Mo_2C/PEDOT: PSS on PET substrate proves the long-term stability of the material and sustainability from surroundings. For the twisting resistance experiments in **Figure 5-8 (b)**, the PET substrate is held on the machine holder, turning both sides of the device for 180 degrees, and then recovered to its regular flattened state several times. No specific voltage turbulence is observed during the test, and no apparent cracks or fragility are found on the device. **Figure 5-8 (c)** and **(d)** depict the bending evaluations with multiple radii from -2 cm to 2 cm critical concave and convex bending motion several times at a stable 2 cm radius. Stable and persistent photovoltages are obtained, with fluctuation within 10%. In general, depending on the above evaluation, swiftness of the mechanical flexibility and durable stability of preventing oxidation appear Mo_2C/PEDOT: PSS on PET substrate, indicating potential applications in wearable devices and IoTs systems.

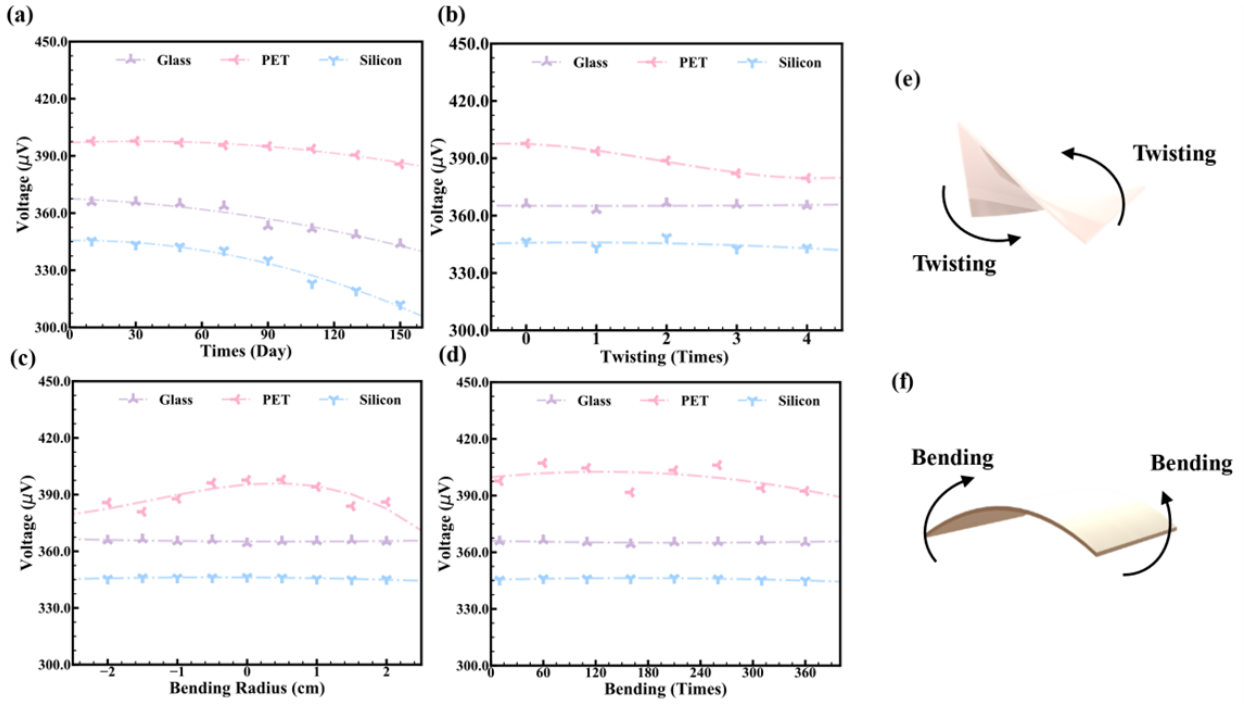

Figure 5-8. Stability and Flexibility of the Mo_2C/PEDOT: PSS detector on glass, PET, and silicon substrates. Note the glass and silicon substrates are selected as references **(a)** Long-term stability of photovoltage changes after 150 days. **(b)** Twisting stability tests 1-4 times. **(c)** Bending tests with various radii from -2 cm to 2 cm. **(d)** Concave and convex folding several times at a stable 2 cm radius.

5.3.5 Motion tracking system

Pandemic diseases cause significant concern in spreading viruses through human interactions. Preventing such human contact to maintain public health will inspire new noncontact tracking systems [182]. The peak of human radiation lies around 9.3 μm within the infrared detection region, facilitating human health monitors [183, 184]. Herein, we introduce a portable, noncontact, self-power, fast-response motion tracking system using the PET mechanism. As shown in **Figure 5-9(a)**, **(c)**, and **(d)**, fingertips are involved as the radiation source, which is low input infrared power. Accompanying the figure tips moving toward the 3×3 detectors at the platform, signals converted

from photon energy are parallelly delivered to the Arduino and TCSCAN Keithley 6500 multichannel systems. Both voltages are compared in **Figure 5-9(g)**, and various positions are controlled within error bars. Sensitive and selective photoresponse experiments are shown in **Figure 5-9(e)** and **(f)**. By controlling different fingertips' distances in the vertical directions, the voltage response with significant variations appears in 9 positions. Furthermore, compared to direct contact sensors, the noncontact PTE motion tracking system can fully utilize human radiation, avoiding contact materials dispersing bacteria and maintaining long-term system utilization and human safety. This motion tracking system can be utilized as publish bottoms, password interfaces, and gesture recording. We reckon this portable and self-power system has advantages over combining with neural network AI for graphics tablets, symbol recognitions, and human-machine interactions.

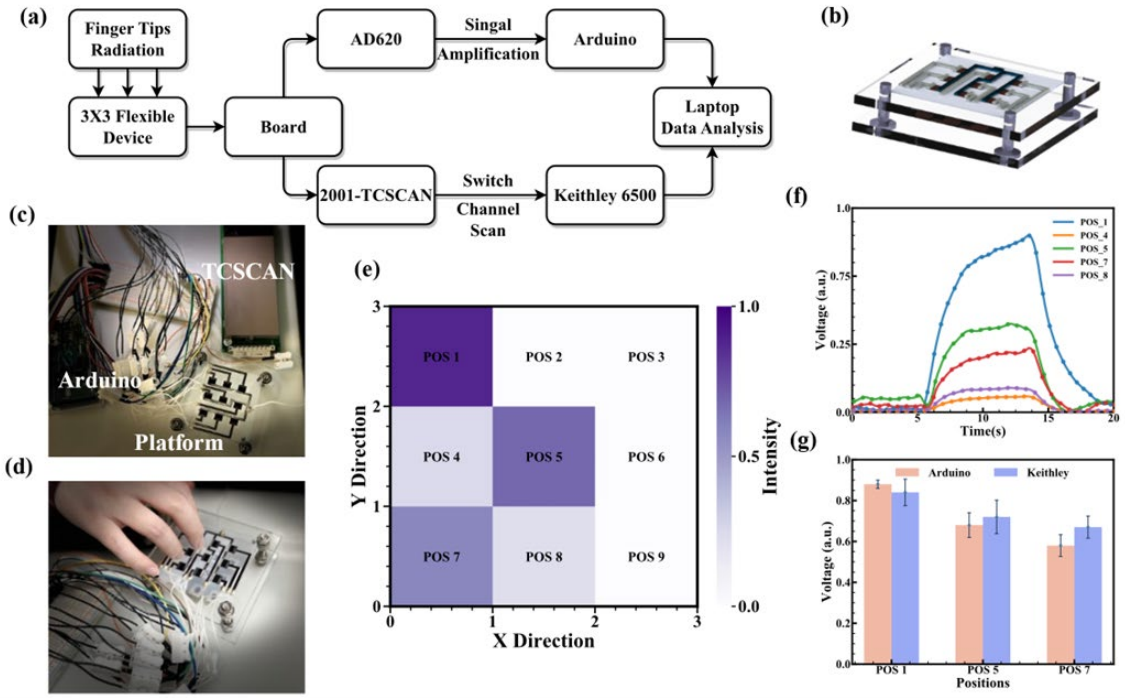

Figure 5-9. Integrated Mo_2C/PEDOT: PSS detector of the motion tracking system. **(a)** Schematic of the motion tracking system with Arduino and Keithley measurements. **(b)** Concept of the

integrated device platform. **(c)** Actual setup image of the motion tracking system. **(d)** Fingertips' motions in perpendicular directions with various distances with the system. **(e)** Data visualization with the fingertips' motion. **(f)** Current responses of the system in individual detectors. **(g)** Comparison of the Arduino and Keithley measurements.

5.3.6 NDT imaging system

Besides the above gestures tracking motion system, another consideration of the applications is the imaging system for NDT measurement. NDT has been widely used in engineering, outer space, security, and industries for troubleshooting, product evaluation, and manufacturing checking. It has been widely accepted as superior in timesaving, comprehensive testing, and non-destruction [185–187]. The PTE mechanism is compatible with the NDT measurement due to high effective energy conversion and low noise disturbance. Besides, the PET substrate can be applied to curvature surfaces due to its high flexibility. A potential model is visible in **Figure 5-10(a) and (b)**. Our NDT measurement system can be divided into three parts, the radiation system, the stage system, and the data analysis system. The radiation system includes the radiation source (Newport Oriel 67030) and infrared lens to select the region. Then the stage system part is implied with the sample holder and device holder, controlled by MPC-200 steppers and MP-285 micromanipulators. The testing objects are bound on the sample holder, and a flexible PET device is set at the device holder. The data analysis system converts data obtained from Keithley 6500 with USB cables to a laptop for a visual screen. **Figure 5-10(c)** and **(d)** demonstrate an 'h' shape structure with round curvatures matched on the 25 mm × 25 mm scale. **Figure 5-10(e)** and **(f)** prove a heart shape with additional fragments on the surface. Despite previous straight lines for NDT measurement, from the results in our sample, the NDT measurement system could reach curvature measuring and deep fragment detection for complex structures with high penetration and high spatial resolution.

Moreover, the system can be operated in ambient surroundings, which may benefit packaging imaging systems, security checks, industries, and agricultural food inspections.

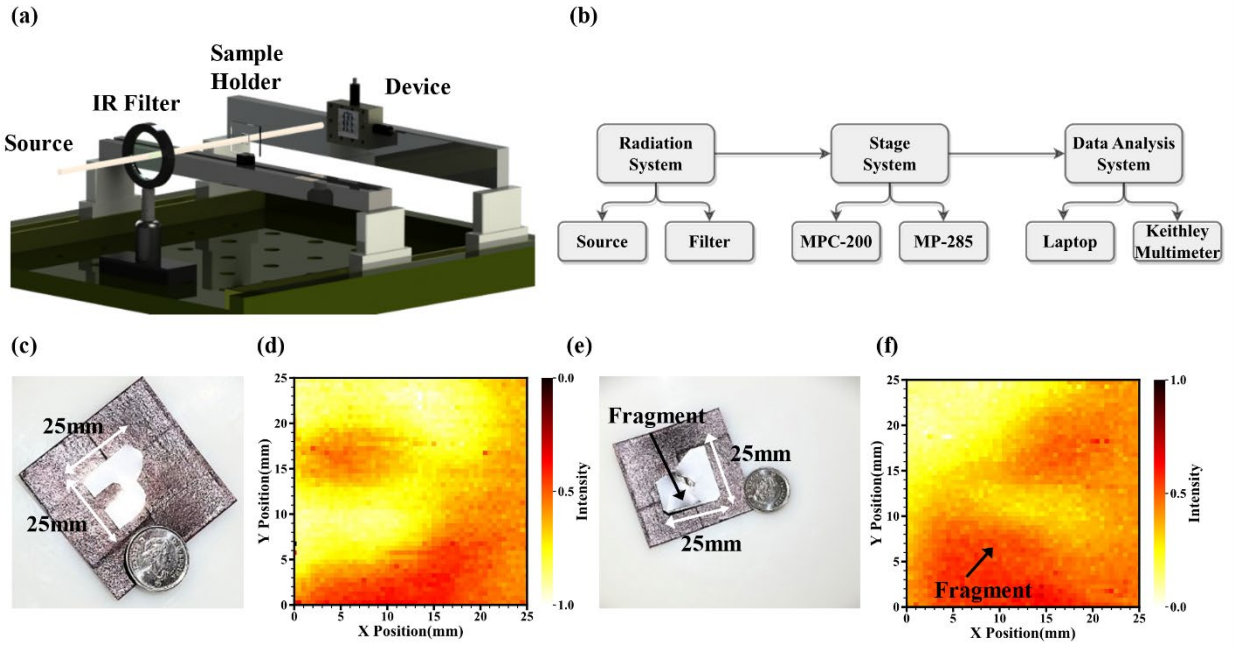

Figure 5-10. Integrated Mo_2C/PEDOT: PSS detector of the NDT imaging system. **(a)** Concept of the NDT imaging platform. **(b)** Schematic of the NDT imaging platform with radiation, stage, and data analysis systems. **(c-f)** Curvatures and deep fragment detection of two sample images and their NDT images. One is an 'h' shape, and the other is a heart shape with an additional fragment.

5.4 Conclusion

In this chapter, we proposed and fabricated a self-powered, broadband infrared region PTE detector based on Mo_2C/PEDOT: PSS with a flexible PET substrate. By adjusting the Mo_2C concentration and utilizing the spray coating method, we optimized the performance of the Mo_2C/PEDOT: PSS detector under 973 K global blackbody radiation with a 4.2 V W^{-1} response, 1.2×10^8 cm $Hz^{1/2}$ W^{-1} detectivity and low 1.06×10^{-9} cm $Hz^{1/2}$ W^{-1} NEP. Such achievements are owing to PTE's superior high-efficiency energy conversion, significant Seebeck coefficient at

-37.2 μV K^{-1}, enhanced electrical conductivity, and suppressed heat dissipation, as discussed in the paper. Besides outstanding PTE conversion, as flexible devices, Mo_2C/PEDOT: PSS detectors demonstrate their long-term and durable stability while minimizing drop at room-temperature surroundings. By combining the excellence in mechanical and self-power PTE principles, we propose two potential systems: motion tracking and NDT image systems. Both demo applications provide new sights in various applications for flexible detectors. We foresee Mo_2C/PEDOT: PSS detector, combined with self-established systems, will play a prominent role in industrial work, medical tracking, public security and health, space exploration, and kinematics learning.

Chapter 6 Summary and future work

6.1 Summary of contributions

PTE detectors demonstrate superior broadband detection, room-temperature operation, and self-powered capabilities. However, several issues remain to be solved. The fabrication process of CNTs or single-layer 2D materials is costly and complicated. Short-term stability and the fragile transfer process prevent such promising detectors from being applied in various applications. In this thesis, addressing these challenges requires ongoing research and development in material synthesis, fabrication techniques, and process optimization. Some potential strategies to overcome these issues include polymer matrixes for synthesis, an alternative for new 2D materials, and an improved material fabrication process. Below is a specific summary of my contribution to PTE detectors.

My first contribution is accomplishing a high-performance, bias-free PTE detector using a doped PANI/graphene composite. The overall performance of the detector is improved due to solid π-π junctions, assisting the electrons moving along the temperature gradient. Polymer-involved PTE matrix provides enough space for graphene dispersion and avoids flake aggregation. Besides, such doped PANI/graphene can maintain long-term stability and obtain substantial flexibility, suggesting its anticipation as a wearable health monitor. As the firstly attempt to introduce PANI in the PTE detector to improve its stability and conductivity in overall PTE performance, the involvement of fabrication-free and cost-free PANI/graphene materials makes it potential for massive productions in array detectors without complex synthesis procedures. This part of the work is provided in Chapter 3.

My second contribution is to attain self-power, low-cost, and flexible vertical PTE array detectors based on graphene and PEI composite within a unique spray-coating method. The polymer-matrix-involved nanocomposite optimizes mechanical stability, biocompatibility, and structure flexibility, enhances photoreactivity and responsivity, and improves the combination of various substrates by involving spray coating methods and combing manipulation of PEI concentration. A high photovoltage detectivity of 6.05×10^7 cm $Hz^{1/2}$ W^{-1} and 2.7 V W^{-1} response is achieved at a 2.98 μm peak wavelength on PET substrate, focusing on realistic situations with low incident power. Furthermore, stability and flexibility investigation proves 90-day long-term sustainability and prominent applications in health electronics and wearable biological applications. The spray-coating method has dealt with the procedure of non-uniform and rounded shape structures. Besides, the spray-coating method has reduced the surface tension with the substrates and improved the performance on both hydrophobic and hydrophilic substrates. This new dispersion method and PEI polymer will benefit realistic industrial applications and security monitors with extreme surroundings. This part of the work is shown in Chapter 4.

Finally, my third contribution is to propose and fabricate a self-powered, broadband infrared region PTE detector based on Mo_2C/PEDOT: PSS with a flexible PET substrate. By adjusting the Mo_2C concentration and utilizing the spray coating method, we optimized the performance of the Mo_2C/PEDOT: PSS detector under 973 K global blackbody radiation with a 4.2 V W^{-1} response, 1.2×10^8 cm $Hz^{1/2}$ W^{-1} detectivity and low 1.06×10^{-9} cm $Hz^{1/2}$ W^{-1} NEP. Besides, we integrate such devices into two separate systems and make their demos. The motion tracking and NDT systems show high spatial resolution and sensitive real-time tracking, bridging scientific research and future applications. By involving the PEDOT: PSS, the highly transparent chemical will assist

the transparent, flexible detector to improve its applications in human health monitor, eye tracking systems, and further biomedical productions. This part of the work is shown in Chapter 5.

7.2 Future work

Currently, the study of PTE still faces some challenges. These challenges are often associated with the complexity of the underlying physical processes, the intricacies involved in understanding and optimizing the performance of PTE devices, and the integration of formatted chip systems. Herein, I would like to propose some potential strategies to improve the overall performance of PTE detection and practical applications.

7.2.1 Material optimization

While 2D materials hold great promise for a wide range of applications, they also face challenges and issues, such as bandgap issues, environmental stability, scalability, and cost production researchers are actively working to overcome. 2D materials have many potentials for IR range absorption as the limitations of the disorder. Combining new polymers and modifying surface function groups can enhance the IR range. On the one hand, the absorption of photons in such a PTE detector can be improved by cooperating with a synthesized composite in multiple layers/solo mixture. On the other hand, seeking more extensive ZT value materials, including high carrier mobility, significant Seebeck coefficient, and low thermal conductivity of thermoelectrical materials, is another essential guide for sufficient energy conversion.

7.2.2 Structural optimization

Traditional PTE detectors are dual metal as electrodes with the same metal. Therefore, the excite of the free carriers usually select the cross-section of the electrode side with the material layer, which only limits effective area. To extend the detectivity of the surface area, one should consider

using the two different electrodes with a high Seebeck coefficient. Therefore, the generated photovoltage will increase. Another improvement method is to use a vertical structure with a limited top electrode layer, as metal electrodes will reflect most of the injected electromagnetic waves. Besides, switching the metal layer to a high conductive and IR absorption layer is more suitable to improve overall performance, such as CNT/MXene electrodes.

Miniature, patterned with signal amplifier circuits, should also be considered. How to combine with current clean room standard operation without any pollution concerns and nanomaterial explosion issues is still questionable and unclear. Also, the affinity with PCB boards to integrate with electronic devices is still challenging for realistic applications.

7.2.3 Fabrication optimization

As PTE detectors, the response time is related to the mean free path of the electrode. Therefore, restricting the height of the photoactive layer will force the electrode carriers to flow along the temperature gradient. Even if the spray coating method can shrink the layer's height, precise control of the uniform layer may require a more dedicated methodology. Also, to reduce any fabrication costs and mass production is desired. For the active layer, the synthesis of stable in-room ambient surroundings and avoidance of oxidation

7.2.4 Application consideration

While motion tracking and NDT systems have been approved, they’re almost not in package size or easy to auto-generate results. To fully consider software integration for all signal processes, artificial intelligence to assist in dealing with pixel read-out data and optimize the image quality and portable smartphone apps are eagerly desired to fulfill such commercial demos. Furthermore, biological compacity and health concerns should be fully demonstrated with certifications.

References

[1] C. Liu *et al.*, "Silicon/2D-material photodetectors: from near-infrared to mid-infrared," *Light Sci. Appl.*, vol. 10, no. 1, p. 123, 2021, doi: 10.1038/s41377-021-00551-4.

[2] F. Wang *et al.*, "2D Metal Chalcogenides for IR Photodetection," *Small*, vol. 15, no. 30, p. 1901347, Jul. 2019, doi: https://doi.org/10.1002/smll.201901347.

[3] X. Guan *et al.*, "Recent Progress in Short- to Long-Wave Infrared Photodetection Using 2D Materials and Heterostructures," *Adv. Opt. Mater.*, vol. 9, no. 4, p. 2001708, Feb. 2021, doi: https://doi.org/10.1002/adom.202001708.

[4] E. Song *et al.*, "Heavy Mn2+ doped MgAl2O4 phosphor for high-efficient near-infrared light-emitting diode and the night-vision application," *Adv. Opt. Mater.*, vol. 7, no. 24, p. 1901105, 2019.

[5] M. Vollmer, "Infrared thermal imaging," in *Computer Vision: A Reference Guide*, Springer, 2021, pp. 666–670.

[6] M. Gerhards, M. Schlerf, K. Mallick, and T. Udelhoven, "Challenges and future perspectives of multi-/Hyperspectral thermal infrared remote sensing for crop water-stress detection: A review," *Remote Sens.*, vol. 11, no. 10, p. 1240, 2019.

[7] K. B. Beć, J. Grabska, and C. W. Huck, "Biomolecular and bioanalytical applications of infrared spectroscopy–A review," *Anal. Chim. Acta*, vol. 1133, pp. 150–177, 2020.

[8] M. Shimoni, R. Haelterman, and C. Perneel, "Hypersectral imaging for military and security applications: Combining myriad processing and sensing techniques," *IEEE Geosci. Remote Sens. Mag.*, vol. 7, no. 2, pp. 101–117, 2019.

[9] J. Xu *et al.*, "Recent advances in near-infrared emitting lanthanide-doped nanoconstructs: Mechanism, design and application for bioimaging," *Coord. Chem. Rev.*, vol. 381, pp. 104–134, 2019.

[10] M. Amiri and N. Alizadeh, "Mid-infrared photoconductivity of polypyrrole doped with cadmium sulfide quantum dots," *J. Phys. Chem. Solids*, vol. 141, p. 109383, 2020.

[11] Q. Guo *et al.*, "Enhanced heat dissipation in gallium nitride-based light-emitting diodes by piezo-phototronic effect," *Nano Lett.*, vol. 21, no. 9, pp. 4062–4070, 2021.

[12] M. Shimatani, S. Fukushima, S. Okuda, and S. Ogawa, "High-performance graphene/InSb heterojunction photodetectors for high-resolution mid-infrared image sensors," *Appl. Phys. Lett.*, vol. 117, no. 17, p. 173102, 2020.

[13] X. Lu, L. Sun, P. Jiang, and X. Bao, "Progress of photodetectors based on the photothermoelectric effect," *Adv. Mater.*, vol. 31, no. 50, p. 1902044, 2019.

[14] Z. Xie, J. Wang, and J. T. W. Yeow, "Flexible Multi-Element Photothermoelectric Detectors Based on Spray-Coated Graphene/Polyethylenimine Composites for Nondestructive Testing," *ACS Appl. Mater. Interfaces*, vol. 15, no. 4, pp. 5921–5930, 2023, doi: 10.1021/acsami.2c20487.

[15] J. Wang, Z. Xie, G. Lu, J. A. Liu, and J. T. W. Yeow, "An infrared photothermoelectric detector enabled by MXene and PEDOT: PSS composite for noncontact fingertip tracking," *Microsystems Nanoeng.*, vol. 9, no. 1, p. 21, 2023.

[16] Z. Xie, J. Wang, and J. T. W. Yeow, "Doped Polyaniline/Graphene Composites for Photothermoelectric Detectors," *ACS Appl. Nano Mater.*, vol. 5, no. 6, pp. 7967–7973,

2022, doi: 10.1021/acsanm.2c01039.

[17] D. K. Efetov *et al.*, “Fast thermal relaxation in cavity-coupled graphene bolometers with a Johnson noise read-out,” *Nat. Nanotechnol.*, vol. 13, no. 9, pp. 797–801, 2018, doi: 10.1038/s41565-018-0169-0.

[18] J. Xu *et al.*, “2D matrix engineering for homogeneous quantum dot coupling in photovoltaic solids,” *Nat. Nanotechnol.*, vol. 13, no. 6, pp. 456–462, 2018, doi: 10.1038/s41565-018-0117-z.

[19] L.-B. Luo *et al.*, “Near-Infrared Light Photovoltaic Detector Based on GaAs Nanocone Array/Monolayer Graphene Schottky Junction,” *Adv. Funct. Mater.*, vol. 24, no. 19, pp. 2794–2800, May 2014, doi: https://doi.org/10.1002/adfm.201303368.

[20] U. Sassi *et al.*, “Graphene-based mid-infrared room-temperature pyroelectric bolometers with ultrahigh temperature coefficient of resistance,” *Nat. Commun.*, vol. 8, no. 1, p. 14311, 2017, doi: 10.1038/ncomms14311.

[21] D. Suzuki, K. Li, K. Ishibashi, and Y. Kawano, “A Terahertz Video Camera Patch Sheet with an Adjustable Design based on Self-Aligned, 2D, Suspended Sensor Array Patterning,” *Adv. Funct. Mater.*, vol. 31, no. 14, pp. 1–8, 2021, doi: 10.1002/adfm.202008931.

[22] K. Kawase, Y. Ogawa, Y. Watanabe, and H. Inoue, “Non-destructive terahertz imaging of illicit drugs using spectral fingerprints,” *Opt. Express*, vol. 11, no. 20, pp. 2549–2554, 2003, doi: 10.1364/OE.11.002549.

[23] X. Yang *et al.*, “CNN with spatio-temporal information for fast suspicious object

detection and recognition in THz security images," *Signal Processing*, vol. 160, pp. 202–214, 2019, doi: https://doi.org/10.1016/j.sigpro.2019.02.029.

[24] D. Suzuki, S. Oda, and Y. Kawano, "A flexible and wearable terahertz scanner," *Nat. Photonics*, vol. 10, no. 12, pp. 809–813, 2016, doi: 10.1038/nphoton.2016.209.

[25] S. U. Hwu, K. B. deSilva, and C. T. Jih, "Terahertz (THz) wireless systems for space applications," in *2013 IEEE Sensors Applications Symposium Proceedings*, 2013, pp. 171–175, doi: 10.1109/SAS.2013.6493580.

[26] Q. Qiu and Z. Huang, "Photodetectors of 2D Materials from Ultraviolet to Terahertz Waves," *Adv. Mater.*, vol. 33, no. 15, p. 2008126, Apr. 2021, doi: https://doi.org/10.1002/adma.202008126.

[27] X. He *et al.*, "Carbon Nanotube Terahertz Detector," *Nano Lett.*, vol. 14, no. 7, pp. 3953–3958, Jul. 2014, doi: 10.1021/nl5012678.

[28] L. Ju *et al.*, "Graphene plasmonics for tunable terahertz metamaterials," *Nat. Nanotechnol.*, vol. 6, no. 10, pp. 630–634, 2011, doi: 10.1038/nnano.2011.146.

[29] S. Castilla *et al.*, "Fast and Sensitive Terahertz Detection Using an Antenna-Integrated Graphene pn Junction," *Nano Lett.*, vol. 19, no. 5, pp. 2765–2773, May 2019, doi: 10.1021/acs.nanolett.8b04171.

[30] L. Viti *et al.*, "Black Phosphorus Terahertz Photodetectors," *Adv. Mater.*, vol. 27, no. 37, pp. 5567–5572, Oct. 2015, doi: https://doi.org/10.1002/adma.201502052.

[31] C. J. Docherty *et al.*, "Ultrafast Transient Terahertz Conductivity of Monolayer MoS2 and WSe2 Grown by Chemical Vapor Deposition," *ACS Nano*, vol. 8, no. 11, pp. 11147–

11153, Nov. 2014, doi: 10.1021/nn5034746.

[32] Y. I. Jhon, M. Seo, and Y. M. Jhon, “First-principles study of a MXene terahertz detector,” *Nanoscale*, vol. 10, no. 1, pp. 69–75, 2018, doi: 10.1039/c7nr05351g.

[33] X. Lu, L. Sun, P. Jiang, and X. Bao, “Progress of Photodetectors Based on the Photothermoelectric Effect,” *Adv. Mater.*, vol. 31, no. 50, p. 1902044, Dec. 2019, doi: https://doi.org/10.1002/adma.201902044.

[34] M. Zhang and J. T. W. W. Yeow, “A flexible, scalable, and self-powered mid-infrared detector based on transparent PEDOT: PSS/graphene composite,” *Carbon N. Y.*, vol. 156, pp. 339–345, 2020, doi: 10.1016/j.carbon.2019.09.062.

[35] N.-N. Zhao, P.-J. Guo, X.-Q. Lu, Q. Han, K. Liu, and Z.-Y. Lu, “Topological properties of Mo 2 C and W 2 C superconductors,” *Phys. Rev. B*, vol. 101, no. 19, p. 195144, 2020.

[36] J. Wang, Z. Xie, J. A. Liu, G. Lu, R. Zhou, and J. T. W. Yeow, “Capillary-Assisted Self-Assembly of Carbon Nanotubes for the Self-Powered Photothermoelectric Detector,” *Adv. Mater. Technol.*, p. 2300309, 2023.

[37] S. J. Rowley-Neale, C. W. Foster, G. C. Smith, D. A. C. Brownson, and C. E. Banks, “Mass-producible 2D-MoSe 2 bulk modified screen-printed electrodes provide significant electrocatalytic performances towards the hydrogen evolution reaction,” *Sustain. Energy Fuels*, vol. 1, no. 1, pp. 74–83, 2017.

[38] M. Shibata, Y. Sakai, and D. Yokoyama, “Advantages and disadvantages of vacuum-deposited and spin-coated amorphous organic semiconductor films for organic light-emitting diodes,” *J. Mater. Chem. C*, vol. 3, no. 42, pp. 11178–11191, 2015.

[39] K. Choonee, R. R. A. Syms, M. M. Ahmad, and H. Zou, "Post processing of microstructures by PDMS spray deposition," *Sensors Actuators A Phys.*, vol. 155, no. 2, pp. 253–262, 2009, doi: https://doi.org/10.1016/j.sna.2009.08.029.

[40] C. L. Cassano, T. Z. Georgiev, and Z. H. Fan, "Using airbrushes to pattern reagents for microarrays and paper-fluidic devices," *Microsystems Nanoeng.*, vol. 3, no. 1, p. 17055, 2017, doi: 10.1038/micronano.2017.55.

[41] S. Srinivasan, S. S. Chhatre, J. M. Mabry, R. E. Cohen, and G. H. McKinley, "Solution spraying of poly(methyl methacrylate) blends to fabricate microtextured, superoleophobic surfaces," *Polymer (Guildf).*, vol. 52, no. 14, pp. 3209–3218, 2011, doi: https://doi.org/10.1016/j.polymer.2011.05.008.

[42] Y. Zheng, R. Wu, W. Shi, Z. Guan, and J. Yu, "Effect of in situ annealing on the performance of spray coated polymer solar cells," *Sol. Energy Mater. Sol. Cells*, vol. 111, pp. 200–205, 2013, doi: https://doi.org/10.1016/j.solmat.2013.01.011.

[43] K. S. Sadanandan *et al.*, "Graphene coated fabrics by ultrasonic spray coating for wearable electronics and smart textiles," *JPhys Mater.*, vol. 4, no. 1, 2021, doi: 10.1088/2515-7639/abc632.

[44] K. Choudhary *et al.*, "Comparison of the Mechanical Properties of a Conjugated Polymer Deposited Using Spin Coating, Interfacial Spreading, Solution Shearing, and Spray Coating," *ACS Appl. Mater. Interfaces*, vol. 13, no. 43, pp. 51436–51446, Nov. 2021, doi: 10.1021/acsami.1c13043.

[45] H.-B. Liu, H. Zhong, N. Karpowicz, Y. Chen, and X.-C. Zhang, "Terahertz Spectroscopy and Imaging for Defense and Security Applications," *Proc. IEEE*, vol. 95, no. 8, pp.

1514–1527, 2007, doi: 10.1109/JPROC.2007.898903.

[46] P. U. Jepsen, D. G. Cooke, and M. Koch, “Terahertz spectroscopy and imaging – Modern techniques and applications,” *Laser Photon. Rev.*, vol. 5, no. 1, pp. 124–166, Jan. 2011, doi: https://doi.org/10.1002/lpor.201000011.

[47] D. M. Mittleman, M. Gupta, R. Neelamani, R. G. Baraniuk, J. V Rudd, and M. Koch, “Recent advances in terahertz imaging,” *Appl. Phys. B*, vol. 68, no. 6, pp. 1085–1094, 1999, doi: 10.1007/s003400050750.

[48] G. Kastberger and R. Stachl, “Infrared imaging technology and biological applications,” *Behav. Res. Methods, Instruments, Comput.*, vol. 35, no. 3, pp. 429–439, 2003, doi: 10.3758/BF03195520.

[49] Q. Weng, “Thermal infrared remote sensing for urban climate and environmental studies: Methods, applications, and trends,” *ISPRS J. Photogramm. Remote Sens.*, vol. 64, no. 4, pp. 335–344, 2009, doi: https://doi.org/10.1016/j.isprsjprs.2009.03.007.

[50] F. R. Gfeller and U. Bapst, “Wireless in-house data communication via diffuse infrared radiation,” *Proc. IEEE*, vol. 67, no. 11, pp. 1474–1486, 1979, doi: 10.1109/PROC.1979.11508.

[51] R. Zhang *et al.*, “Noninvasive Electromagnetic Wave Sensing of Glucose,” *Sensors*, vol. 19, no. 5. 2019, doi: 10.3390/s19051151.

[52] N. Kaur, M. Singh, D. Pathak, T. Wagner, and J. M. Nunzi, “Organic materials for photovoltaic applications: Review and mechanism,” *Synth. Met.*, vol. 190, pp. 20–26, 2014, doi: https://doi.org/10.1016/j.synthmet.2014.01.022.

[53] S. Kim, V. Q. Hoang, and C. W. Bark, “Silicon-Based Technologies for Flexible Photovoltaic (PV) Devices: From Basic Mechanism to Manufacturing Technologies,” *Nanomaterials*, vol. 11, no. 11. 2021, doi: 10.3390/nano11112944.

[54] R. Yu, Q. Lin, S.-F. Leung, and Z. Fan, “Nanomaterials and nanostructures for efficient light absorption and photovoltaics,” *Nano Energy*, vol. 1, no. 1, pp. 57–72, 2012, doi: https://doi.org/10.1016/j.nanoen.2011.10.002.

[55] G. Ghione, *Semiconductor devices for high-speed optoelectronics*. Cambridge ; New York : Cambridge University Press, 2009.

[56] P. V. K. Yadav, I. Yadav, B. Ajitha, A. Rajasekar, S. Gupta, and Y. Ashok Kumar Reddy, “Advancements of uncooled infrared microbolometer materials: A review,” *Sensors Actuators A Phys.*, vol. 342, p. 113611, 2022, doi: https://doi.org/10.1016/j.sna.2022.113611.

[57] P. L. Richards, “Bolometers for infrared and millimeter waves,” *J. Appl. Phys.*, vol. 76, no. 1, pp. 1–24, Jul. 1994, doi: 10.1063/1.357128.

[58] M. Henini and M. Razeghi, *Handbook of infrared detection technologies*. Elsevier, 2002.

[59] M. Aleks *et al.*, “An Overview of Microelectronic Infrared Pyroelectric Detector ,” *Engineered Science* , vol. 16. pp. 82–89, 2021, doi: 10.30919/es8d535.

[60] A. Hossain and M. H. Rashid, “Pyroelectric detectors and their applications,” *IEEE Trans. Ind. Appl.*, vol. 27, no. 5, pp. 824–829, 1991, doi: 10.1109/28.90335.

[61] D. Zhang, H. Wu, C. R. Bowen, and Y. Yang, “Recent Advances in Pyroelectric Materials and Applications,” *Small*, vol. 17, no. 51, p. 2103960, Dec. 2021, doi:

https://doi.org/10.1002/smll.202103960.

[62] R. A. Kishore and S. Priya, “A Review on Low-Grade Thermal Energy Harvesting: Materials, Methods and Devices,” *Materials (Basel).*, vol. 11, no. 8, 2018, doi: 10.3390/ma11081433.

[63] S. B. Lang, “Pyroelectricity: From Ancient Curiosity to Modern Imaging Tool,” *Phys. Today*, vol. 58, no. 8, pp. 31–36, Aug. 2005, doi: 10.1063/1.2062916.

[64] M. Jablan, H. Buljan, and M. Soljačić, “Plasmonics in graphene at infrared frequencies,” *Phys. Rev. B*, vol. 80, no. 24, p. 245435, Dec. 2009, doi: 10.1103/PhysRevB.80.245435.

[65] B. T. Diroll, S. Jeong, and X. Ye, “Ultrafast Dynamics of Colloidal Copper Nanorods: Intraband versus Interband Excitation,” *Small Sci.*, vol. 2, no. 3, p. 2100103, Mar. 2022, doi: https://doi.org/10.1002/smsc.202100103.

[66] S. Shoji, H. Suzuki, R. P. Zaccaria, Z. Sekkat, and S. Kawata, “Optical polarizer made of uniaxially aligned short single-wall carbon nanotubes embedded in a polymer film,” *Phys. Rev. B*, vol. 77, no. 15, p. 153407, Apr. 2008, doi: 10.1103/PhysRevB.77.153407.

[67] R. F. Rajter, R. Podgornik, V. A. Parsegian, R. H. French, and W. Y. Ching, “van der Waals--London dispersion interactions for optically anisotropic cylinders: Metallic and semiconducting single-wall carbon nanotubes,” *Phys. Rev. B*, vol. 76, no. 4, p. 45417, Jul. 2007, doi: 10.1103/PhysRevB.76.045417.

[68] H.-S. Kim, Z. M. Gibbs, Y. Tang, H. Wang, and G. J. Snyder, “Characterization of Lorenz number with Seebeck coefficient measurement,” *APL Mater.*, vol. 3, no. 4, p. 41506, Feb. 2015, doi: 10.1063/1.4908244.

[69] X. Wang, V. Askarpour, J. Maassen, and M. Lundstrom, “On the calculation of Lorenz numbers for complex thermoelectric materials,” *J. Appl. Phys.*, vol. 123, no. 5, p. 55104, Feb. 2018, doi: 10.1063/1.5009939.

[70] H. Xu, M. Wang, Z.-G. Yu, K. Wang, and B. Hu, “Magnetic field effects on excited states, charge transport, and electrical polarization in organic semiconductors in spin and orbital regimes,” *Adv. Phys.*, vol. 68, no. 2, pp. 49–121, Apr. 2019, doi: 10.1080/00018732.2019.1590295.

[71] J. Yang, G. Yang, G. Zhang, and Y. X. Wang, “Low effective mass leading to an improved ZT value by 32% for n-type BiCuSeO: a first-principles study,” *J. Mater. Chem. A*, vol. 2, no. 34, pp. 13923–13931, 2014, doi: 10.1039/C4TA02050B.

[72] M. Markov *et al.*, “Semi-metals as potential thermoelectric materials,” *Sci. Rep.*, vol. 8, no. 1, p. 9876, 2018, doi: 10.1038/s41598-018-28043-3.

[73] Z. Wang, X. Li, G. Zhang, Y. Luo, and J. Jiang, “Suppressing Electron–Phonon Coupling through Laser-Induced Phase Transition,” *ACS Appl. Mater. Interfaces*, vol. 9, no. 28, pp. 23309–23313, Jul. 2017, doi: 10.1021/acsami.7b05480.

[74] L. Yan, M. Shao, H. Wang, D. Dudis, A. Urbas, and B. Hu, “High Seebeck effects from hybrid metal/polymer/metal thin-film devices.,” *Adv. Mater.*, vol. 23, no. 35, pp. 4120–4124, Sep. 2011, doi: 10.1002/adma.201101634.

[75] R. J. Young, I. A. Kinloch, L. Gong, and K. S. Novoselov, “The mechanics of graphene nanocomposites: A review,” *Compos. Sci. Technol.*, vol. 72, no. 12, pp. 1459–1476, 2012, doi: https://doi.org/10.1016/j.compscitech.2012.05.005.

[76] W. Xu, H. M. Dong, L. L. Li, J. Q. Yao, P. Vasilopoulos, and F. M. Peeters, "Optoelectronic properties of graphene in the presence of optical phonon scattering," *Phys. Rev. B*, vol. 82, no. 12, p. 125304, Sep. 2010, doi: 10.1103/PhysRevB.82.125304.

[77] D. R. Cooper *et al.*, "Experimental Review of Graphene," *ISRN Condens. Matter Phys.*, vol. 2012, p. 501686, 2012, doi: 10.5402/2012/501686.

[78] A. Omidvar, "Electronic structure tuning and band gap opening of nitrogen and boron doped holey graphene flake: The role of single/dual doping," *Mater. Chem. Phys.*, vol. 202, pp. 258–265, 2017, doi: https://doi.org/10.1016/j.matchemphys.2017.09.025.

[79] T. Low and P. Avouris, "Graphene Plasmonics for Terahertz to Mid-Infrared Applications," *ACS Nano*, vol. 8, no. 2, pp. 1086–1101, Feb. 2014, doi: 10.1021/nn406627u.

[80] M. Yankowitz *et al.*, "Tuning superconductivity in twisted bilayer graphene," *Science (80-.).*, vol. 363, no. 6431, pp. 1059–1064, 2019, doi: 10.1126/science.aav1910.

[81] G. Li *et al.*, "Observation of Van Hove singularities in twisted graphene layers," *Nat. Phys.*, vol. 6, no. 2, pp. 109–113, 2010, doi: 10.1038/nphys1463.

[82] L. Lin, H. Peng, and Z. Liu, "Synthesis challenges for graphene industry," *Nat. Mater.*, vol. 18, no. 6, pp. 520–524, 2019, doi: 10.1038/s41563-019-0341-4.

[83] P. Avouris and C. Dimitrakopoulos, "Graphene: Synthesis and applications," *Mater. Today*, vol. 15, no. 3, pp. 86–97, 2012, doi: 10.1016/S1369-7021(12)70044-5.

[84] S. Ullah *et al.*, "Graphene transfer methods: A review," *Nano Res.*, vol. 14, no. 11, pp. 3756–3772, 2021, doi: 10.1007/s12274-021-3345-8.

[85] S. Gorantla *et al.*, “A universal transfer route for graphene,” *Nanoscale*, vol. 6, no. 2, pp. 889–896, 2014, doi: 10.1039/C3NR04739C.

[86] G. J. M. Fechine *et al.*, “Direct dry transfer of chemical vapor deposition graphene to polymeric substrates,” *Carbon N. Y.*, vol. 83, pp. 224–231, 2015, doi: https://doi.org/10.1016/j.carbon.2014.11.038.

[87] Y. Wang *et al.*, “Electrochemical Delamination of CVD-Grown Graphene Film: Toward the Recyclable Use of Copper Catalyst,” *ACS Nano*, vol. 5, no. 12, pp. 9927–9933, Dec. 2011, doi: 10.1021/nn203700w.

[88] D. L. Mafra, T. Ming, and J. Kong, “Facile graphene transfer directly to target substrates with a reusable metal catalyst,” *Nanoscale*, vol. 7, no. 36, pp. 14807–14812, 2015, doi: 10.1039/C5NR03892H.

[89] R. W. (1997) Shleifer, A., & Vishny, “Scholar (59).” 1997.

[90] W. S. Williams, “Transition-metal carbides,” *Prog. Solid State Chem.*, vol. 6, pp. 57–118, 1971, doi: https://doi.org/10.1016/0079-6786(71)90028-8.

[91] B. C. Wyatt, S. K. Nemani, and B. Anasori, “2D transition metal carbides (MXenes) in metal and ceramic matrix composites,” *Nano Converg.*, vol. 8, no. 1, p. 16, 2021, doi: 10.1186/s40580-021-00266-7.

[92] K. Huang, Z. Li, J. Lin, G. Han, and P. Huang, “Two-dimensional transition metal carbides and nitrides (MXenes) for biomedical applications,” *Chem. Soc. Rev.*, vol. 47, no. 14, pp. 5109–5124, 2018, doi: 10.1039/C7CS00838D.

[93] K. Hantanasirisakul and Y. Gogotsi, “Electronic and Optical Properties of 2D Transition

Metal Carbides and Nitrides (MXenes)," *Adv. Mater.*, vol. 30, no. 52, p. 1804779, Dec. 2018, doi: https://doi.org/10.1002/adma.201804779.

[94] Y. I. Jhon *et al.*, "Metallic MXene Saturable Absorber for Femtosecond Mode-Locked Lasers," *Adv. Mater.*, vol. 29, no. 40, p. 1702496, Oct. 2017, doi: https://doi.org/10.1002/adma.201702496.

[95] J. Wang, "Nanocomposite Based Infrared Photothermoelectric Detectors by," 2023.

[96] Y. Gogotsi, "Transition metal carbides go 2D," *Nat. Mater.*, vol. 14, no. 11, pp. 1079–1080, 2015, doi: 10.1038/nmat4386.

[97] T. Qin, Z. Wang, Y. Wang, F. Besenbacher, M. Otyepka, and M. Dong, "Recent Progress in Emerging Two-Dimensional Transition Metal Carbides," *Nanomicro Lett*, vol. 13, no. 1, p. 183, 2021, doi: 10.1007/s40820-021-00710-7.

[98] C. Xu *et al.*, "Large-area high-quality 2D ultrathin Mo2C superconducting crystals," *Nat. Mater.*, vol. 14, no. 11, pp. 1135–1141, 2015, doi: 10.1038/nmat4374.

[99] Y. Su, M. Yang, X. Wang, F. Tian, H. Jia, and L. Li, "Synthesis of Ni nanoparticles embedded porous Mo2C nanospheres for enhancing the electrochemical hydrogen storage properties of Co2B material," *J. Alloys Compd.*, vol. 954, p. 170143, 2023, doi: 10.1016/j.jallcom.2023.170143.

[100] M. I. Naher and S. H. Naqib, "Possible applications of Mo2C in the orthorhombic and hexagonal phases explored via ab-initio investigations of elastic, bonding, optoelectronic and thermophysical properties," *Results Phys.*, vol. 37, p. 105505, 2022, doi: https://doi.org/10.1016/j.rinp.2022.105505.

[101] Y. Liu *et al.*, " Coupling Mo 2 C with Nitrogen-Rich Nanocarbon Leads to Efficient Hydrogen-Evolution Electrocatalytic Sites ," *Angew. Chemie*, vol. 127, no. 37, pp. 10902–10907, 2015, doi: 10.1002/ange.201504376.

[102] T. Ouyang, Y. Q. Ye, C. Y. Wu, K. Xiao, and Z. Q. Liu, "Heterostructures Composed of N-Doped Carbon Nanotubes Encapsulating Cobalt and beta-Mo(2) C Nanoparticles as Bifunctional Electrodes for Water Splitting," *Angew Chem Int Ed Engl*, vol. 58, no. 15, pp. 4923–4928, 2019, doi: 10.1002/anie.201814262.

[103] B. Zhou, J. Song, B. Wang, Y. Feng, C. Liu, and C. Shen, "Robust double-layered ANF/MXene-PEDOT:PSS Janus films with excellent multi-source driven heating and electromagnetic interference shielding properties," *Nano Res.*, vol. 15, no. 10, pp. 9520–9530, 2022, doi: 10.1007/s12274-022-4756-x.

[104] J. Jeon *et al.*, "Transition-Metal-Carbide (Mo2C) Multiperiod Gratings for Realization of High-Sensitivity and Broad-Spectrum Photodetection," *Adv. Funct. Mater.*, vol. 29, no. 48, p. 1905384, 2019, doi: https://doi.org/10.1002/adfm.201905384.

[105] M. Khazaei, M. Arai, T. Sasaki, M. Estili, and Y. Sakka, "Two-dimensional molybdenum carbides: Potential thermoelectric materials of the MXene family," *Phys. Chem. Chem. Phys.*, vol. 16, no. 17, pp. 7841–7849, 2014, doi: 10.1039/c4cp00467a.

[106] X.-H. Zha *et al.*, "Intrinsic Structural, Electrical, Thermal, and Mechanical Properties of the Promising Conductor Mo2C MXene," *J. Phys. Chem. C*, vol. 120, no. 28, pp. 15082–15088, Jul. 2016, doi: 10.1021/acs.jpcc.6b04192.

[107] J. Jeon *et al.*, "Transition-Metal-Carbide (Mo2C) Multiperiod Gratings for Realization of High-Sensitivity and Broad-Spectrum Photodetection," *Adv. Funct. Mater.*, vol. 29, no.

48, pp. 1–7, 2019, doi: 10.1002/adfm.201905384.

[108] R. A. Mir, S. Upadhyay, and O. P. Pandey, “A review on recent advances and progress in Mo2C@C: A suitable and stable electrocatalyst for HER,” *Int. J. Hydrogen Energy*, vol. 48, no. 35, pp. 13044–13067, 2023, doi: https://doi.org/10.1016/j.ijhydene.2022.12.179.

[109] K. S. Zelenska, S. E. Zelensky, L. V Poperenko, K. Kanev, V. Mizeikis, and V. A. Gnatyuk, “Thermal mechanisms of laser marking in transparent polymers with light-absorbing microparticles,” *Opt. Laser Technol.*, vol. 76, pp. 96–100, 2016, doi: https://doi.org/10.1016/j.optlastec.2015.07.011.

[110] I. Riedel, J. Parisi, V. Dyakonov, L. Lutsen, D. Vanderzande, and J. C. Hummelen, “Effect of Temperature and Illumination on the Electrical Characteristics of Polymer–Fullerene Bulk-Heterojunction Solar Cells,” *Adv. Funct. Mater.*, vol. 14, no. 1, pp. 38–44, Jan. 2004, doi: https://doi.org/10.1002/adfm.200304399.

[111] G. Chen, W. Xu, and D. Zhu, “Recent advances in organic polymer thermoelectric composites,” *J. Mater. Chem. C*, vol. 5, no. 18, pp. 4350–4360, 2017, doi: 10.1039/C6TC05488A.

[112] S. Xu, X.-L. Shi, M. Dargusch, C. Di, J. Zou, and Z.-G. Chen, “Conducting polymer-based flexible thermoelectric materials and devices: From mechanisms to applications,” *Prog. Mater. Sci.*, vol. 121, p. 100840, 2021, doi: https://doi.org/10.1016/j.pmatsci.2021.100840.

[113] M. He, F. Qiu, and Z. Lin, “Towards high-performance polymer-based thermoelectric materials,” *Energy Environ. Sci.*, vol. 6, no. 5, pp. 1352–1361, 2013, doi: 10.1039/C3EE24193A.

[114] L. Wang *et al.*, “Polymer composites-based thermoelectric materials and devices,” *Compos. Part B Eng.*, vol. 122, pp. 145–155, 2017, doi: https://doi.org/10.1016/j.compositesb.2017.04.019.

[115] E. N. Zare, P. Makvandi, B. Ashtari, F. Rossi, A. Motahari, and G. Perale, “Progress in Conductive Polyaniline-Based Nanocomposites for Biomedical Applications: A Review,” *J. Med. Chem.*, vol. 63, no. 1, pp. 1–22, Jan. 2020, doi: 10.1021/acs.jmedchem.9b00803.

[116] L. Wang, Q. Yao, H. Bi, F. Huang, Q. Wang, and L. Chen, “PANI/graphene nanocomposite films with high thermoelectric properties by enhanced molecular ordering,” *J. Mater. Chem. A*, vol. 3, no. 13, pp. 7086–7092, 2015, doi: 10.1039/c4ta06422d.

[117] X. Chen *et al.*, “One-step synthesis of graphene/polyaniline hybrids by in situ intercalation polymerization and their electromagnetic properties,” *Nanoscale*, vol. 6, no. 14, pp. 8140–8148, 2014, doi: 10.1039/c4nr01738b.

[118] J. Stejskal, P. Kratochvíl, and N. Radhakrishnan, “Polyaniline dispersions 2. UV—Vis absorption spectra,” *Synth. Met.*, vol. 61, no. 3, pp. 225–231, 1993, doi: https://doi.org/10.1016/0379-6779(93)91266-5.

[119] O. T. Ikkala, L. Pietilä, L. Ahjopalo, H. Österholm, and P. J. Passiniemi, “On the molecular recognition and associations between electrically conducting polyaniline and solvents,” *J. Chem. Phys.*, vol. 103, no. 22, pp. 9855–9863, Dec. 1995, doi: 10.1063/1.469952.

[120] Q. Yao *et al.*, “The synergic regulation of conductivity and Seebeck coefficient in pure polyaniline by chemically changing the ordered degree of molecular chains,” *J. Mater.*

Chem. A, vol. 2, no. 8, pp. 2634–2640, 2014, doi: 10.1039/C3TA14008C.

[121] Z. Morávková and P. Bober, "Writing in a polyaniline film with laser beam and stability of the record: A Raman spectroscopy study," *Int. J. Polym. Sci.*, vol. 2018, 2018, doi: 10.1155/2018/1797216.

[122] N. Chen *et al.*, "Sandwich-Like Holey Graphene/PANI/Graphene Nanohybrid for Ultrahigh-Rate Supercapacitor," *ACS Appl. Energy Mater.*, vol. 1, no. 10, pp. 5189–5197, 2018, doi: 10.1021/acsaem.8b00725.

[123] M. Zhang, D. Ban, C. Xu, and J. T. W. Yeow, "Large-Area and Broadband Thermoelectric Infrared Detection in a Carbon Nanotube Black-Body Absorber," *ACS Nano*, vol. 13, no. 11, pp. 13285–13292, 2019, doi: 10.1021/acsnano.9b06332.

[124] L. Zhang *et al.*, "Ultrasensitive and Self-Powered Terahertz Detection Driven by Nodal-Line Dirac Fermions and Van der Waals Architecture," *Adv. Sci.*, vol. 8, no. 23, p. 2102088, Dec. 2021, doi: https://doi.org/10.1002/advs.202102088.

[125] D. Wang *et al.*, "Enhancing the graphene photocurrent using surface plasmons and a p-n junction," *Light Sci. Appl.*, vol. 9, no. 1, p. 126, 2020, doi: 10.1038/s41377-020-00344-1.

[126] W. Guo *et al.*, "Sensitive Terahertz Detection and Imaging Driven by the Photothermoelectric Effect in Ultrashort-Channel Black Phosphorus Devices," *Adv. Sci.*, vol. 7, no. 5, p. 1902699, 2020.

[127] A. Zubair *et al.*, "Carbon nanotube woven textile photodetector," *Phys. Rev. Mater.*, vol. 2, no. 1, p. 15201, Jan. 2018, doi: 10.1103/PhysRevMaterials.2.015201.

[128] H. Zhou *et al.*, "A flexible in-plane p–n heterojunction nano-generator with phonon-

enhanced photothermoelectric effect to harvest solar energy," *J. Mater. Chem. A*, vol. 9, no. 26, pp. 14958–14968, 2021, doi: 10.1039/D1TA02946K.

[129] X. Lu, P. Jiang, and X. Bao, "Phonon-enhanced photothermoelectric effect in SrTiO 3 ultra-broadband photodetector," *Nat. Commun.*, vol. 10, no. 1, 2019, doi: 10.1038/s41467-018-07860-0.

[130] Y. Wang *et al.*, "Ultrabroadband, Sensitive, and Fast Photodetection with Needle-Like EuBiSe3 Single Crystal," *ACS Photonics*, vol. 6, no. 4, pp. 895–903, Apr. 2019, doi: 10.1021/acsphotonics.8b01527.

[131] J. Wen *et al.*, "Ultra-broadband self-powered reduced graphene oxide photodetectors with annealing temperature-dependent responsivity," *Carbon N. Y.*, vol. 153, pp. 274–284, 2019, doi: https://doi.org/10.1016/j.carbon.2019.07.033.

[132] M. Zhang and J. T. W. W. Yeow, "Flexible Polymer-Carbon Nanotube Composite with High-Response Stability for Wearable Thermal Imaging," *ACS Appl. Mater. Interfaces*, vol. 10, no. 31, pp. 26604–26609, 2018, doi: 10.1021/acsami.8b06482.

[133] M. Zhu *et al.*, "An enhanced solar-blind ultraviolet photodetector based on polyvinyl alcohol/carbon nanodots film," *Appl. Phys. A*, vol. 127, no. 9, p. 664, 2021, doi: 10.1007/s00339-021-04793-2.

[134] J. Yang *et al.*, "Cavity-Enhanced Near-Infrared Organic Photodetectors Based on a Conjugated Polymer Containing [1,2,5]Selenadiazolo[3,4-c]Pyridine," *Chem. Mater.*, vol. 33, no. 13, pp. 5147–5155, Jul. 2021, doi: 10.1021/acs.chemmater.1c01196.

[135] Y.-R. Guo *et al.*, "The origin, transmission and clinical therapies on coronavirus disease

2019 (COVID-19) outbreak – an update on the status," *Mil. Med. Res.*, vol. 7, no. 1, p. 11, 2020, doi: 10.1186/s40779-020-00240-0.

[136] B. Sun, W. Hong, E. S. Thibau, H. Aziz, Z.-H. Lu, and Y. Li, "Polyethylenimine (PEI) As an Effective Dopant To Conveniently Convert Ambipolar and p-Type Polymers into Unipolar n-Type Polymers," *ACS Appl. Mater. Interfaces*, vol. 7, no. 33, pp. 18662–18671, Aug. 2015, doi: 10.1021/acsami.5b05097.

[137] P. S. Parsamehr, M. Zahed, M. A. Tofighy, T. Mohammadi, and M. Rezakazemi, "Preparation of novel cross-linked graphene oxide membrane for desalination applications using (EDC and NHS)-activated graphene oxide and PEI," *Desalination*, vol. 468, p. 114079, 2019.

[138] S. Bao, W. Yang, Y. Wang, Y. Yu, Y. Sun, and K. Li, "PEI grafted amino-functionalized graphene oxide nanosheets for ultrafast and high selectivity removal of Cr (VI) from aqueous solutions by adsorption combined with reduction: Behaviors and mechanisms," *Chem. Eng. J.*, vol. 399, p. 125762, 2020.

[139] L. M. Malard, M. A. Pimenta, G. Dresselhaus, and M. S. Dresselhaus, "Raman spectroscopy in graphene," *Phys. Rep.*, vol. 473, no. 5, pp. 51–87, 2009, doi: https://doi.org/10.1016/j.physrep.2009.02.003.

[140] F. Tarannum *et al.*, "Chemically Edge-Carboxylated Graphene Enhances the Thermal Conductivity of Polyetherimide–Graphene Nanocomposites," *ACS Appl. Mater. Interfaces*, vol. 14, no. 12, pp. 14753–14763, Mar. 2022, doi: 10.1021/acsami.1c25279.

[141] C. Liu, S. Qiu, P. Du, H. Zhao, and L. Wang, "An ionic liquid–graphene oxide hybrid nanomaterial: synthesis and anticorrosive applications," *Nanoscale*, vol. 10, no. 17, pp.

8115–8124, 2018, doi: 10.1039/C8NR01890A.

[142] B. Dehghanzad, M. K. Razavi Aghjeh, O. Rafeie, A. Tavakoli, and A. Jameie Oskooie, "Synthesis and characterization of graphene and functionalized graphene via chemical and thermal treatment methods," *RSC Adv.*, vol. 6, no. 5, pp. 3578–3585, 2016, doi: 10.1039/C5RA19954A.

[143] G. Bharath, B. S. Latha, E. H. Alsharaeh, P. Prakash, and N. Ponpandian, "Enhanced hydroxyapatite nanorods formation on graphene oxide nanocomposite as a potential candidate for protein adsorption, pH controlled release and an effective drug delivery platform for cancer therapy," *Anal. Methods*, vol. 9, no. 2, pp. 240–252, 2017, doi: 10.1039/C6AY02348G.

[144] X. Wang *et al.*, "Porous biochar modified with polyethyleneimine (PEI) for effective enrichment of U(VI) in aqueous solution," *Sci. Total Environ.*, vol. 708, p. 134575, 2020, doi: https://doi.org/10.1016/j.scitotenv.2019.134575.

[145] D. Suzuki, T. Okamoto, J. Li, Y. Ito, T. Fujita, and Y. Kawano, "Terahertz and infrared response assisted by heat localization in nanoporous graphene," *Carbon N. Y.*, vol. 173, pp. 403–409, 2021, doi: 10.1016/j.carbon.2020.10.059.

[146] X. Zhang *et al.*, "Conversion of solar power to chemical energy based on carbon nanoparticle modified photo-thermoelectric generator and electrochemical water splitting system," *Nano Energy*, vol. 48, pp. 481–488, 2018.

[147] H. Liu *et al.*, "Photothermoelectric SnTe Photodetector with Broad Spectral Response and High On/Off Ratio," *ACS Appl. Mater. Interfaces*, vol. 12, no. 44, pp. 49830–49839, Nov. 2020, doi: 10.1021/acsami.0c15639.

[148] R. Wang, Z. He, J.-L. Wang, J.-Y. Liu, J.-W. Liu, and S.-H. Yu, "Manipulating Nanowire Structures for an Enhanced Broad-Band Flexible Photothermoelectric Photodetector," *Nano Lett.*, vol. 22, no. 14, pp. 5929–5935, Jul. 2022, doi: 10.1021/acs.nanolett.2c01957.

[149] B. Lv *et al.*, "Local large temperature difference and ultra-wideband photothermoelectric response of the silver nanostructure film/carbon nanotube film heterostructure," *Nat. Commun.*, vol. 13, no. 1, pp. 1–9, 2022.

[150] T. Ghomian, O. Kizilkaya, and J.-W. Choi, "Lead sulfide colloidal quantum dot photovoltaic cell for energy harvesting from human body thermal radiation," *Appl. Energy*, vol. 230, pp. 761–768, 2018.

[151] X. Q. Cao, R. Vassen, S. Schwartz, W. Jungen, F. Tietz, and D. Stöever, "Spray-drying of ceramics for plasma-spray coating," *J. Eur. Ceram. Soc.*, vol. 20, no. 14–15, pp. 2433–2439, 2000, doi: 10.1016/S0955-2219(00)00112-6.

[152] X. Huang *et al.*, "Thermal conductivity of graphene-based polymer nanocomposites," *Mater. Sci. Eng. R Reports*, vol. 142, p. 100577, 2020.

[153] H.-Y. Zhao, M.-Y. Yu, J. Liu, X. Li, P. Min, and Z.-Z. Yu, "Efficient preconstruction of three-dimensional graphene networks for thermally conductive polymer composites," *Nano-Micro Lett.*, vol. 14, no. 1, pp. 1–40, 2022.

[154] Z. Liu and G. Chen, "Advancing flexible thermoelectric devices with polymer composites," *Adv. Mater. Technol.*, vol. 5, no. 7, p. 2000049, 2020.

[155] M. Majumder *et al.*, "Insights into the physics of spray coating of SWNT films," *Chem. Eng. Sci.*, vol. 65, no. 6, pp. 2000–2008, 2010, doi: 10.1016/j.ces.2009.11.042.

[156] S. Theimer, M. Graunitz, M. Schulze, F. Gaertner, and T. Klassen, “Optimization adhesion in cold spraying onto hard substrates: A case study for brass coatings,” *J. Therm. Spray Technol.*, vol. 28, no. 1, pp. 124–134, 2019.

[157] N. Wang *et al.*, “Tailoring the thermal and mechanical properties of graphene film by structural engineering,” *Small*, vol. 14, no. 29, p. 1801346, 2018.

[158] T. D. Le, S. Park, J. An, P. S. Lee, and Y. Kim, “Ultrafast laser pulses enable one-step graphene patterning on woods and leaves for green electronics,” *Adv. Funct. Mater.*, vol. 29, no. 33, p. 1902771, 2019.

[159] C. Li *et al.*, “Three-dimensional interconnected graphene microsphere as fillers for enhancing thermal conductivity of polymer,” *Chem. Eng. J.*, vol. 368, pp. 79–87, 2019.

[160] S. Kumar, M. Kumar, and N. Jindal, “Overview of cold spray coatings applications and comparisons: a critical review,” *World J. Eng.*, vol. 17, no. 1, pp. 27–51, 2020, doi: 10.1108/WJE-01-2019-0021.

[161] X. Wang, J. Li, Y. Chen, J. Ran, Y. Yuan, and B. Yang, “Spray-Coating Thick Films of All-Inorganic Halide Perovskites for Filterless Narrowband Photodetectors,” *ACS Appl. Mater. Interfaces*, vol. 14, no. 21, pp. 24583–24591, 2022, doi: 10.1021/acsami.2c03585.

[162] R. Xiao *et al.*, “Infrared-Radiation-Enhanced Nanofiber Membrane for Sky Radiative Cooling of the Human Body,” *ACS Appl. Mater. Interfaces*, vol. 11, no. 47, pp. 44673–44681, Nov. 2019, doi: 10.1021/acsami.9b13933.

[163] X. Dai *et al.*, “Self-Healing, Flexible, and Tailorable Triboelectric Nanogenerators for Self-Powered Sensors based on Thermal Effect of Infrared Radiation,” *Adv. Funct.*

Mater., vol. 30, no. 16, p. 1910723, Apr. 2020, doi: https://doi.org/10.1002/adfm.201910723.

[164] J. Wang, Z. Xie, J. A. Liu, and J. T. W. Yeow, "Design of room-temperature infrared photothermoelectric detectors based on CNT/PEDOT:PSS composites," *J. Mater. Chem. C*, vol. 10, no. 40, pp. 15105–15113, 2022, doi: 10.1039/D2TC03159K.

[165] X. Jin *et al.*, "Ultraflexible PEDOT:PSS/Helical Carbon Nanotubes Film for All-in-One Photothermoelectric Conversion," *ACS Appl. Mater. Interfaces*, vol. 14, no. 23, pp. 27083–27095, Jun. 2022, doi: 10.1021/acsami.2c05875.

[166] M. Chen, Y. Wang, W. Ma, Y. Huang, and Z. Zhao, "Ionic Liquid Gating Enhanced Photothermoelectric Conversion in Three-Dimensional Microporous Graphene," *ACS Appl. Mater. Interfaces*, vol. 12, no. 25, pp. 28510–28519, Jun. 2020, doi: 10.1021/acsami.0c05833.

[167] D. Zhang *et al.*, "Photo-thermoelectric effect induced electricity in stretchable graphene-polymer nanocomposites for ultrasensitive strain sensing," *Nano Res.*, vol. 12, no. 12, pp. 2982–2987, 2019, doi: 10.1007/s12274-019-2541-2.

[168] H. D. Lee *et al.*, "Organic enrichment, physical phase state, and surface tension depression of nascent core–shell sea spray aerosols during two phytoplankton blooms," *ACS Earth Sp. Chem.*, vol. 4, no. 4, pp. 650–660, 2020.

[169] H. Zhang, X. Ji, L. Liu, J. Ren, F. Tao, and C. Qiao, "Versatile, mechanochemically robust, sprayed superomniphobic coating enabling low surface tension and high viscous organic liquid bouncing," *Chem. Eng. J.*, vol. 402, p. 126160, 2020.

[170] C. Yang *et al.*, "Balance Effect: A Universal Strategy for Transition Metal Carbides to Enhance Hydrogen Evolution," *Adv. Funct. Mater.*, vol. 32, no. 5, p. 2108167, 2022, doi: https://doi.org/10.1002/adfm.202108167.

[171] T. Meng, L. Zheng, J. Qin, D. Zhao, and M. Cao, "A three-dimensional hierarchically porous Mo2C architecture: salt-template synthesis of a robust electrocatalyst and anode material towards the hydrogen evolution reaction and lithium storage," *J. Mater. Chem. A*, vol. 5, no. 38, pp. 20228–20238, 2017, doi: 10.1039/C7TA05946A.

[172] C.-Q. Li, X. Shen, R.-C. Ding, and G.-S. Wang, "Excellent microwave absorption properties based on a composite of one dimensional Mo2C@C nanorods and a PVDF matrix," *RSC Adv.*, vol. 9, no. 37, pp. 21243–21248, 2019, doi: 10.1039/C9RA03362A.

[173] D. Alemu Mengistie, P.-C. Wang, and C.-W. Chu, "Effect of molecular weight of additives on the conductivity of PEDOT:PSS and efficiency for ITO-free organic solar cells," *J. Mater. Chem. A*, vol. 1, no. 34, pp. 9907–9915, 2013, doi: 10.1039/C3TA11726J.

[174] L. Yue, S. Wang, X. Zhao, and L. Zhang, "Nano-silicon composites using poly(3,4-ethylenedioxythiophene):poly(styrenesulfonate) as elastic polymer matrix and carbon source for lithium-ion battery anode," *J. Mater. Chem.*, vol. 22, no. 3, pp. 1094–1099, 2012, doi: 10.1039/C1JM14568A.

[175] J. Wang, Z. Xie, J. A. Liu, and J. T. W. Yeow, "Design of room-temperature infrared photothermoelectric detectors based on CNT/PEDOT:PSS composites," *J. Mater. Chem. C*, pp. 15105–15113, 2022, doi: 10.1039/d2tc03159k.

[176] X. Cai *et al.*, "Sensitive room-temperature terahertz detection via the photothermoelectric

effect in graphene," *Nat. Nanotechnol.*, vol. 9, no. 10, pp. 814–819, 2014, doi: 10.1038/nnano.2014.182.

[177] D. Basko, "A photothermoelectric effect in graphene," *Science (80-.).*, vol. 334, no. 6056, pp. 610–611, 2011.

[178] K. J. Erikson *et al.*, "Figure of Merit for Carbon Nanotube Photothermoelectric Detectors," *ACS Nano*, vol. 9, no. 12, pp. 11618–11627, 2015, doi: 10.1021/acsnano.5b06160.

[179] J. Wei *et al.*, "Review of current high-ZT thermoelectric materials," *J. Mater. Sci.*, vol. 55, pp. 12642–12704, 2020.

[180] I. Vangelidis *et al.*, "Unbiased plasmonic-assisted integrated graphene photodetectors," *ACS photonics*, vol. 9, no. 6, pp. 1992–2007, 2022.

[181] Y. Liu *et al.*, "High-performance ultrabroadband photodetector based on photothermoelectric effect," *ACS Appl. Mater. Interfaces*, vol. 14, no. 25, pp. 29077–29086, 2022.

[182] F. K. Yoshimoto, "The proteins of severe acute respiratory syndrome coronavirus-2 (SARS CoV-2 or n-COV19), the cause of COVID-19," *Protein J.*, vol. 39, no. 3, pp. 198–216, 2020.

[183] R. K. Will, E. F. J. Ring, A. K. Clarke, and P. J. Maddison, "Infrared thermography: what is its place in rheumatology in the 1990s?," *Rheumatology*, vol. 31, no. 5, pp. 337–344, 1992.

[184] F. Mairinger, "The infrared examination of paintings," *Radiat. Art Archeometry Eds. DC*

Creagh, DA Bradley, Elsevier, pp. 40–55, 2000.

[185] Y.-K. Zhu, G.-Y. Tian, R.-S. Lu, and H. Zhang, "A review of optical NDT technologies," *Sensors*, vol. 11, no. 8, pp. 7773–7798, 2011.

[186] D. Balageas *et al.*, "Thermal (IR) and other NDT techniques for improved material inspection," *J. Nondestruct. Eval.*, vol. 35, pp. 1–17, 2016.

[187] S. Deane *et al.*, "Application of NDT thermographic imaging of aerospace structures," *Infrared Phys. Technol.*, vol. 97, pp. 456–466, 2019.